POLITECNICO DI TORINO

POLITECNICO DI TORINO

Master Degree course in Quantum Engineering

Master Degree Thesis

Generation and characterization of entangled states of light in a Si_3N_4 microresonator

Supervisors
Prof. Lorenzo Columbo
Dr. Alice Meda
Dr. Francesca Famà

Candidate
Lorenzo Lucia

Academic Year 2024-2025

Acknowledgements

Grazie.

Abstract

The development of compact, bright, and robust quantum light sources is a fundamental requirement for scalable quantum communication, quantum key distribution, and future quantum networks. Photonic integrated circuits based on third-order ($\chi^{(3)}$) microresonators provide a promising solution due to their reduced footprint, CMOS compatibility, low propagation losses, and operation in the telecom band. In this thesis, we report the generation and complete experimental characterization of entangled and heralded single photons produced via spontaneous four-wave mixing (SFWM) in an integrated Si_3N_4 microring resonator with a nominal quality factor of approximately 10^6.

To ensure accurate photon-source characterization, we first perform a full metrological analysis of the superconducting nanowire single-photon detectors (SNSPDs) used in the experiment. This includes detection efficiency calibration as well as a novel experimental investigation of the polarization dependence of the detection efficiency, for which we propose and validate a new quantitative model that links nanowire geometry and photon polarization alignment.

The microring source is experimentally assessed using both semiclassical and quantum figures of merit that are relevant for real-world quantum-network deployment. We report a photon-pair generation rate of $316(3)\,\mathrm{kHz/mW^2}$, a maximum coincidence-to-accidental ratio (CAR) of 3.6(3), and an intrinsic heralding efficiency of 0.862(5), demonstrating strong pair correlations.

Non-classicality is first evidenced through super-Poissonian marginal statistics and by measuring temporal cross-correlations that violate the Cauchy–Schwarz inequality across multiple resonator modes. The device is then validated as a heralded single-photon source by measuring a heralded second-order correlation value of $g_{\mathrm{h}}^{(2)}(0) = 0.113(10)$, well below the limit of 0.5 for the multiple-photon state. Time–energy entanglement is demonstrated using a Franson interferometric measurement, yielding a two-photon interference visibility of $V = 84(3)\,\%$, exceeding the CHSH inequality threshold of $70.7\,\%$ by more than four standard deviations, thus confirming the ability of the device to generate entangled photon pairs suitable for quantum information protocols.

A major original contribution of this thesis is the experimental demonstration of photon-coherence control through the resonator's operational regime. By tuning the laser-resonance distance via controlled variations of the laser wavelength, we achieve deterministic bandwidth engineering of the emitted SFWM photons over more than three orders of magnitude, from approximately 100 MHz down to 30 kHz. This result, previously unreported for integrated $\chi^{(3)}$ quantum sources, establishes a practical method for adapting a single source to heterogeneous quantum network architectures. Furthermore, we experimentally verify the continuous transition between the stimulated and spontaneous FWM regimes by demonstrating consistent bandwidth values obtained with both classical and quantum measurement methods.

Overall, this work provides not only a complete performance assessment of a $\chi^{(3)}$ microring quantum light source, but also key new insights into detector behavior, bandwidth tunability, and practical control parameters for chip-scale photon generation. The

demonstrated brightness, entanglement visibility, purity, and spectral agility position this platform as a strong candidate for integrated and deployable quantum network nodes, bridging fundamental studies and real-world quantum communication requirements.

Contents

Chapter 1

Introduction

Quantum Communication and Quantum Key Distribution have approached the industrial world and are currently being commercialized. But there is a need to develop superior technologies to exploit the quantum advantage effectively. On-chip and robust quantum light sources are a fundamental requirement in the development of real-life quantum networks. They allow for better scalability with the introduction of quantum routers and easier integration of new nodes [1].

Commercialized single and entangled photon sources [2, 3] are bulky and need a server rack or even an optical laboratory to be operated. Usually, second-order ($\chi^{(2)}$) optical non-linear materials are used, more specifically, Spontaneous Parametric Down Conversion (SPDC) [4–6]. $\chi^{(2)}$ crystals emit photons at a frequency which is half the frequency of the input photons; therefore, one is forced to use very different wavelength ranges, and it is not easy to remain in commercial telecommunication bands. An additional limitation is that SPDC sources have very broad emission spectra, up to the THz range [7, 8]. Which may not be compatible with the, usually, 100 GHz wide telecommunication channels.

There is a need to develop integrated, robust, telecom-band quantum light sources. In recent years, thanks to the evolution of micro-fabrication technologies, research has been focusing on integrating third-order ($\chi^{(3)}$) non-linear materials in microresonating structures [9–15].

Using $\chi^{(3)}$, it is possible to completely work within the telecom band, since the pump generates two photons with frequencies whose average is that of the pump light. Integrating these materials onto a photonic chip gives the possibility to scale the dimensions of a source to the mm or even μm scale.

Since second and third-order optical processes have, respectively, a second and third-order dependence on the electric field, for weak fields, the effect is feeble. Moreover, $\chi^{(2)}$ and $\chi^{(3)}$ have very low values with respect to the linear susceptibility [16, 17], thus these processes exhibit very low efficiencies and require intense optical fields. The role of the resonant structure, as the microresonators, is to achieve a higher interaction between the optical field and the gain medium, due to the trapping of the field. In this way, one can obtain the generation rates needed to work with a real-life optical fiber link. Additionally, the effect of the resonator is also to filter the output spectrum, allowing emission only at

the resonance wavelengths. Each resonance can easily have a linewidth of $\sim 200\,\mathrm{MHz}$, solving in this way the problem of the broad emission spectrum.

The main platforms exploited are Si_3N_4 [18], silicon-on-insulator (SOI) [19], and high-index doped silica, also called Hydex [20]. They offer promising features due to their high optical non-linearity and low non-linear losses. But most importantly, the possibility of integration and the compatibility with current CMOS technologies, which is crucial if we want to develop a commercial and cheap platform.

$\chi^{(3)}$-resonators offer additional advantages; first of all, they allow for a better understanding of quantum optics, and more specifically, of biphoton states [21]. Entangled states of light, even though predicted almost a century ago [22], have been completely demonstrated just ten years ago, with the first violations of the Bell inequality without any loophole [23, 24]. Therefore, even though researchers have been experimentally studying entanglement for many decades, the field is still at an early stage.

There is a need for the unification of the metrological definitions and characterization of single photon technologies [25], both sources and detectors. Some steps have already been made in this direction [26, 27], but more needs to be done to fully unify the community.

Microresonators with a $\chi^{(3)}$ material also have applications in other quantum technologies. In the quantum sensing field [28, 29], for example, researchers are trying to achieve an integrated and stabilized laser using a Si_3N_4 microring [30].

These devices also have widespread interest in building compact classical frequency combs. Exploiting the generation of photons over a wide $\chi^{(3)}$ spectrum and the filtering effect arising from the equally spaced resonances of the microcavity, it is possible to produce evenly spaced narrow frequency lines. Combs are developed for the field of high-speed communication in data centers [31], where each line of the resonator is exploited as an optical carrier within the DWDM (Dense Wavelength Division Multiplexing) architecture, which is the standard in telecommunication. In addition, they generate great interest also in the atomic clock community, since they are also a fundamental requirement in the design of compact optical clocks [32, 33]. The possibility to integrate a frequency comb will allow mounting optical clocks in airplanes and satellites, providing numerous advantages such as higher precision GNSS service (such as GPS), military applications, and high precision spectroscopy. Moreover, a current commercial frequency comb is an expensive and complex device [34, 35], costing around a hundred thousand euros, while a photonic chip pumped with a laser is definitely a cheaper option.

In this thesis, we present the generation and characterization of entangled states of light from within a Si_3N_4 microring. We demonstrate the possibility of using such a device as an entangled-photon and heralded single-photon source for quantum communication applications. The work was carried out at the Italian National Metrology Institute INRiM. We show a qualitative theoretical analysis of the different properties and propose a full characterization. We want to give a complete overview of the parameters, their roles, and their meaning in the generation of quantum states of light. This report is constructed following a technical approach, where each chapter introduces a fundamental argument regarding the work, presenting both theory and experimental results. More in detail, the manuscript is structured as follows.

In the second chapter *Experimental setup*, we describe the experimental setup. We start by focusing on the section of the experiment related to the generation and pumping stage. Then the focus moves on to cavity theory and the main metrics describing the behavior of these devices. Then we scale down the dimensions, introducing microresonators, and show the additional challenges that must be faced with μm scale devices, such as compensating the red shifts of the resonances when optical power is coupled into the device. To conclude the description of the microring and the generation stage, we present a characterization of two fundamental properties of the device: linewidth and Free Spectral Range (FSR), and perform simulations about the dispersivity of the device. We demonstrate how our microring exhibits optimal properties to integrate it into a real-life telecommunication infrastructure.

Afterward, we move to the detection part of the experimental setup, which is a set of Superconducting Nanowire Single Photon Detectors (SNSPDs). The devices' theory and working principles are described in order to sustain the metrological characterization presented next. We performed a careful study of the detection efficiency η as a function of the number of photons reaching the detectors. This is a common practice to extrapolate the "zero-flux efficiency" η_0, which is the parameter of most interest in the metrological community [27]. Because it does not depend on any experimental condition other than the photon's wavelength. After that, we studied the detection efficiency polarization dependence, which is a phenomenon related to the geometry of the nanowires. We introduce a novel measurement technique not found in the literature yet, and present its demonstration through experimental results.

The second chapter, namely *Entangled states generation process: Four-Wave Mixing*, focuses mainly on the light generation process. We introduce the theory of optical nonlinearities and how they are quantitatively described in a medium. Then we close the focus on the third-order non-linearity of our interest: Four-Wave Mixing (FWM). We start describing its working principle in the classical regime, which we will call stimulated FWM, and the conditions it needs to arise. We describe how FWM behaves in microresonators and introduce the concept of the Optical Parametric Oscillator (OPO). Afterward, we move to the quantum regime of FWM, which we will call spontaneous FWM (SFWM), and the quantum state generated by it, underlining how this state can exhibit entanglement.

Then, we give a qualitative description of the frequency comb regimes that can be obtained working with a $\chi^{(3)}$ medium integrated in a resonant geometry. We support the latter statements with qualitative experimental observations and MATLAB simulations. This is important to comprehend how many different output spectra can be generated, and what operational conditions are necessary to produce stable and coherent Kerr combs for semi-classical applications.

To conclude the chapter, we evaluate important metrics that are strictly linked to the SFWM process and the source. We start measuring the photon-pair generation rate, which defines how many correlated photons are generated for a given amount of input power. Then, we present a parameter analogous to the Signal-to-Noise Ratio (SNR), which is the Coincidence-to-Accidental Ratio (CAR). It measures the amount of measured "good" (correlated) photon pairs with respect to the "bad" ones, the latter are

composed of background and environmental light, and detector dark counts. The CAR is fundamental when designing a quantum network since it is also a setup-sensitive metric. Using the data and the results obtained from the last measurements, we present the evaluation of the heralding efficiency, which describes the probability that a photon, at the detectors or at the source, is paired with a correlated counterpart, and that the latter is not lost or absorbed by the environment. These three parameters are keys to the evaluation of a heralded single-photon or entangled-photon source oriented toward a real-life quantum communication infrastructure.

The third chapter *Entangled states characterization* focuses on the quantum mechanical properties of the generated photons. First, we study the temporal correlations within only one of the two output photon channels, namely the autocorrelation. We provide the theory of such a measurement and underline how the temporal behavior is strictly linked to the spectral properties of the photon. We present how it is possible to obtain an insight into the biphoton density matrix purity simply by studying the temporal behavior within a single emitted mode. Then, we reproduce the same measurement, but studying the temporal correlations between the two correlated photons. We, again, underline the strong relationship with the biphoton spectral properties and link the results to the autocorrelation. We confirm the non-classical correlations within the SFWM photon pair by violating the Cauchy-Schwarz inequality. These two measurements show the strong link between the temporal and spectral properties of the single and biphoton states and give an insight into the properties of the quantum state, such as the density matrix purity or the coherence time.

Then, we show the ability to use the device as a heralded single-photon source by demonstrating that the single-photon nature can be unveiled from the biphoton state generated with SFWM. We use the heralded second-order correlation, which is the extension of the autocorrelation measurement, but it is able to project the biphoton state onto a single-photon wavefunction and uncover its single-particle nature. In the final part of the chapter, we describe more in depth time-energy entanglement and how it can arise from the biphoton state generated by SFWM. We demonstrate that our device is able to exhibit this type of entanglement using a Franson interferometric measurement, which is a non-loophole-free violation of the CHSH inequality. These last two measurements are fundamental in order to establish and state that our source is able to emit single or entangled photons, which are key requirements for quantum communication protocols.

We, then, present the fifth chapter, *Coherence time and detuning*, which describes a novel experimental study of the photons' behavior generated in a $\chi^{(3)}$ integrated quantum light source. This section is also based on some results that are the core of an article in preparation. We study the dependence of the emitted photons' bandwidth during the evolution of the operational regime. We show how, by tuning the circulating power within the microring, it is possible to modify the bandwidth by over three orders of magnitude, from $\sim 100\,\mathrm{MHz}$ to $\sim 30\,\mathrm{kHz}$. This work is important for two reasons:

- It provides a novel technique for tuning the photon's bandwidth;
- It links the properties of the light in the stimulated and classical regimes with those in the quantum realm.

The first reason gives an additional tool for optimizing the light coherence properties when integrating the device in a real-life network, where various components with different coherence requirements may be present. In the second reason, we are showing that quantum and classical physics are just different representations of the same phenomenon, simply on different scales. And it is possible to study the transition between quantum phenomena and the classical world.

To perform such a study, we had to demonstrate that the photon bandwidth measurement in the quantum and classical regimes returned the same quantity. To do so, we introduced a third approach that allows us to create a bridge measurement between the two. Moreover, we also exploited advanced physics concepts, such as laser locking, in order to achieve these results and sustain them with experimental evidence.

In the sixth the conclusive chapter, we present and summarize the work done in this thesis, listing the main achievements and how they can be exploited in a real-life environment. Then, we underline some limitations in our study and our device, and present possible solutions to overcome such problems. To conclude, we give an overlook of what can be done in the future to improve the field of $\chi^{(3)}$ integrated quantum light sources to develop these technologies further and to achieve the previously mentioned applications.

Chapter 2

Experimental setup

In this chapter, we describe the experimental apparatus, as shown in Fig. 2.1, which divides the system into two main sections: the photon-pair generation stage and the detection stage. The first section consists of a continuous-wave (CW) pump laser coupled to a Si_3N_4 microring resonator. Within which, through an optical non-linear process, better described in Sec. 3.3, we are generating the entangled photons. We provide a detailed characterization of this key component, as it plays a central role in the process of photon-pair generation. The second section comprises filtering and connection to Superconducting Nanowire Single Photon Detectors (SNSPDs). The performance and characterization of the latter are also discussed in detail.

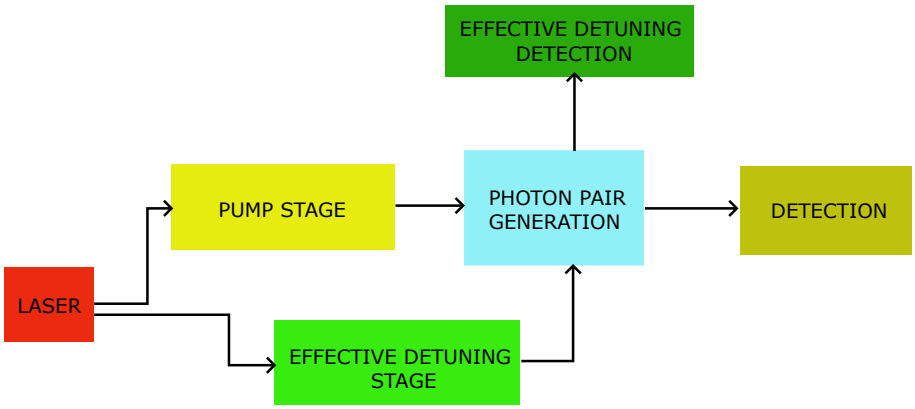

Figure 2.1: Visual scheme of the experimental setup.

2.1 Microresonator

2.1.1 Description of generation stage

The pump laser is a RIO Planex 1550nm centered at $\lambda_P = 1543.7\,\text{nm}$, tunable over a 35 GHz range, linewidth of $\Delta\nu = 30\,\text{kHz}$, controlled by a QUBECL system. The laser is typically operated at a current of 76 mA and a temperature range of 17 °C to 21 °C. After

an optical isolator, placed to avoid back reflections directly into the diode, the pump light is split by a 95/5 splitter. The 95 % is used for measuring the effective detuning between the pump frequency and the microresonator resonance, as described later in the chapter. The 5 % is amplified by a Continuous Erbium-doped Fiber Amplifier (CEFA) (CEFA-C-PB-HP by Keopsys) typically operated with 250 mW output power. The amplified light is then filtered by a fiber-coupled DWDM filter (C-band WDM filter by Fiberdyne Labs) with 0.8 nm bandwidth, and with a 30 dB rejection of frequencies outside the pass-band. This filter is inserted in order to remove the noise generated by the CEFA, the Amplified Spontaneous Emission (ASE) noise, before entering the microring. One of the strongest limitations of this filter is the presence of ripples, which are ranges where the pass-band is non-zero even though they are outside the specified DWDM channel. These ripples are populated with ASE light generated by the CEFA and are detrimental when trying to work with quantum states of light, since they increase background photons.

Such amplified and filtered light is then coupled to an integrated chip. Note, to better couple light inside the photonic waveguide, one must match the propagation mode of the waveguide with the pump light. To do so, we exploited a polarization controller (PC), which modifies the polarization of the light to better couple with the waveguide. This integrated chip was manufactured by Ligentec and contains 16 microrings, see Fig. 2.3b, all of which are made of silicon nitride Si_3N_4. The generation stage is depicted in Fig. 2.2.

Silicon nitride was chosen because of low losses, high third-order non-linearity, negligible non-linear loss at telecom wavelengths, and compatibility with CMOS fabrication processes [36]. These features make silicon nitride microresonators a highly efficient platform to exploit non-linear optics.

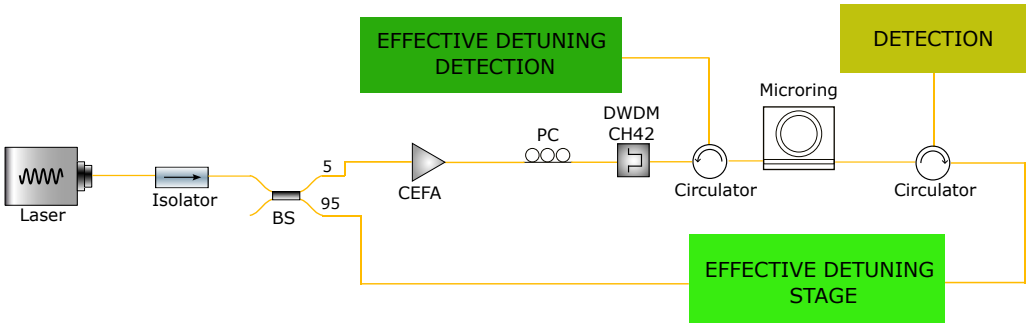

Figure 2.2: Experimental setup of the generation and pumping stage. *PC*: paddle for polarization control, *BS*: beam-splitter splitting the input power in percentages written on the output arms, *DWDM CH42*: DWDM filters working in channel 42, centered at 1543.7 nm and wide 0.8 nm.

The 16 rings on the chip are divided into two sets or rings characterized by different nominal diameters, 185 μm and 270 μm. Furthermore, each ring is fabricated at a distance d from a Si_3N_4 straight waveguide to which it can evanescently couple. The strength of the coupling depends on d and can vary from under- to over-coupled [37]. For the work carried out in this thesis, we selected a single ring with a nominal ring radius of 185 μm and waveguide-ring coupling distance $d = 0.5\,\mu$m. The section of the waveguide has a

rectangular shape of width 1.6 μm and height 0.8 μm. Its characterization is presented later in the chapter.

The substrate on which the photonic circuit is built is made of SiO_2; the difference in refractive index between Si_3N_4 and SiO_2 confines the radiation inside the waveguides. The presence of the straight waveguide allows for coupling of the external pump light into the photonic chip.

2.1.2 Resonators' theory

The microring functions as a resonator for the pump light. An optical resonator is a device that stores radiation and, due to resonance, can contain powerful fields at specific frequencies, while completely blocking all the other wavelengths. A well-known example of an optical resonator is the Fabry–Pérot cavity [38], where light is confined between two parallel, reflective mirrors, leading to constructive interference at resonant frequencies. The resonant frequencies are defined by the cavity geometry, and they are selected by the condition that the accumulated phase shift over a round-trip equals an integer multiple n of 2π [39]. All the radiation at non-resonant frequencies is eliminated by destructive interference. The resonant field within the cavity is actually a standing wave, since it is a balanced superposition of two identical fields going in opposite directions. If the reflective part of the cavity is 100 % reflective, the radiation is ideally stored infinitely. To extract part of the stored light, the idea is to make the reflective components partly transmitting.

Similarly, in microring resonators, confinement is achieved not through discrete mirrors but through total internal reflection enabled by the circular waveguide geometry. This geometry imposes boundary conditions that allow for resonant enhancement of specific wavelengths, analogous to Fabry–Pérot resonators but in a compact, integrated form.

Before presenting the specific characteristics of our device, we first introduce key concepts relevant to resonator performance and operational regimes.

Resonant circulating radiation is enhanced due to constructive interference; we describe this effect by the ratio of the circulating and input fields, by a factor [39]:

$$\Gamma_{\text{circ}} = \frac{I_{\text{circ}}}{I_0} = \frac{Finesse}{\pi} \tag{2.1}$$

where I_{circ} is the circulating power and I_0 is the intensity that is coupled from the bus to the ring waveguide [40]. The $Finesse$ is defined as:

$$Finesse = \frac{FSR}{\Delta\nu}, \tag{2.2}$$

where FSR (Free Spectral Range) is the distance between two neighboring resonances ($^{n}\nu$ and $^{n+1}\nu$) and $\Delta\nu$ is the cavity linewidth, see Eq. (2.4). The FSR can be linked to the ring radius R by [41]:

$$FSR = \frac{c}{2\pi n_{\text{eff}} R} \tag{2.3}$$

where n_{eff} is the effective refractive index of the cavity. Therefore, the ring dimensions are crucial for defining the spectral distribution of the resonances and cannot be freely tuned.

In microresonators, this enhancement of optical radiation is fundamental in order to exploit non-linear optical processes, since they depend on the electromagnetic field intensity. Losses in the cavity materials and imperfections are responsible for a non-zero resonance linewidth $\Delta\nu$, which is defined as the full width at half maximum ($FWHM$) of the resonance, which has a characteristic Lorentzian profile. The $FWHM$ of a cavity is also related to the photon lifetime τ_{L} inside the resonator [39, 42]:

$$\Delta\nu = FWHM = \frac{1}{2\pi\tau_{\mathrm{L}}}. \tag{2.4}$$

where τ_{L} describes the average time a photon spends inside the resonator. It is therefore directly proportional to the enhancement factor $\Gamma_{\mathrm{circ}} \propto \tau_{\mathrm{L}}$, as demonstrated using Eq. (2.1) and (2.4). The last relevant parameter introduced here is the quality factor Q:

$$Q = \frac{\nu}{\Delta\nu} \tag{2.5}$$

where ν is a resonant frequency. This parameter describes the ratio between the frequency and the bandwidth of oscillation frequencies.

Now that the main resonator-related quantities have been introduced, we can introduce some features of our resonator.

Light is coupled on the chip by using lensed fibers at the input and output of the chosen waveguide. Such fibers have a smoothed end, which acts as a collimator; therefore, it is easier to focus the laser beam, matching the chip waveguide core dimension. Fiber-to-chip coupling is optimized with two translation stages (one at the input and the other at the output), each controlling the position of the fiber in the three axes x, y, z. This control allows for a fine-tuning of the coupling point and readjustment when needed.

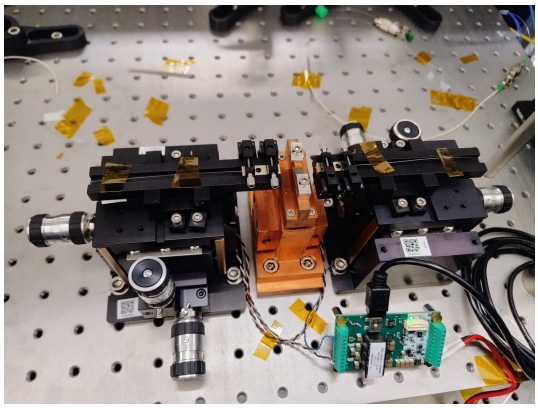

(a) Mechanical apparatus coupling the optical fibers to the microchip.

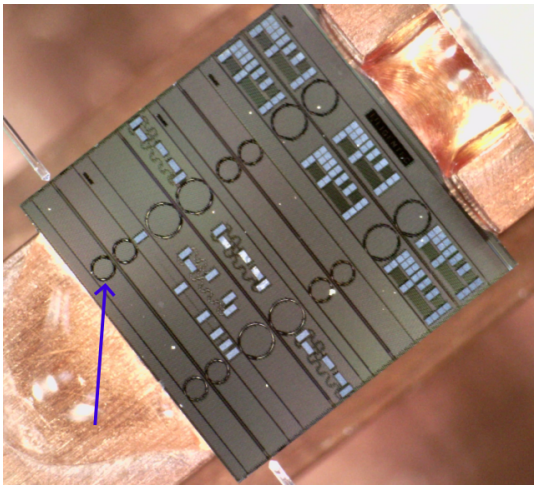

(b) Image of the microchip taken with a Dino-Lite digital microscope. The blue arrow indicates the ring of interest.

Figure 2.3

The ring-shaped waveguide is designed to work in an anomalous dispersion regime [43] around the telecom C-band, and the nominal quality factor is $Q \sim 10^6$.

2.1.3 Thermal effects in Kerr-microresonators

In microresonators, thermal effects are non-negligible, since the power circulating is $\sim 50\,\mathrm{W}$, at $\lambda_P = 1550\,\mathrm{nm}$, in a small region, it generates a high temperature increase. The main thermal effects are the change in the refractive index and the deformation of the spatial geometry. The main result is a red shift of the resonant frequency, in Si_3N_4 material, of the order of $\sim 5\,\mathrm{GHz/°C}$ [44, 45], additionally, the FSR is changed. Heating the ring will increase R, thus increasing the optical path, reducing the FSR (see Eq. (2.3)). The resonance distance can change by orders of $\sim 300\,\mathrm{MHz}$ [44], which is usually a deviation less than $0.5\,\%$ with respect to the cold temperature value ($\sim 10^5\,\mathrm{MHz}$).

A consequence of these non-negligible thermal effects is an asymmetric approach to resonance, with the system responding differently depending on whether the frequency is swept from below or above the resonator's resonance. As the input frequency approaches resonance, the intracavity power increases, gradually heating the ring and causing a red shift of the resonant frequency. As a result, it is easier to reach resonance when sweeping from higher to lower frequencies. This is called "forward tuning" [46]. Working in this direction can also allow for thermal self-locking of the resonance on the pump laser [46]. The opposite approach, from low to high frequencies, is called "backward tuning", and hardly reaches an equilibrium point, since the resonance shifts towards the pump and can eventually "jump" it (cooling very fast when resonance is passed). The behavior described above results in a hysteretic response in the transmission observed at the output of the photonic chip when scanning the frequency around the micro-ring resonator resonance, see Fig. 2.4.

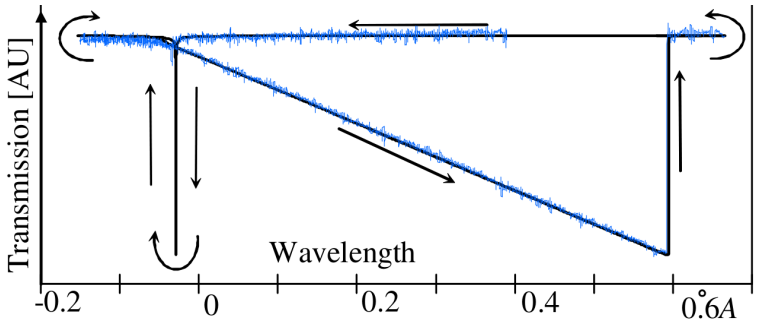

Figure 2.4: Hysteretic behavior of the transmission of a micro-ring resonator. When forward tuning, the resonance red-shifts until a maximum point, thus creating a triangular response. Back tuning returns a narrow, distorted response. Image taken from [47].

The maximum shift experienced by the ring when forward tuning (the higher edge of the triangle in the figure) depends on the power pumped into the ring. For low input power, it is possible to retrieve the characteristic Lorentzian lineshape, because there is

not enough heat transfer to change the resonance position. For very high pump power, it is possible to shift the resonance for hundreds of FWHM [48].

In summary, when the pump is detuned from the resonance, no light is coupled to the ring, and the heating is limited. Reducing the detuning, light starts circulating in the cavity, and due to the enhancement effect, the ring is heated. The latter generates both a change in FSR and a shift of the resonance toward higher wavelengths, thus increasing the detuning of the pump and reducing the circulating power and heat. Due to this dynamical behavior, we built an experimental section to monitor the instantaneous detuning between the pump frequency and the microresonator "hot" resonance (shifting with respect to the original one). We call this detuning "effective detuning" δ_{eff}.

Effective detuning monitoring

In Fig. 2.5, we show the setup developed to monitor the δ_{eff} in real time during the experiments.

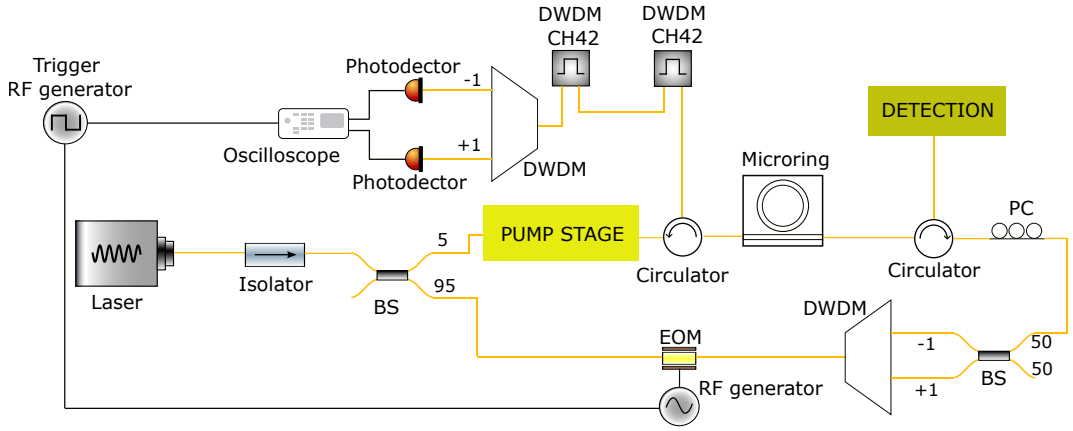

Figure 2.5: Experimental setup used for the measurement of the effective detuning. Note that the two DWDM filters are working in reflection; thus, they are effectively filtering radiation in channel 42, which is the one where the ring is pumped. Both the DWDM demultiplexers are used to select the channel where the sideband is located. *DWDM*: DWDM demultiplexer, *EOM*: electro-optic modulator.

The pump laser is tuned to pump the mode 0, while the 5 % is amplified to be coupled to the ring, the 95 % is used for measuring δ_{eff}. The measurement idea is to insert into the ring a low-power component resonant with the neighboring modes ± 1 at a distance $f_{\pm 1}$ from the pump frequency. As the pump is scanned, the distance $f_{\pm 1}$ is changed to keep the component resonant. At the same time, monitoring two resonances, we can measure the temporal variation of the FSR (with the assumption that $FSR_{0:+1} = FSR_{-1:0}$). Knowing this, for every point we get:

$$\delta_{\text{eff}} = f_{+1} - FSR = FSR - f_{-1} = f_{\text{p}} - f_0 \tag{2.6}$$

where f_{p} is the pump frequency and f_0 is the frequency of the resonance that is being pumped. Note that we are interested in measuring δ_{eff} close to resonance, where $f_{\pm 1}$

approaches FSR.

This technique is inspired by the work by Kippenberg et al. [48]. However, while in their work, a sideband on the pump laser is used to directly probe the main pumped resonance, we probed the two neighboring modes, see Fig. 2.6. We chose a different approach due to difficulties in reproducing the measurement, as well as the absence of a Vector Network Analyzer (VNA) in our laboratory, which is a requirement.

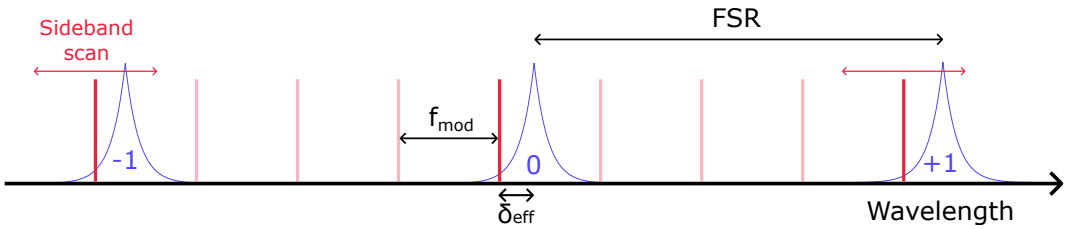

Figure 2.6: Visual representation of the technique used to measure the δ_{eff}. In blue, the resonator resonance. The central red line represents the pump component, and all the other red lines are the sidebands generated by the EOM. f_{mod} is the RF modulation frequency, which is swept to completely cover the resonances with the 4^{th} sidebands.

The "monitoring" components are generated by an electro-optic modulator (EOM), specifically the MPZ-LN-40 by Exail. An EOM is a device that changes, following an RF signal, the refractive index of the material through which light is flowing, in this case $LiNbO_3$. The temporal change in refractive index generates symmetric frequency components separated by the original frequency by the modulation frequency. By increasing the power of the RF modulation signal, it is possible to generate higher-order sidebands. They appear at n (n is the order of the sideband) frequency of modulation distant from the main component. Given the upper limit of 40 GHz (from datasheet), we are not able to work at hundreds of GHZ of modulation (comparable with the FSR); therefore, we used a higher order sideband. In particular, modulating around 37.5 GHz we can use the fourth-order sideband to reach the nominal FSR distance. Instead of choosing a single value for the modulating frequency, we opted for a wide ramp scanning through the resonance to monitor the whole resonance feature. After the EOM, the fourth-order sidebands are selected by the use of a multi-channel DWDM (Dense Wavelength Division Multiplexer). The selected channels are 41 and 43, respectively centered at 1542.9 nm and 1544.5 nm (both are 0.8 nm wide). The so filtered components are then recombined using a 50/50 splitter before entering the chip. The power of these monitoring components is of the order of 0.5 mW, low enough not to introduce additional thermal shifts. We chose to employ two circulators to inject the monitoring components into the chip opposite the pump input. In this way, we can measure the detuning while performing the experiment. After exiting by the output circulator, the monitoring light is filtered by two DWDM filters to remove the light component due to the reflected pump coming from the opposite direction. Such filters are centered around the mode 0 DWDM-channel (channel 42 centered at 1543.7 nm) and are used in reflection, thus suppressing frequencies centered around channel 42. Lastly, a DWDM demultiplexer retrieves radiation around modes ± 1, which are then directed onto two photodiodes (ET-3010EXT by Coherent) and acquired

through an oscilloscope, see Fig. 2.7.

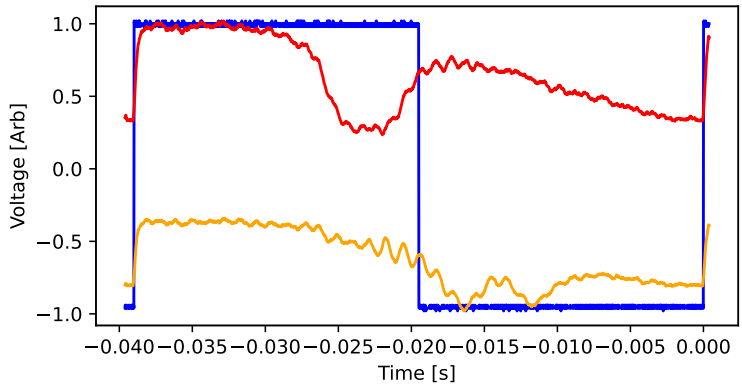

Figure 2.7: Sweep of resonant profile of modes ±1 of the microring. In blue, the trigger signal used to start the frequency sweep and to precisely define the start time point. In red, the transmission signal of mode -1^{th}. In orange, the transmission signal of mode $+1^{\text{th}}$. The scan frequency in the figure is scanned from 35.5 GHz to 35.8 GHz. Since working with the fourth-order sideband, the effective scan is from 142 GHz to 143.2 GHz. Note, the oscillations on the transmission signals are due to a residual interference happening at the recombination of the two wavelengths (mode ±1) before entering the photonic chip.

Starting from Fig. 2.7, it is possible to calculate the effective detuning. First, we need to identify the starting point on the time axis that corresponds to the start of the frequency scan, t_{start}. For this, we used a trigger signal, which defined such a point with its rising edge (red curve). Then, using a fit curve with two Lorentzians, we define the resonance center on the time axis, t_{+1} and t_{-1}. Assuming that the RF generator swept from $f_{\text{start}} = 35.5\,\text{GHz}$ to $f_{\text{stop}} = 35.8\,\text{GHz}$ (typical values for the scan) in $t_{\text{duration}} = 40\,\text{ms}$, we can calculate the factor $K = 4 \cdot (f_{\text{stop}} - f_{\text{start}})/t_{\text{duration}}$ (note the coefficient 4 is necessary since we are working with the fourth-order sideband). Now, we can calculate the exact frequency that separates the pump from the neighboring resonances with $f_{+1(-1)} = 4f_{\text{start}} + K(t_{+1(-1)} - t_{\text{start}})$. Summing these values, we obtain an estimation of $f_{+1} + f_{-1} = 2 \cdot FSR$; this is an assumption based on the almost zero dispersion in such a small frequency range. Knowing the FSR and the sideband distance, it is immediate to calculate the distance between the pump and mode 0 with: $\delta_{\text{eff}} = f_{+1} - FSR = FSR - f_{-1} = (f_{+1} - f_{-1})/2$.

Note, in some of the following measurements, we did not use two sidebands to monitor both neighboring resonances. We, instead, considered an FSR measured a priori and observed only a single sideband. This approach is still acceptable since the FSR does not change much when coupling light within the resonator. In Fig. 2.8, we demonstrate the earlier statement, in fact in the figure we reported the variation of the FSR with respect to FSR_0, which is the value obtained for a laser temperature of 19.1 °C ($\delta_{\text{eff}} \approx 155\,\text{MHz}$). We can tune the laser frequency by changing the device's temperature, which modifies the laser's cavity length, thus affecting the emission wavelength. At FSR_0 light coupled within the microring is just a few, and a little spontaneous emission can

be measured, while for temperatures $> 20.0\,°\mathrm{C}$ we are approaching the OPO threshold. From the data, we see that the Free-Spectra Range has fluctuations of $\sim 10\,\mathrm{kHz}$, which are not detrimental for our measurements. We need precisions of the order of $\sim 1\,\mathrm{MHz}$, since the resonator linewidth is $\sim 100\,\mathrm{MHz}$.

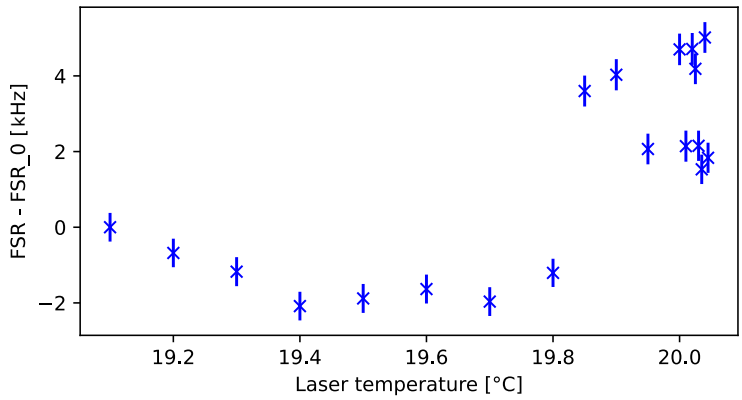

Figure 2.8: Change of the FSR with respect to the value measured using a laser temperature of $19.1\,°\mathrm{C}$ which corresponds to a $\delta_{\mathrm{eff}} \approx 155\,\mathrm{MHz}$. Note that increasing the temperature of the laser the wavelength also increases, which means we are approaching the resonance.

An interesting effect is that the effective detuning is linearly decreasing when tuning the laser wavelength far from resonance, as shown in Fig. 2.9. Meaning that the laser is moving toward the resonator mode. While closely approaching the resonant point, δ_{eff} changes very slowly, which means that the resonance is also moving with the laser. Therefore, confirming the shift of the resonances when light is coupled into the ring. Note how the δ_{eff} almost stops decreasing at around $\lambda_{\mathrm{P}} \approx 1543.655\,\mathrm{nm}$. This occurs when power starts circulating inside the resonator, effectively heating it and shifting the resonance.

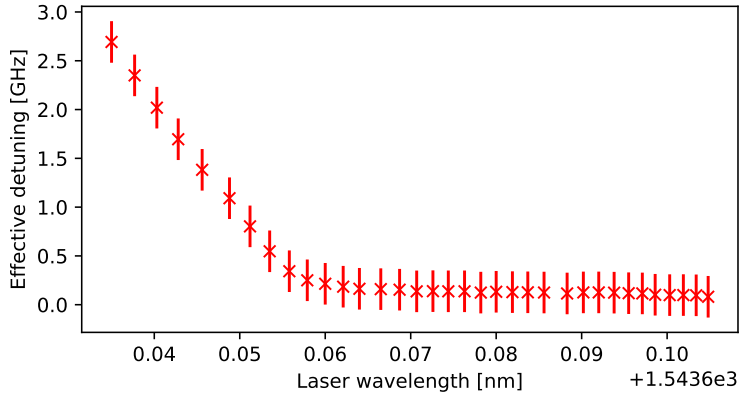

(a) Complete scan.

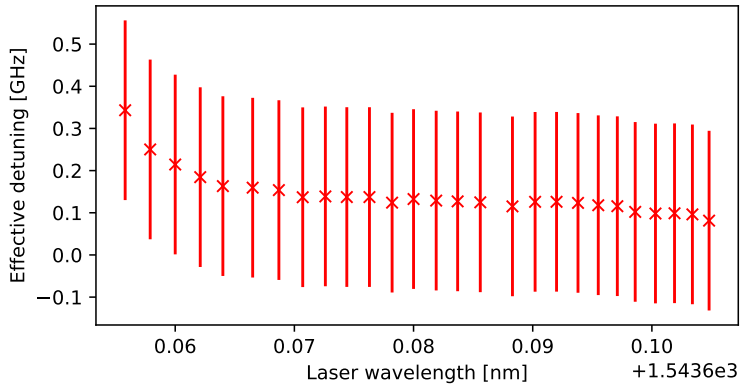

(b) Zoom when the δ_{eff} almost stops to decreasing, $\lambda_{\text{P}} > 1543.655\,\text{nm}$.

Figure 2.9: Effective detuning as a function of the laser pump when approaching resonance from lower to higher wavelengths.

2.1.4 Characterization

We experimentally characterized the linewidth $\Delta\nu$ and FSR, which nominally is 150 GHz, of the resonator, while the effective refractive index and effective area were simulated using the software COMSOL, thanks to the help of Dr. Chiara Gionco from INRiM. The effective area is a parameter describing how the electromagnetic field is spatially confined inside the photonic waveguide. Note that the measurement of the effective detuning as described in Sec. 2.1.3 is not necessary here.

Linewidth

The linewidth has been measured by pumping the cavity with low power ($\sim 5\,\text{mW}$), in order not to distort the resonance profile. In diode lasers, modifying the pump current, the carrier density changes, as well as the optical susceptibility χ of the gain medium. Since the emission frequency depends on the material χ, one can tune the emission

frequency of a laser by controlling the driving current. We modulate the laser current using an RF signal generator to generate a frequency sweep around the resonance. The transmission exiting the ring is directed onto a photodiode, and its response is detected by an oscilloscope.

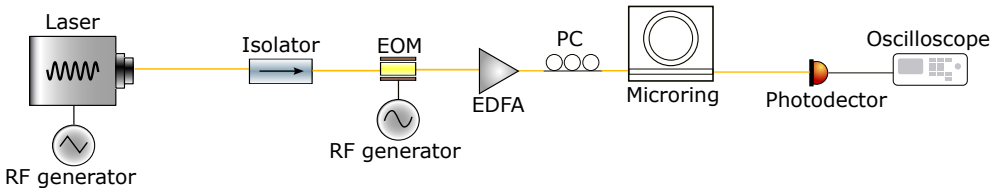

Figure 2.10: Experimental setup for the cavity linewidth measurement. *EDFA*: Erbium-Doped Fiber Amplifier.

In Fig. 2.10, we show the simple setup employed. The modulation is a triangular wave at 100 Hz emitted by an RF signal generator. The amplitude defines the frequency range in which the modulation changes the laser emission. We tuned the modulation amplitude and obtained a frequency scan of 1.5 GHz, large enough to contain the complete resonance profile. The triangular wave is important to obtain a linear change of the frequency during a single edge of the modulation. The EDFA is useful for achieving precise control of the power entering the chip and for reducing amplitude modulations. A sideband placed at a well-known frequency, imprinted by an EOM connected before the EDFA, is used for frequency calibration.

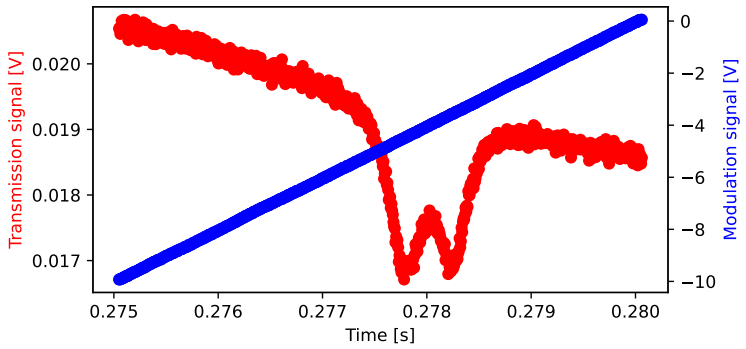

(a) No sidebands.

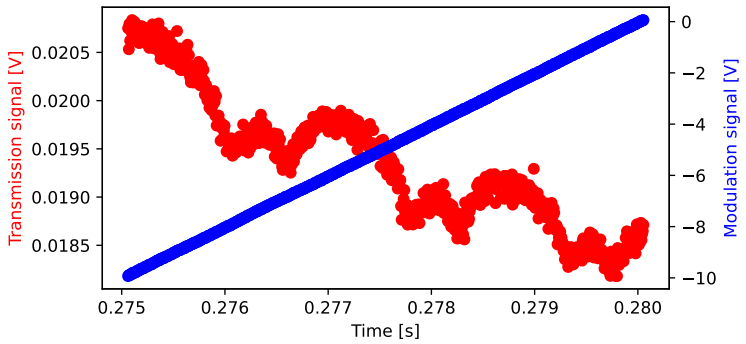

(b) With calibration sidebands generated with the EOM.

Figure 2.11: Example of signal measured on the oscilloscope. In red, the transmission signal detected by the photodiode. In blue, the modulation ramp.

Generating sidebands on the pump laser has the effect shown in Fig. 2.11b: the pump transmission is depleted and two symmetrical resonance profiles appear. Dividing the RF modulation frequency of the EOM by the distance between the central peak and the side peaks (on the oscilloscope), we get a calibration factor to turn the time axis into a frequency axis. This conversion is possible only if the frequency variation during a sweep is linear. Usually, the frequency response of a directly modulated laser is not linear. Changing the driving current also modifies the device's temperature, thereby altering its output wavelength. Moreover, the increased pump injected into the Kerr resonator changes its refractive index, which also modifies the frequency. But if we keep the sweep small enough, the linearity assumption holds.

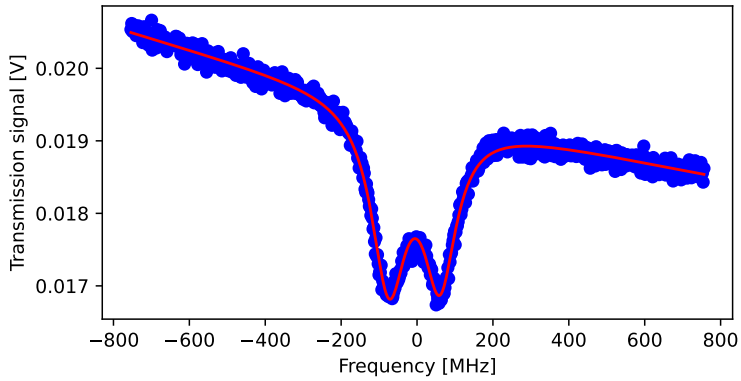

Figure 2.12: Transmission spectrum as a function of the pump frequency sweep, centered around the resonant frequency. In blue, the experimental points. In red, the double Lorentzian fit. The fit parameters are (see Eq. (2.7)) $x_{0,1} = -74.2(5)\,\mathrm{MHz}$, $x_{0,2} = 62.1(5)\,\mathrm{MHz}$, $\Delta\nu_1 = 112.3(16)\,\mathrm{MHz}$, $\Delta\nu_2 = 105.7(19)\,\mathrm{MHz}$, $A_1 = -0.434(6)\,\mathrm{V}$, $A_2 = -0.346(6)\,\mathrm{V}$, $a = -1.300(7) \times 10^{-6}\,\mathrm{V/MHz}$, and $b = 1.9478(4) \times 10^{-2}\,\mathrm{V}$

In Fig. 2.12 we show the transmission spectrum as a function of the modulation frequency. The absorption dip, in the presence of counter-propagating waves due to surface roughness in the waveguide, is lowered and split into two sub-resonances [49]. This effect is strongly dependent on the fabrication quality of the resonator. The midpoint between the two sub-resonances corresponds to the original resonance frequency. However, not all resonances exhibit a double Lorentzian lineshape; qualitatively, approximately half display a single Lorentzian dip. The reason for this is still under study. To model the splitting, we used the fitting function:

$$f = ax + b + \sum_{i=1}^{2} \frac{A_i}{2\pi} \frac{\Delta\nu_i}{(\Delta\nu_i/2)^2 + (x - x_{0,i})^2} \tag{2.7}$$

where the linear part fits the background and the Lorentzians fit the cavity resonance, $\Delta\nu_i$ describes the linewidth and coincides with the $FWHM$ of the resonance.

The two linewidths were evaluated to be $\Delta\nu_1 = 106(9)\,\mathrm{MHz}$ and $\Delta\nu_2 = 115(14)\,\mathrm{MHz}$ (lower and higher frequency). The two linewidths are compatible within a standard deviation, which is in agreement with the theory [21, 49]. Since the quality factor is a property of the whole resonator, and the resonances are close in frequency, we can state that they must show the same $\Delta\nu$. Moreover, the resonance splitting was estimated to be $\Delta\nu_2 - \Delta\nu_1 = 137(6)\,\mathrm{MHz}$. The uncertainties were evaluated using the standard deviation of the sample mean over 11 independent measurements. With these values, it is possible to calculate the quality factor using Eq. (2.5), where the absolute frequency of the pump laser at resonance is measured with the wavemeter 621A from Bristol Instruments. Since the instrument uncertainty ($\sim 150\,\mathrm{MHz}$) is larger than the resonance spacing, one can assume that the two resonances are at the same frequency of $\nu = 194\,242.81(15)\,\mathrm{GHz}$ or $1543.3902(12)\,\mathrm{nm}$. The resulting quality factors are $Q_1 = 1.83(15) \times 10^6$ and $Q_2 = 1.7(2) \times 10^6$. We must point out that we did not measure the microring quality factors;

we measured the Q of the ring and waveguide system. The ring Q should be higher since additional losses are added by the straight waveguide. But, due to critical coupling, or near-critical coupling, the two quality factors almost coincide. The uncertainty on the quality factor was estimated by propagating the uncertainty of $\Delta\nu$ and ν. These results align well with the values found in the literature for Si_3N_4 microring used in quantum information processes and entangled photons generation [50, 51].

Free-Spectral Range

We now describe the characterization of the FSR, setup shown in Fig. 2.14. To be able to perform wide frequency scans, a continuously tunable laser by Toptica at low power (to neglect thermal shifts) was employed. The frequency of the laser is set between two resonant modes n, n+1, then using an electro-optic modulator, we generated frequency sidebands separated by $\sim$ 35 GHz. This allows for the second-order sidebands to be resonant with mode n and mode n+1, see Fig. 2.13. We swept the frequency of the EOM to probe the cavity modes.

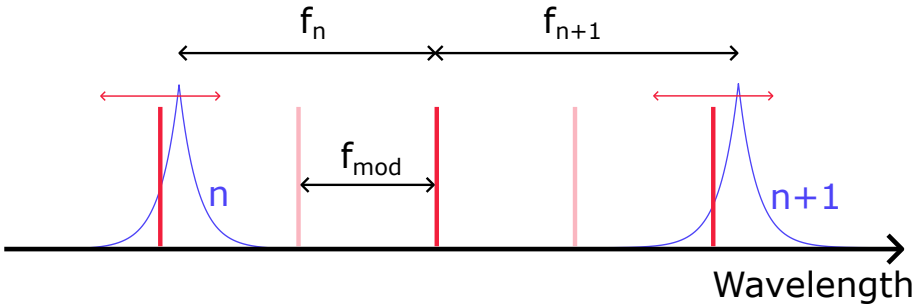

Figure 2.13: Visual representation of the measurement of the FSR. The central red line is the pump frequency component, while all the others are the sidebands generated by the EOM. The FSR is obtained as $f_{\mathrm{n}} + f_{\mathrm{n+1}} = FSR$.

The modulated light is then coupled into the chip. The transmission of the system is filtered (mainly to remove the 0^{th} order component that would blind the photodiodes) using a commercial DWDM demultiplexer to select the signals relative to the two neighboring resonances. The signals are then recombined, sent to a photodiode whose output is monitored on an oscilloscope, see Fig. 2.15.

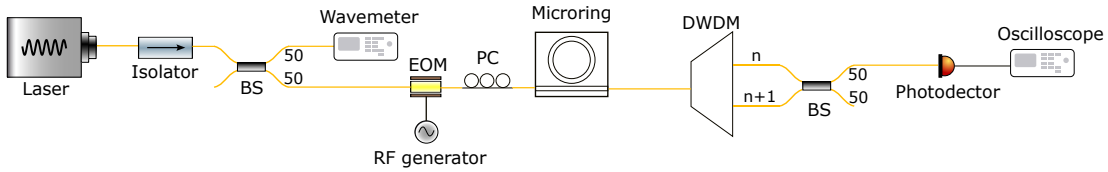

Figure 2.14: Experimental setup used for the characterization of the Free Spectral Range.

Both resonances' dips are shown in the same sweep if the frequency scan is properly set. To define which resonance is which, one just needs to unplug one of the two signals

from the DWDM demultiplexer and monitor which profile remains. The data analysis is analogous to the one performed to estimate δ_{eff}, with the exception of the presence of the trigger that requires a manual identification of the start of the scan (see yellow cross in figure).

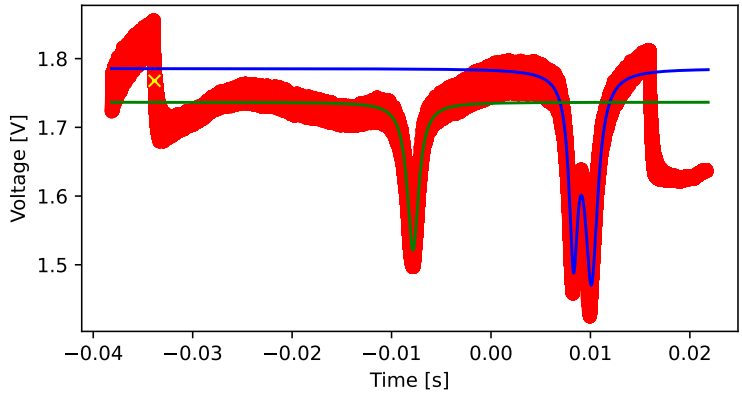

Figure 2.15: Photodector output measured on an oscilloscope, it shows a complete 50 ms frequency sweep 34 GHz to 36.4 GHz (effectively 68 GHz to 72.8 GHz) of the two second-order sidebands. In red, the measured data. In yellow, the point chosen to define the beginning of the frequency scan. In green, the fit of the resonance relative to the higher-order mode. In blue, the fit of the resonance relative to the lower order mode, note that it is a double Lorentzian.

We report the measurement of 25 line spacings in Fig. 2.16 and denote the central mode with index 0, since it is the one pumped with the usual laser (RIO Planex 1550nm). We chose to measure 25 FSR since it allowed us to reach the first-order modes in the primary comb regime, see Sec. 3.4. Moreover, we could have an idea of the dispersion of the FSR, namely its dependence on the frequency. Such dispersion could contrast with FWM generation conditions, therefore limiting performances or generating specific regimes. From the reported results, no dispersivity of the FSR is found. Measurement of $FSR_{3,2}$ (between modes 2 and 3) was problematic, as the resonance profile of mode 3 was not clearly distinguishable on the oscilloscope. Consequently, this measurement is not included in the reported results.

The uncertainty was evaluated taking into account: curve fitting uncertainty, RF generator resolution, and frequency scan starting point uncertainty. The last contribution was qualitatively evaluated to be $\delta t_{\text{start}} = 0.0002 + 0.0015 \cdot |t_{\text{start}}|$, the first part was chosen empirically, analyzing the oscilloscope data. While the second term takes into account that the frequency step used by the RF generator divided by the overall scan is around 0.15 %. The error bars of the $FSRs$ are mainly due to the starting point of the frequency scan. From Fig. 2.15, it is clear that the starting point is not easily defined, hence the use of a trigger is a better choice.

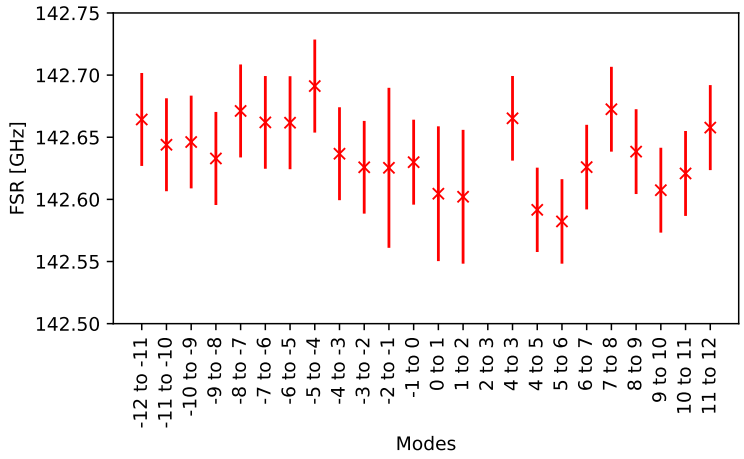

Figure 2.16: Measured $FSRs$ of the ring resonator, the measurements cover wavelengths from $\approx 1529\,\text{nm}$ to $\approx 1558\,\text{nm}$. Note that the line spacing between mode 2 and mode 3 is not reported, since it was not possible to precisely detect the resonance of mode 3 when pumping between resonances 2 and 3.

Dispersivity simulation

The FSR dispersion can also be simulated or calculated theoretically. The FSR in fact gives the separation between two adjacent modes, so in terms of wavevector k, $FSR_k = k(\omega_{\text{m}+1}) - k(\omega_{\text{m}})$ it is related to how k changes with modes (or equivalently ω) $FSR_k \sim dk/d\omega FSR_\omega$. Using the cavity resonance condition $k(\omega_m) = \pi m/L$ we get:

$$FSR_\omega = \frac{\pi}{L\dfrac{\partial k}{\partial \omega}} = \frac{\pi v_{\text{g}}}{L} \tag{2.8}$$

where $L = 2\pi R$ and we have introduced the group velocity $v_{\text{g}} = d\omega/dk = 1/\kappa_1$ describing the speed of the envelope of a wavepacket generated by superimposing different frequencies. In a non-dispersive material; therefore, where v_{g} is constant, it is possible to write $v_g = c/n_{\text{eff}}$ and retrieve Eq. (2.3). While a non-constant group velocity, namely a dispersive material, causes a non-zero:

$$k(\omega) = \frac{n_{\text{eff}}\omega}{c} \tag{2.9}$$

$$\frac{\partial k}{\partial \omega} = \kappa_1 \tag{2.10}$$

$$\frac{\partial \kappa_1}{\partial \omega} = \frac{\partial^2 k}{\partial \omega^2} = \kappa_2 = GVD \tag{2.11}$$

We have introduced κ_1, the group delay per unit length expressing the time it takes for the pulse envelope to travel a unit distance through the medium, and κ_2, the group velocity dispersion (GVD), measuring how the group delay κ_1 changes with frequency.

Now, we show the results of COMSOL simulations we used to extract κ_1, κ_2, and n_{eff}. In addition to verifying the FSR dispersion, knowing the values of these parameters is

essential for solving the equations governing the electric field in the ring (Lugiato–Lefever equations) and for comparing our experimental results with theoretical predictions. For this reason, we also used COMSOL to calculate the effective mode area A_{eff}, which quantifies the cross-sectional area occupied by the electric field inside the ring.

We performed the simulations for a Si_3N_4 microring built on a substrate of SiO_2. The radius is 185 μm, the waveguide width 1.7 μm, and the gap between the bus and ring waveguide of 0.5 μm.

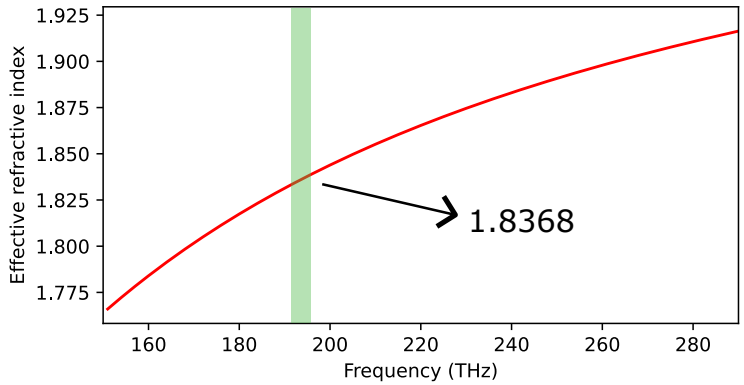

Figure 2.17: Simulation of the real part of the refractive index $Re(n) = n_{\text{eff}}$. In green, we shaded the frequency range of interest and reported an average value used for later calculations.

In Fig. 2.17, the simulated effective refractive index is shown. Note that in general, COMSOL simulates the complex refractive index $n = Re(n) + iIm(n)$, describing how light radiates in a given material with a certain geometry. It thus includes both diffraction/refraction (real part) and the absorption (imaginary part) effects the light experiences when traveling through a medium. Here we are mainly interested in the real part $Re(n) = n_{\text{eff}}$ and how that varies with frequency.

We note that $Re(n)$ can also be written as [52, 53]:

$$n_{\text{eff}} = \frac{k(\omega)}{k_0} \tag{2.12}$$

where $k(\omega)$ is the propagation constant in a given waveguide and takes into account the geometrical properties of the resonator, and $k_0 = 2\pi/\lambda_0$ is the vacuum wavenumber. From Eq. (2.12) it is immediate to note that in vacuum $k(\omega) = k_0$, thus obtaining $n_{eff} = 1$. Then, to show the waveguide effect on the propagation constant, we can Taylor expand $k(\omega)$ up to the second order:

$$k(\omega) = k_0 + \kappa_1(\omega - \omega_0) + \frac{\kappa_2}{2}(\omega - \omega_0)^2 \ + \ ... \tag{2.13}$$

where we retrieve the GVD κ_2 and ω_0 is the frequency around which the pulse spectrum is centered [53].

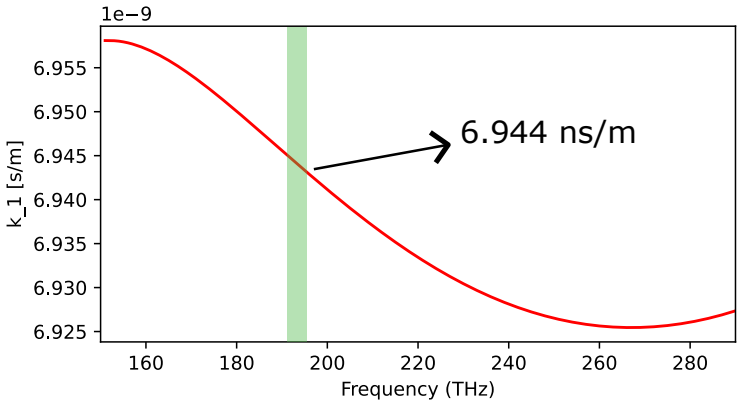

(a) Simulation of group delay κ_1.

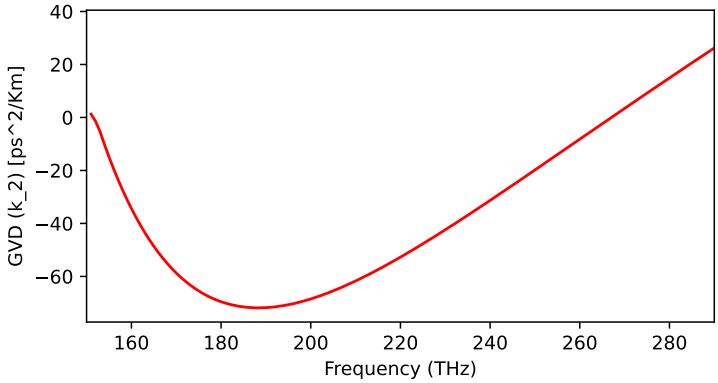

(b) Simulation of GVD, parameter κ_2. No specific value is reported here since no calculation was performed with the GVD parameter.

Figure 2.18: COMSOL simulations of the diffraction group delay (κ_1) and GVD (κ_2) of the propagation constant.

Next we show the simulations for κ_1 and κ_2, see Fig. 2.18. From Fig. 2.18b we observe that the ring is in an anomalous dispersion ($GVD < 0$) regime for the frequency region of interest.

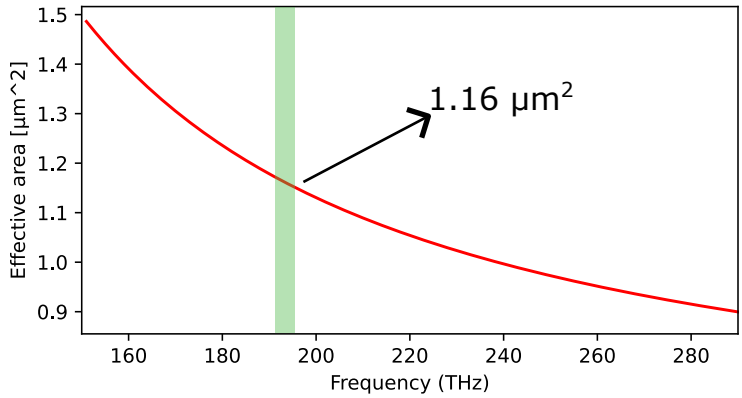

Figure 2.19: Simulation of A_{eff} as a function of pump frequency.

Lastly, the effective area (A_{eff}) of the light propagation in the waveguide was simulated. The result of the simulation is shown in Fig. 2.19. It is interesting to note how the confinement ability of the resonator changes with the frequency.

2.2 Detectors

The detection of single photons must be performed using appropriate devices able to emit an electric signal whenever a single photon impinges on them. Classical photodetectors cannot distinguish single particles of light. In fact, the magnitude of the output signal given a certain input is set by the responsivity (R) of the device; however, in C-band, it is typically about $\leq 1\,\text{A/W}$ [54–56]. Considering that the power generated by a single photon at $\lambda = 1550\,\text{nm}$ in a second is $P_{ph} = (\hbar c 2\pi/\lambda)/1 = 1.282 \times 10^{-19}\,\text{W}$, the emitted signal would be too low to be detected by classical electronics (e.g. oscilloscope or RF spectrum analyzer). As a consequence, devices such as superconducting nanowire single-photon detectors (SNSPDs) or single-photon avalanche detectors (SPADs) are mandatory when working with single states of light. The focus will be on the first kind of instrument, since it is the one we used.

2.2.1 Devices overview and theory

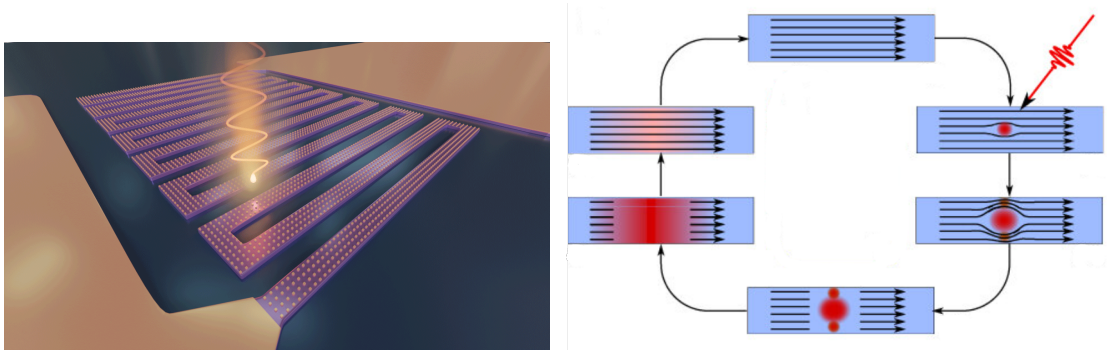

(a) Design schematic. Image taken from HRL Laboratories website.

(b) Working principle. Image taken from [57].

Figure 2.20: Schematic of SNSPD design and working principle.

SNSPDs are realized with a nanowire of a superconducting material built in a meandered shape, see Fig. 2.20a. During the operation, a current, just below the critical value for breaking the superconducting state of the material, flows through the nanowire. When a photon hits the conductor, due to energy transfer, superconductivity is lost, thus generating a resistive spot in the nanowire, see Fig. 2.20b. The loss of superconductivity forces the current to flow through narrower side regions around the resistive spot. The reduction of the section in which the electron flux must flow makes the current increase. Since it was near the threshold value during normal operation, now the critical current has surpassed it and superconductivity is broken along the nanowire transverse direction, creating a resistive barrier. Since both resistance and current are $\neq 0$, a voltage is generated. After a characteristic time, called dead time, the superconductivity is recovered, and the resistance returns to zero, and no voltage is present. The device is now ready for a new detection event. This process effectively generates a voltage pulse, which can be detected with classical electronics [57].

A noise source in detectors is the so-called "dark counts", spontaneous, random voltage pulses that occur without any incident photons, mimicking photon detection events. SNSPDs, however, have very low dark counts, below one hundred. Thanks to this feature, it is possible to work at very low count rates. In addition, SNSPDs are capable of reaching detection rates of the order of 10 MHz thanks to their low dead time $\sim$ 20 ps. Finally, such devices can work in a very broad wavelength range, and reach detection efficiencies (η) up to 90 % over the whole spectrum [58, 59]. η is defined as the number of detected photons divided by the number of photons effectively reaching the detector [27]. This is important when comparing to InGaAs SPAD, the cheapest option for single photon detection in the C-band, since this only has detection efficiencies of the order of 30 % [60]. The drawback of SNSPDs is that they need to work at cryogenic temperatures, around 2.5 K. It is also worth pointing out that they are not photon-number-resolving detectors. This means that they are not able to distinguish between one or multiple photons hitting the nanowire at the same time.

While up to 90 % detection efficiency is possible, this is not guaranteed. A photon

is most likely to be absorbed if it hits the nanowire with a polarization parallel to the meanders' direction [61], hence η is polarization dependent. For this reason, we present here, also, a characterization of the SNSPDs' detection efficiency as a function of the input light polarization.

2.2.2 Characterization

The definition of the characterization process for the detection efficiency of single-photon detectors is still under development in the metrology community. The main problem is that Single-Photon Detectors (SPDs) work in Geiger mode, which means they output a *click* or nothing. Instead, classical detectors measure a physical quantity that is related to the international standard of optical power. The number of *clicks* emitted by an SPD is not linked to any quantity, yet.

The detection efficiency of single-photon detectors depends on the operational wavelength, which must, therefore, be specified. Additionally, it depends on the photon rate due to the effect of the dead time. Increasing the photon rate, the efficiency decreases due to the dead time, which "covers" the next detection events. Therefore, the response function of an SPD is not linear, since doubling the input does not double the output due to the lowering of η. Given the dependence on the incoming photon rate, a metrologically interesting parameter is η_0, also called "zero-flux efficiency" [27]. It defines the efficiency at zero counts, so it is independent of the incoming photon rate and can be compared between different experimental conditions and setups.

To characterize the SNSPDs, we used the "substitution method" introduced by PTB (Physikalisch-Technische Bundesanstalt), and applied by INRiM and PTB in pilot studies [62, 63]. It consists of comparing the classical power measured by a detector traceable to the international standard and the number of clicks recorded by the SPD. The SPD detectors used at INRiM are Single Quantum Eos SNSPDs. The characterization setup we used is shown in Fig. 2.21.

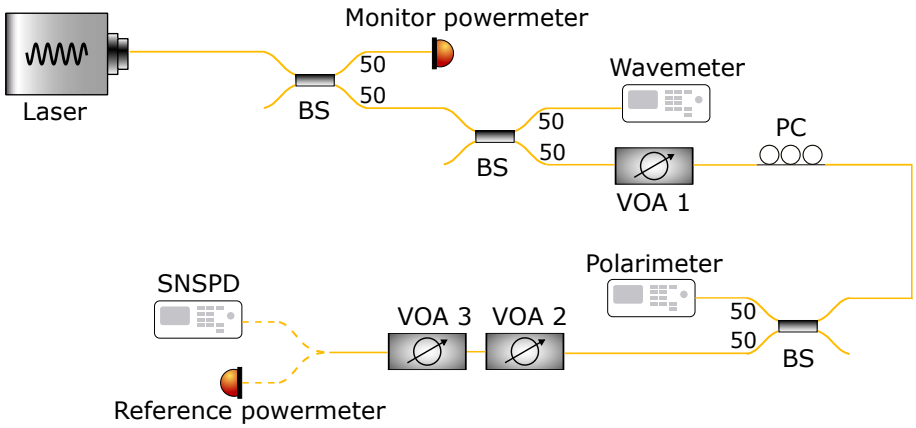

Figure 2.21: Facility for the characterization of the detection efficiency at different count rates and polarization of the SNSPD. After the last VOA, it is possible to connect either the SNSPD or the reference power meter. *VOA*: Variable Optical Attenuator.

Light exiting the laser is coupled into a 50/50 BS, which sends part of the power to the monitor power meter (81624B by Keysight), while the other output is sent to an additional balanced BS. One arm sends light to a wavemeter (621 Series by Bristol Instruments), while the rest of the radiation is sent through a Variable Optical Attenuator (VOA) (81577A by Keysight), which is used to control the photons' flux. Then, light is sent to a polarization controller and to a final balanced BS, which splits light between a polarimeter (N7781B by Keysight) and two VOAs (81577A by Keysight) connected in series. The latter devices are necessary to ensure that the radiation is at the single photon level, flux rate $\lesssim 10^6$, in order not to blind the SPDs. Lastly, the end of the optical path can be either connected to the SNSPDs or to the reference power meter (S154C by Thorlabs).

The idea is to compare the classical power reaching the end of the characterization facility and the recorded click counts. The classical power reaching the SNSPDs is evaluated thanks to the simultaneous operation of the monitor power meter with the SPD and a careful characterization of the total attenuation. The optical path that light undergoes in the facility is carefully evaluated with the means of the reference power meter, which is calibrated with respect to the SI (International System). Moreover, the monitor is not metrologically calibrated; therefore, the reference is also used to transmit the calibration to the monitor.

The detection efficiency, given the setup of Fig. 2.21, is obtained as:

$$\eta = \frac{hc}{\lambda t} \cdot \frac{N - N_{env}}{\tau \cdot cc \cdot P_{mon}} \tag{2.14}$$

where τ is the total transmissivity obtained as explained later, P_{mon} is the power read by the monitor. cc is the calibration parameter that links the power measured by the monitor and the reference power meter. It is calculated as $cc = P_0/P_{0,\text{mon}}$, where the subscript $_0$ means a 0 dB of nominal attenuation set on the VOAs and P is the power read by the reference.

The characterization procedure consists of three steps:

1. Characterization of the VOAs (Variable Optical Attenuators) and calibration of the reference power meter;

2. SNSPD characterization at different count rates and fixed polarization to estimate η_0;

3. SNSPD characterization at fixed count rate, but for different polarizations of the incoming light.

Characterization of the attenuations and calibration of the power meters

During the first step, the setup is terminated with the reference power meter. First, VOA 2 and VOA 3 are set to 0 dB, to calibrate VOA 1. The characterization of the other VOAs is performed analogously, with the VOAs not under characterization set to 0 dB. For example purposes, we assume VOA1 to be the VOA under characterization.

To characterize the attenuation experienced by light flowing through the facility at a given nominal attenuation set on the VOAs, we performed the following steps. The quantity of interest is the transmissivity τ, which is defined as:

$$\tau_{\mathrm{x}} = \frac{P_{\mathrm{x}}}{P_0} \tag{2.15}$$

where P_{x} is the power read by the reference power meter with x dB of nominal attenuation. Then, to obtain some statistics on the resulting τ, we performed 10 *sets* of 30 measurements or *runs*, therefore we have $\tau_{\mathrm{x}}^{(\mathrm{i,j})}$ with $1 \leq \mathrm{i} \leq 30$ and $1 \leq \mathrm{j} \leq 10$. In each *run*, given a fixed nominal source power, we measured the power reaching the reference and the monitor with all the possible nominal attenuations set on the VOAs. Then, we modified Eq. (2.15) to remove the contribution of the environmental counts:

$$\tau_{\mathrm{x}}^{(\mathrm{i,j})} = \frac{P_{\mathrm{x}}^{(\mathrm{i,j})} - P_{\mathrm{env}}^{(\mathrm{i,j})}}{P_0^{(\mathrm{i,j})} - P_{\mathrm{env}}^{(\mathrm{i,j})}} \tag{2.16}$$

where P_{env} is the power measured when the attenuators are switched off (maximum attenuation). The latter equation can be safely used only if the source radiation does not fluctuate in time. To remove this assumption and be as general as possible, we introduced the following modification:

$$\begin{aligned} P_{\mathrm{x}}^{(\mathrm{i,j})} &\to \rho_{\mathrm{x}}^{(\mathrm{i,j})} P_{\mathrm{x}}^{(\mathrm{i,j})} \\ P_0^{(\mathrm{i,j})} &\to \epsilon_{\mathrm{x}}^{(\mathrm{j})} \rho_0^{(\mathrm{i,j})} P_{\mathrm{x}}^{(\mathrm{i,j})} \end{aligned} \tag{2.17}$$

where:

$$\begin{aligned} \rho_{\mathrm{x}}^{(\mathrm{i,j})} &= \frac{\langle P_{\mathrm{x,mon}}^{(\mathrm{i,j})} \rangle_{\mathrm{i}}}{P_{\mathrm{x,mon}}^{(\mathrm{i,j})}} \\ \epsilon_{\mathrm{x}}^{(\mathrm{j})} &= \frac{\langle P_{\mathrm{x,mon}}^{(\mathrm{i,j})} \rangle_{\mathrm{i}}}{\langle P_{\mathrm{0,mon}}^{(\mathrm{i,j})} \rangle_{\mathrm{i}}} \end{aligned} \tag{2.18}$$

where $P_{\mathrm{x,mon}}^{(\mathrm{i,j})}$ is the power read by the monitor power meter with x dB of nominal attenuation at the i-th *run* and j-th *set*. $\langle \cdot \rangle_{\mathrm{i}}$ means the average over all 30 *runs*. With Eq. (2.17), we can consider the source fluctuations, because ρ_{x} considers the punctual deviation of the source, it is the comparison of the single outcome with respect to the average of a *set*. Instead, ϵ_{x} takes into account slow drifts of the source; in fact, it contains the ratio between the average values of different *sets*. What we obtain in the end is the following:

$$\tau_{\mathrm{x}}^{(\mathrm{i,j})} = \frac{\rho_{\mathrm{x}}^{(\mathrm{i,j})} P_{\mathrm{x}}^{(\mathrm{i,j})} - P_{\mathrm{env}}^{(\mathrm{i,j})}}{\rho_0^{(\mathrm{i,j})} P_0^{(\mathrm{i,j})} - P_{\mathrm{env}}^{(\mathrm{i,j})}} \frac{1}{\epsilon_{\mathbf{x}}^{(\mathbf{j})}} \tag{2.19}$$

where we used the fact that the environmental counts are independent of the source fluctuations. And since the contribution of P_{env} is small and $\epsilon_{\mathrm{x}} \approx 1$ we can write $P_{\mathrm{env}}/\epsilon_{\mathrm{x}} \approx P_{\mathrm{env}}$.

Now, we evaluated $\tau_{\mathrm{x}}^{(\mathrm{j})} = \langle \tau_{\mathrm{x}}^{(\mathrm{i,j})} \rangle_{\mathrm{i}}$ for every *set* and the associated statistical uncertainty $\delta\tau_{\mathrm{x}}^{(\mathrm{j})}$ is calculated as the standard deviation of the mean. It turns out that the

results of different *sets* are not compatible with each other, i.e., the uncertainty ranges do not overlap between all of them. This result is due to the non-repeatability of the experiment. For example, the VOAs are mechanical devices, and every time the nominal attenuation is changed and then set back to the initial value, it is not assured that the system will be identical to the initial condition. To evaluate a final single result of τ, we must take into account such an effect. The GUM [64], which is the standard international metrological guide describing how to report the uncertainty of measurements, states that non-repeatability can be taken into account by considering the results as outcomes of a rectangular random variable. Therefore, we inserted the additional contribution, including the standard deviation of a rectangular probability distribution:

$$\delta\tau_{\mathrm{x}} = \sqrt{\sum_{j=1}^{10} \frac{(\delta\tau_{\mathrm{x}}^{(\mathrm{j})})^2}{10} + \frac{(max\{\tau_{\mathrm{x}}^{(\mathrm{j})}\} - min\{\tau_{\mathrm{x}}^{(\mathrm{j})}\})^2}{3}} \tag{2.20}$$

where 10 is the number of *sets*. Combining Eq. (2.19) and Eq. (2.20), the calibration of the attenuation light undergoes when flowing through the facility for a given x dB of nominal attenuation is found.

Evaluation of the detection efficiency at different count rates

During the second step, the reference power meter is substituted with the *device under test* (DUT), to obtain the η_0, we model η as [61, 63, 65]:

$$\eta(\lambda, N) = \eta_0(1 - D\frac{N - N_{env}}{t}) \tag{2.21}$$

where λ is the impinging photon wavelength, N is the count rate, N_{env} is the count rate measured in the absence of light (the VOAs are off). Therefore, it takes into account the dark counts and environmental photons (e.g., from room light). D is the dead time, and t is the acquisition time. The latter equation allows us, using a linear regression of the measured η as a function of N, to obtain the parameters η_0 and D.

To modify N, VOA1 was swept from 0 dB to 20 dB, instead VOA2 and VOA3 were both set to 40 dB to reach the single photon regime.

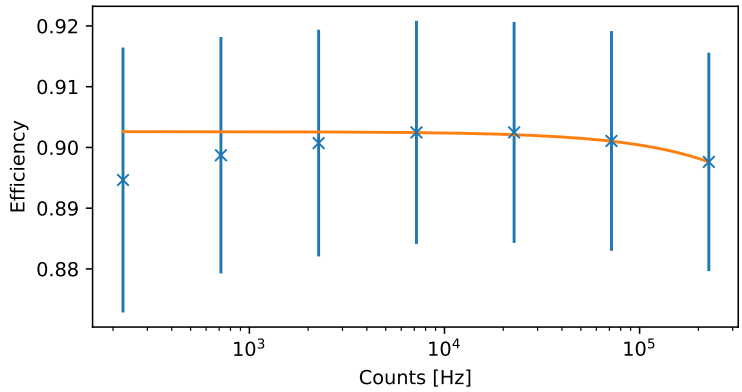

Figure 2.22: Plot of the measured efficiency as a function of the photon flux rate reaching the detector. In orange, the fit curve calculated using Eq. (2.21), note, the x-axis is in logarithmic scale.

The data plotted in Fig. 2.22 show the detection efficiency as a function of the photon count rate; Eq. (2.21) was used as the fitting curve. The parameters extracted from the linear regression are $\eta_0 = 0.903(19)$ and $D/t = 2.2(4) \times 10^{-8}$. The zero-flux efficiency η_0 is around 90 %, which is compatible with nominal specifications. Having used an acquisition window of $t = 1\,\text{s}$, we can estimate the dead time of the detectors to be $D = 22(4)\,\text{ns}$. This result is comparable with the maximum photon detection rate achievable by SNSPDs and the datasheet specifications.

Evaluation of the detection efficiency polarization dependence

Lastly, we reach the third step, where the DUT detection efficiency was studied for different light polarizations, given a fixed count rate. Here, we assume that the polarization-dependent detection efficiency could be described as follows:

$$\eta = \eta_{\max}[1 - a + a \cdot cos^2(\frac{\theta}{2})] \tag{2.22}$$

where $\eta_{\max}$ is the detection efficiency with polarization parallel to the meanders (maximum efficiency), $\theta/2$ is the angle between the polarization of the impinging beam and the nanowire direction (see Fig. 2.23b), and a defines the minimum efficiency with $\eta_{\min} = \eta_{\max}(1 - a)$. This assumption is based on the idea that the meander's direction behaves in the same way as the polarizer optical axis. For this reason, we propose a model with just one variable θ and two parameters $\eta_{\max}$ and a. We call the polarization parallel to the nanowire "horizontal" and the perpendicular one "vertical". Keeping this in mind, we construct the Poincaré sphere, with θ as the polar angle. The Poincaré sphere is a graphical representation that maps all possible polarization states of light onto points on or inside a unit radius sphere.

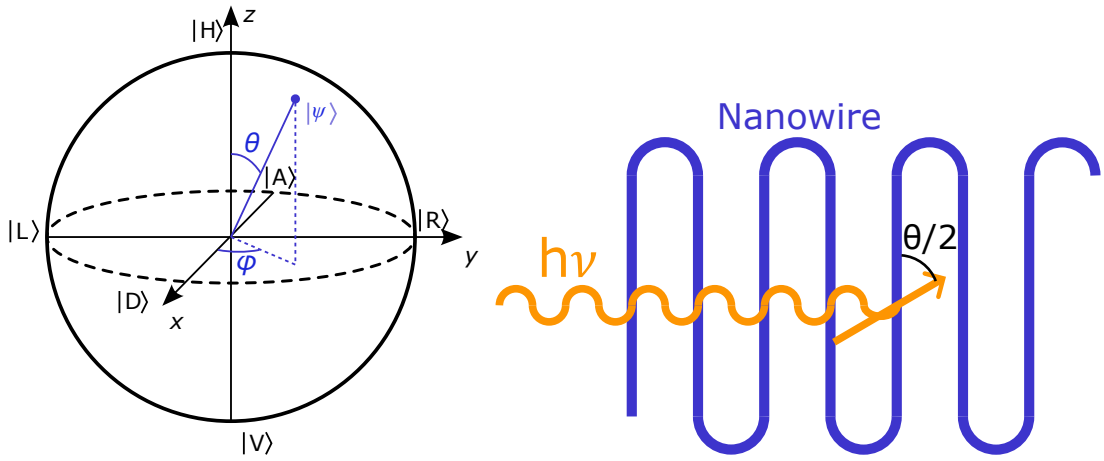

(a) Poincaré sphere.

(b) Schematic of the polarization dependence during a detection event. The orange arrow represents the polarization direction of the photon.

Figure 2.23

Each polarization vector is characterized by the coordinates (r, θ, φ). The radius (r) measures the "purity" of the polarization state: pure states lie on the surface $(r = 1)$, while partially polarized (statistical mixtures) occupy the interior $(r < 1)$. The polar angle quantifies the ellipticity, and the azimuthal angle φ sets the orientation of the polarization ellipse. The basis vectors of the two-dimensional Hilbert space are positioned at the upper and lower poles of the sphere. In our case, the basis vectors are the horizontal $(|H\rangle)$ and vertical $(|V\rangle)$ polarizations. Using this, we can also define other useful states (see Fig. 2.23a):

- $|D\rangle = \dfrac{|H\rangle + |V\rangle}{\sqrt{2}}$: diagonal polarization;
- $|A\rangle = \dfrac{|H\rangle - |V\rangle}{\sqrt{2}}$: anti-diagonal polarization;
- $|R\rangle = \dfrac{|H\rangle + i|V\rangle}{\sqrt{2}}$: right-circular polarization;
- $|L\rangle = \dfrac{|H\rangle - i|V\rangle}{\sqrt{2}}$: left-circular polarization.

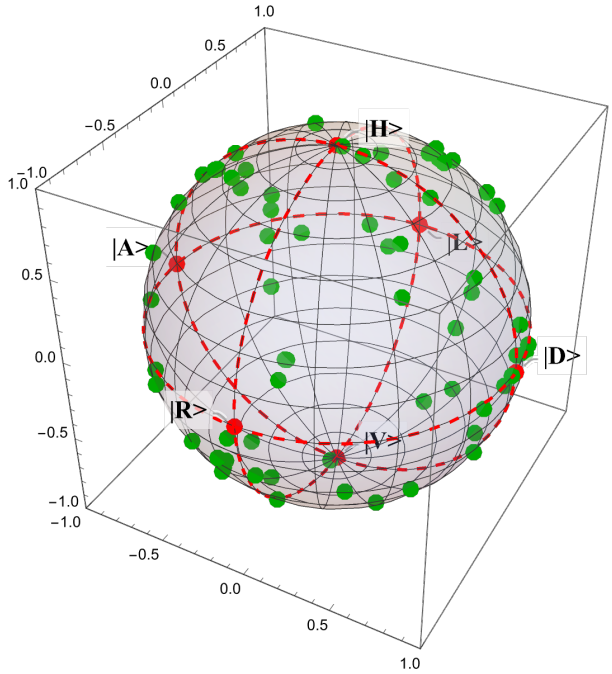

Figure 2.24: Poincaré sphere of the polarimeter, the green dots represent the points where a measurement was performed. The red dashed lines represent the equator and the two meridians parallel to the x and y axes.

As shown in Fig. 2.21, we measure the polarization using a polarimeter. However, the optical fiber that separates the SNSPD and the polarimeter generates a linear rotation of the polarization on the Poincaré sphere, hence the polarimeter measurement does not show the effective polarization experienced by the SNSPD. Therefore, we need to rotate the polarimeter sphere onto the detector reference frame. To do so, we perform measurements of the detection efficiency as a function of the polarization read on the polarimeter, trying to cover the whole Poincaré sphere (polarimeter reference frame), see Fig. 2.24. We note that each point has $r = 1$, indicating we are working with purely polarized light, so from now on we assume $r = 1$. Working with only pure states does not reduce the generality of the work; mixed states are generated from a linear superposition of pure states. Therefore, the behavior of a mixed state can be retrieved by summing together the weighted contributions of the pure states.

From the measurements, the point of maximum efficiency is found $\eta_{max}(\theta'_{max}, \varphi'_{max})$ (with $'$ we indicate the polarimeter reference). An appropriate rotation is then performed to set such a point to $(\theta_{max} = 0^{(dut)}, \varphi_{max} = 0^{(dut)})$. Such rotation was performed using Cartesian coordinates (x, y, z), with z being the vertical axis. The three coordinates that define a vector in the Poincarè sphere in the SNSPD reference frame are built starting from $(\theta'_{max}, \varphi'_{max})$. Note that the azimuthal plane has no role in Eq. (2.22); therefore, it is constructed arbitrarily. For example, the point (0,0,1) of the SNSPD is built to coincide with $(\theta'_{max}, \varphi'_{max})$. The linear rotation to go from the polarimeter frame (x', y', z') to the

DUT frame (x, y, z) is:

$$R = \begin{pmatrix} x_{x'} & y_{x'} & z_{x'} \\ x_{y'} & y_{y'} & z_{y'} \\ x_{z'} & y_{z'} & z_{z'} \end{pmatrix} \tag{2.23}$$

where $x_{x'}$ indicates the coordinate on the x'-axis of the point defining the x-axis on the SNSPD sphere. Therefore, to map
$(\theta'_{\max}, \varphi'_{\max}) = (sin(\theta'_{\max})cos(\varphi'_{\max}), sin(\theta'_{\max})sin(\varphi'_{\max}), cos(\theta'_{\max}))$ to (0,0,1), the element $z_{z'}$ needs to be $cos(\theta'_{\max})$. Then every point can be mapped onto the DUT reference system using:

$$\begin{pmatrix} x \\ y \\ z \end{pmatrix} = R^{-1} \begin{pmatrix} x' \\ y' \\ z' \end{pmatrix} \tag{2.24}$$

Now, it is possible to use Eq. (2.22) to fit the rotated data.

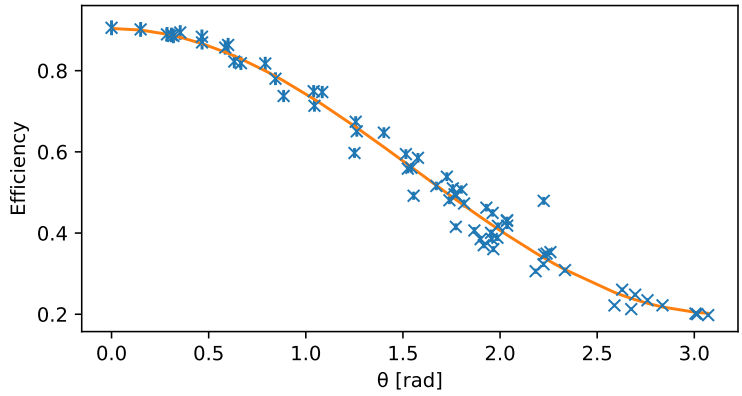

Figure 2.25: Detection efficiency as a function of the angle θ. In orange, the fit curve obtained using Eq. (2.22) with parameters: $a = 0.777(9)$ and $\eta_{\max} = 0.904(8)$.

In Fig. 2.25, the behavior of the detection efficiency as a function of the polarization angle θ is shown. The good agreement between data and fitting curve confirms the previous hypothesis that Eq. (2.22) describes the polarization dependence of the detection efficiency. The fitted parameters are $\eta_{max} = 0.904(8)$, which is compatible with η_0 previously calculated, and $a = 0.777(9)$. The latter result can be used to calculate the minimum detection efficiency $\eta_{min} = \eta_{max}(1 - a) = 0.202(8)$. These results confirm that, to have the highest efficiency possible, it is important to align the incoming light polarization with the detector meanders direction.

To avoid the repetition of such an alignment procedure, there are novel approaches to try to reduce the polarization dependency of the SNSPDs detection efficiency [66–68]. One of the options is to build the nanowires with a geometry as direction-independent as possible, for example, in a circular or fractal-like shape.

Finally, in order to obtain a result suitable for experimental practice, the detection efficiency was mapped onto the Poincaré sphere of the polarimeter. In this way, without changing the setup and moving the fibers, given a measured polarization, one immediately

knows the detection efficiency of the SPDs. To do so, a minimization of the detection efficiency on the sphere was performed using the software Wolfram Mathematica. Essentially, it is a non-linear fit of the detection efficiency on all the measured data points, without forcing the rotation of the sphere. To do so, first we had to demonstrate the dependence of the detection efficiency on only one variable θ as done before. Second, it was useful to force the parameters to be swept in a bound range, $0 \leq a \leq 1$ and $\eta_{\max}^{(\exp)} \leq \eta_{\max} < 1$, where $\eta_{\max}^{(\exp)}$ is the maximum measured detection efficiency.

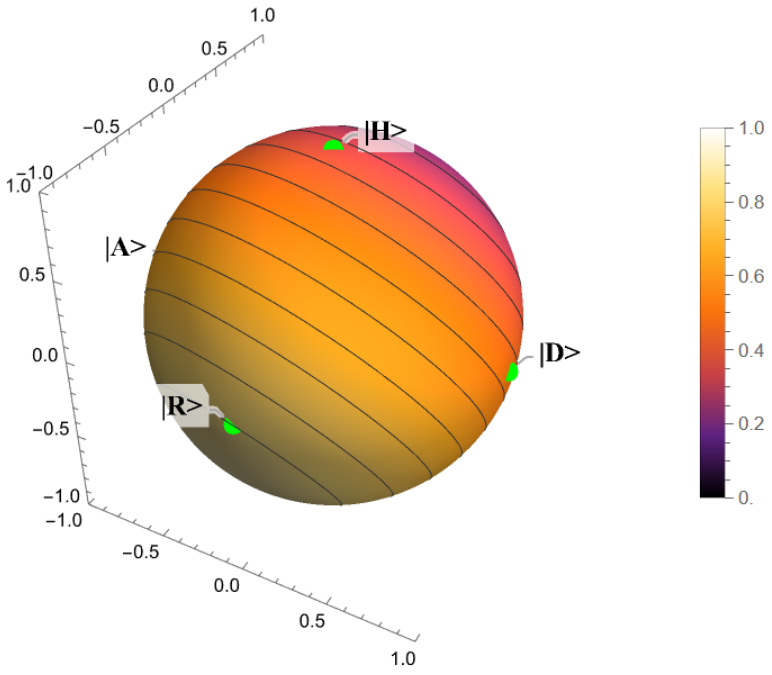

Figure 2.26: Detection efficiency mapped onto the polarimeter reference system.

In Fig. 2.26, the result of the minimization is shown. The detection efficiency is maximum for $\theta \neq 0$, as expected. The latter result is more accurate than using data from Fig. 2.25 and re-mapping it on the polarimeter sphere. Here, the point of maximum efficiency was obtained through the minimization and was not forced among the measured data points.

Chapter 3

Entangled states generation process: Four-Wave Mixing

3.1 Introduction

In this chapter, we describe the process capable of generating entangled states of light in a microring resonator. After a brief review of optical nonlinear processes, we then focus on four-wave mixing (FWM) in a microresonator. In particular, we discuss the different operational regimes of the microring, such as spontaneous and stimulated FMW. In addition, we introduce the concept of optical frequency combs and discuss the different ways they can be generated in a microring through FWM. This discussion is complemented by a qualitative comparison between the theoretical predictions obtained through numerical simulations and the experimental observations. To conclude, we will describe how the generation in the microring process was characterized and present the results.

3.2 Introduction to optical non-linearities

When a material is subject to an external electromagnetic field E, its charges redistribute in a way that creates electric dipoles. The macroscopic response is described by the total polarization P_{T}, defined as the electric dipole moment per unit volume, which depends on the material's properties. In linear regimes, and using a scalar notation for ease of understanding, P_{T} varies linearly with the electric field as:

$$P_{\mathrm{T}}(t,\omega) = \epsilon_0 \chi^{(1)}(\omega) E(t,\omega) \tag{3.1}$$

where ϵ_0 is the permittivity of vacuum and $\chi^{(1)}$ is the linear susceptibility of the material.

Initially, only linear material responses were observed, but after the discovery of the first laser [69]. It was possible to probe the materials with more intense optical fields due to highly focused radiation. These new experiments revealed that the dipole moment inside a material could exhibit a non-linear dependence on the electric field, involving

higher-order terms beyond the linear response [17]:

$$\begin{aligned} P_{\mathrm{T}}(t,\omega) =& \epsilon_0[\chi^{(1)}(\omega)E(t,\omega) + \chi^{(2)}(\omega)E^2(t,\omega) + \chi^{(3)}(\omega)E^3(t,\omega) \ + \ ...] = \\ & P_{\mathrm{L}}(t,\omega) + P_{\mathrm{NL}}(t,\omega) \end{aligned} \tag{3.2}$$

where $\chi^{(2)}$ and $\chi^{(3)}$ are called, respectively, the second and third-order nonlinear optical susceptibilities. It is common to separate the linear part of the polarization, $P_L(t,\omega) = \epsilon_0\chi^{(1)}(\omega)E(t,\omega)$, from the remaining terms included in $P_{NL}(t,\omega)$.

The second-order nonlinear susceptibility is responsible for processes like second-harmonic generation [70], in which two photons of frequency ω are effectively converted into a single photon of frequency 2ω. This effect has been broadly used to generate laser light at frequencies that would otherwise be inaccessible. Another important effect induced by a non-vanishing $\chi^{(2)}$ is Spontaneous Parametric Down-Conversion (SPDC). In this process, one photon at frequency ω_1 is "down-converted" into two lower-energy photons at ω_2 and ω_3. Energy conservation imposes $\omega_1 = \omega_2 + \omega_3$, while momentum conservation is enforced by the condition of phase matching [71]. Among the applications, SPDC is employed for the creation of entangled and single-photon sources [72–74].

The third-order nonlinear susceptibility is, instead, responsible for effects such as the Kerr effect [75], which is the dependence of the refractive index of the material on the intensity of the applied optical radiation. The Kerr effect can be described mathematically by expressing the refractive index as a function of the optical power:

$$n = n_0 + n_2\frac{P}{A_{\mathrm{eff}}} \tag{3.3}$$

where P is the optical power flowing through the material and n_2 is the Kerr coefficient. Materials with a non-vanishing $\chi^{(3)}$ are also called Kerr materials.

Typical values of $\chi^{(2)}$ range from 10^{-24} cm/V to 10^{-21} cm/V, while for $\chi^{(3)}$ are usually of the order of $10^{-34}\,\mathrm{cm}^2/\mathrm{V}^2$ to $10^{-29}\,\mathrm{cm}^2/\mathrm{V}^2$ [16, 17]. Due to these low values, it is easy to understand how such effects can be experienced only with high optical intensities. Resonant geometries, which enhance the local field (see Eq. (2.1)), are a novel, but effective approach to increase the efficiencies of non-linear processes [72, 76].

We now turn to the third-order nonlinear process of primary interest in this work: Four-Wave Mixing (FWM).

3.3 Stimulated and spontaneous Four-Wave Mixing

Four-wave mixing is an effect in which four waves inside a Kerr material interact under given conditions. In this section, we give a formal description of stimulated (classical process) and spontaneous (quantum process) four-wave mixing.

Stimulated FWM is the generation of a wave at ω_4 by the coherent interaction of three waves at ω_1, ω_2, and ω_3. Assuming a medium with only a third-order non-linearity, we can rewrite Eq. (3.2) as:

$$P_{NL}(t,\omega) = \epsilon_0\chi^{(3)}E^3(t,\omega) \tag{3.4}$$

Now, we can write the electric field as a superposition of three plane waves:

$$E(t,\omega_1,\omega_2,\omega_3) = \sum_{q=\pm1,\pm2,\pm,3} \frac{1}{2} E(\omega_{\mathrm{q}}) e^{j\omega_{\mathrm{q}} t} \tag{3.5}$$

where $\omega_{-q} = -\omega_q$ and $E(-\omega_q) = E^*(\omega_q)$. Substituting equation Eq. (3.5) in Eq. (3.4), we get a sum of harmonic components with frequencies $3\omega_1$, $2\omega_1+\omega_2$, $\omega_1+\omega_2+\omega_3$, and so on. We are interested only in the component $P_{NL}(t,\omega_1+\omega_2-\omega_3)$, which is the one responsible for four-wave mixing [16]:

$$P_{NL}(t,\omega_1+\omega_2-\omega_3) \propto \epsilon_0 \chi^{(3)} E(\omega_1) E(\omega_2) E^*(\omega_3) e^{j(\omega_1+\omega_2-\omega_3)t} \tag{3.6}$$

Equation Eq. (3.6) indicates that a fourth wave is generated in the medium at frequency:

$$\omega_4 = \omega_1 + \omega_2 - \omega_3 \tag{3.7}$$

Moreover, the three initial amplitudes $E(\omega_{1,2,3})$ can be written as:

$$E(\omega_{1,2,3}) = |E(\omega_{1,2,3})| e^{jk_{1,2,3}r} \tag{3.8}$$

where r is the space coordinate and $k_{1,2,3}$ is the wavevector. We can expand the non-linear polarization as:

$$P_{NL}(t,\omega_1+\omega_2-\omega_3) \propto \epsilon_0 \chi^{(3)} |E(\omega_1)||E(\omega_2)||E^*(\omega_3)| e^{j(k_1+k_2-k_3)r} e^{j(\omega_1+\omega_2-\omega_3)t} \tag{3.9}$$

From the latter, we get that the generated wave has a wavevector k_4 which is [16]:

$$k_4 = k_1 + k_2 - k_3 \tag{3.10}$$

Note that in general, the wavevectors are three-dimensional vectors. Equations Eq. (3.7) and (3.10) are, respectively, the frequency-matching and phase-matching conditions, and they must be respected for FWM to arise. The first condition describes the energy conservation of the process, while the second one, the momentum conservation, we present a schematic representation in Fig. 3.1.

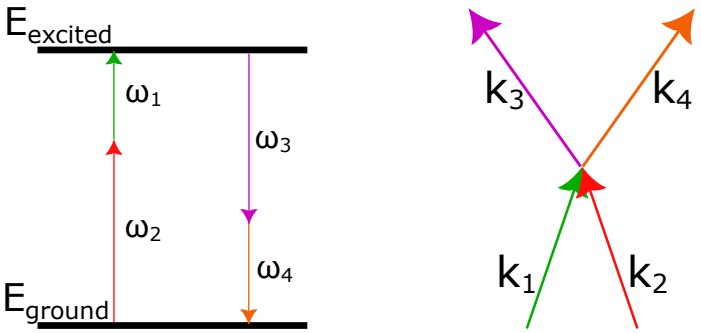

(a) Energy-matching condition.

(b) Phase-matching condition.

Figure 3.1: Schematic of the FWM constraint conditions.

When $\omega_1 \neq \omega_2$, the effect is called non-degenerate four-wave mixing, while when $\omega_1 = \omega_2$, the process is degenerate. The second case is simpler to achieve, as it only requires strongly pumping the non-linear medium with a single laser beam of frequency ω_1, and injecting a seed component at frequency ω_3, triggering the generation of light at frequency $\omega_4 = 2\omega_1 - \omega_3$. A useful notation is to call $\omega_1 = \omega_\mathrm{p}$, $\omega_3 = \omega_\mathrm{s}$ the signal, and $\omega_4 = \omega_\mathrm{i}$ the idler photon as in Fig. 3.2a.

Stimulated four-wave mixing is, therefore, a classical process where three waves are injected in a third-order non-linear medium, which responds by generating a new component if frequency-matching and phase-matching conditions are met.

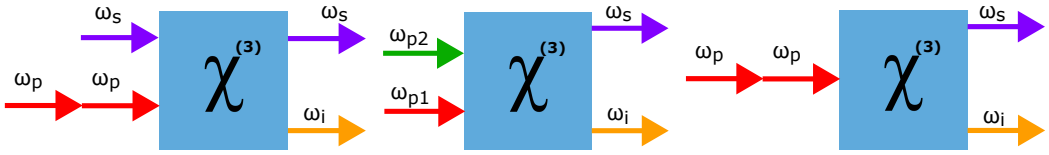

(a) Degenerate stimulated four-wave mixing.

(b) Non-degenerate spontaneous four-wave mixing.

(c) Degenerate spontaneous four-wave mixing.

Figure 3.2: Different types of four-wave mixing. In red and green, the pump wave with frequency $\omega_{\mathrm{p1,p2}}$. In purple and orange, respectively, the signal and idler waves with frequencies ω_s and ω_i.

In spontaneous FWM (SFWM), signal and idler photons are generated without injecting a seed at either of the two output frequencies, see Fig. 3.2c. The emission is stimulated by vacuum fluctuations, a purely quantum effect that stimulates the process, analogous to spontaneous emission [77]. Phase and frequency-matching conditions that need to be met are the same as in the stimulated case.

Therefore, stimulated and spontaneous FWM both need two pump photons, namely ω_1 and ω_2 of Fig. 3.1a. But in the classical case, one must insert an additional wave ω_3 to stimulate the emission of ω_4 also.

3.3.1 Third-order non-linearities in microresonators: Optical Parametric Oscillators

Exploiting the $\chi^{(3)}$ non-linearity of Si_3N_4, we are effectively building an optical-parametric amplifier (OPA). It is called an amplifier since in the presence of a suitably intense injected beam, it generates waves at frequencies that were not present or associated with less intensities before injection. In addition, it is parametric, since the initial and final energy levels of the process are the same: the process only redistributes energy among the interacting optical fields, without permanently exciting the material, see Fig. 3.1a. In particular, no heating is generated, assuming a lossless material. By inserting an OPA medium inside a resonating structure, it is possible to build an optical-parametric oscillator (OPO). An OPO is a light source, analogous to a laser, but instead of stimulated emission, it exploits parametric amplification to generate the output radiation [78]. An OPO, to reach a steady emission over time, needs to be pumped with a certain threshold power $P_{\text{th}}^{(\text{OPO})}$. Such power needs to be able to feed the amplification process and sustain losses inside the resonator [79], again analogously to a laser. When the threshold power is reached, the pumping field is able to generate enough signal and idler photons to induce self-sustained oscillations in the resonator. When our microring OPO is above threshold, stimulated four-wave mixing is the dominating process, since the signal and idler continuously oscillating inside the resonator stimulate further emission. While below threshold, it dominates SFWM [21], and only a weak emission of photons is experienced.

This thesis concentrates on the below-threshold operation of the OPO, where SFWM leads to the generation of non-classical photon pairs. Furthermore, we also study the threshold region, where the transition from spontaneous to stimulated FWM leads to the OPO effect and begins to emit a classical coherent field above threshold.

3.3.2 Quantum description of SFWM in OPOs

As a starting point, we want to describe the photon emission in each signal and idler mode in terms of a generation rate. To do so, we must write the state generated by SWFM inside a microring pumped with a pulsed laser. Note that in our experiment, we worked with a CW laser; however, the result is analogous (limit of infinitely long pulse). Under the assumption of equally spaced cavity modes, weak and undepleted pump, the generated state is [80]:

$$|\psi\rangle = e^{\beta \int d\omega_3 d\omega_4 \phi(\omega_3,\omega_4)\hat{a}^+_{\omega_3}\hat{a}^+_{\omega_4} - H.c}|0\rangle \tag{3.11}$$

where ω_3 and ω_4 are the variables of the possible frequencies for the signal and idler photons, $\hat{a}^+$ is the creation operator, $|\beta|^2$ gives the average number of photons generated per pump pulse, and *H.c.* means the hermitian conjugate. $\phi(\omega_3, \omega_4)$ is the biphoton wavefunction (describes photon in signal and idler mode) or also called the joint spectral amplitude (JSA), and it is analytically defined as [80]:

$$\phi(\omega_3, \omega_4) = \frac{i|\alpha|^2\sqrt{2}}{4\pi\beta}\frac{\sqrt{\omega_3\omega_4}}{\omega_{\text{p}}}\gamma_{\text{NL}}\int d\omega_1 \phi_{\text{p}}(\omega_1)\phi_{\text{p}}(\omega_2)\sqrt{\omega_1\omega_2}I(\omega_1,\omega_2,\omega_3,\omega_4) \tag{3.12}$$

respecting $\omega_4 = \omega_1 + \omega_2 - \omega_3$, and $\omega_{1,2}$ are the integration variables relative to the pump photons. ω_p is the central frequency of the pump pulse, $|\alpha|^2$ is the average number of pump photons, $\phi_\mathrm{p}(\omega_{1,2})$ describes the frequency distribution of the pump pulse centered at ω_p ($\sim$ constant for a continuous pump). The parameter

$$\gamma_\mathrm{NL} = \frac{n_2\sqrt{\omega_\mathrm{s}\omega_\mathrm{i}}}{cA_\mathrm{eff}} \tag{3.13}$$

is the nonlinear coefficient of the Kerr medium [81], while n_2 is the Kerr coefficient (see Eq. (3.3)) and $\omega_{\mathrm{s,i}}$ are the signal and idler frequencies where the phase-matching, frequency-matching, and geometrical conditions are met.

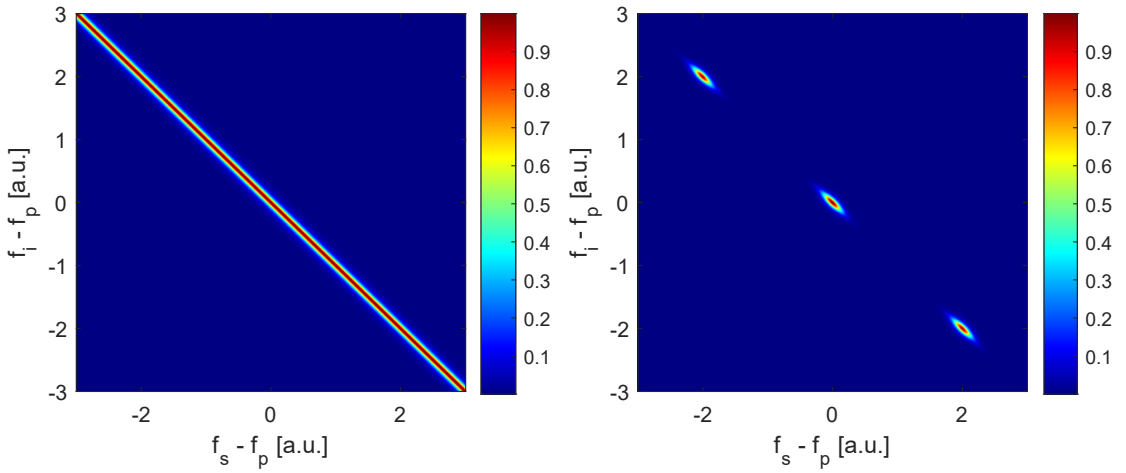

(a) Broad spectrum of the parametric phenomenon modeled by the convolution of a Lorentzian distribution and the energy-matching condition function (diagonal line).

(b) Broad spectrum filtered by a resonator.

Figure 3.3: Qualitative example of a JSI generated by SFWM pumping the non-linear medium at $\lambda_\mathrm{p} = 1550\,\mathrm{nm}$. Note that the resonator's parameters in Fig. 3.3b are chosen purely for illustrative purposes.

Finally, $I(\omega_1, \omega_2, \omega_3, \omega_4)$ incorporates the matching conditions for the system. For a resonator-enhanced FWM, this function can be written as:

$$I(\omega_1, \omega_2, \omega_3, \omega_4) = f_\mathrm{s}(\omega_3) f_\mathrm{i}(\omega_4) f_\mathrm{p}(\omega_1) f_\mathrm{p}(\omega_2) L \tag{3.14}$$

where L is the resonator length, and $f_{\mathrm{p,s,i}}(\omega)$ describes the pump, signal, and idler matching conditions in the resonator. The resonator imposes a Lorentzian frequency response on each field, such that the functions can be written as:

$$f_{\mathrm{p,s,i}}(\omega) = \frac{1}{2}\sqrt{\frac{2}{1-\sigma_{\mathrm{p,s,i}}}}\frac{\Delta\nu_{\mathrm{p,s,i}}}{(\omega-\omega_{\mathrm{p,s,i}}) + i\Delta\nu_{\mathrm{p,s,i}}/2} \tag{3.15}$$

where $\sigma_{\mathrm{p,s,i}}$ is the coupling strength between the straight and ring waveguide for the pump, signal, and idler frequency (note that for critical coupling $\sigma_{\mathrm{p,s,i}} = \Delta\nu$, cavity linewidth).

The quantity $|\phi(\omega_3, \omega_4)|^2$ is called joint spectral intensity (JSI), see an example in Fig. 3.3. It is essentially a probability density distribution describing where the signal and idler photons can be generated, given phase-matching, frequency-matching, and geometrical boundary conditions.

With the equations described above, it is possible to calculate the FWM-generated photon power, e.g., in the idler channel, both in the stimulated and spontaneous cases. For a CW pump [82, 83]:

$$P_{\mathrm{i,ST}} = (\gamma_{\mathrm{NL}} 2\pi R)^2 (\frac{Q v_g}{\omega_{\mathrm{p}} \pi R})^4 P_{\mathrm{s}} P_{\mathrm{p}}^2 \tag{3.16}$$

and

$$P_{\mathrm{i,SP}} = (\gamma_{\mathrm{NL}} 2\pi R)^2 (\frac{Q v_g}{\omega_{\mathrm{p}} \pi R})^3 \frac{\hbar \omega_{\mathrm{p}} v_g}{4\pi R} P_{\mathrm{p}}^2 \tag{3.17}$$

where R specifies the ring radius, v_g is the group velocity, i.e., the inverse of k_1, and $P_{\mathrm{s(p)}}$ is the intra-resonator power at the frequency of the signal (pump) mode. The formulae are also valid for the signal channel. It is possible to calculate the ratio:

$$\frac{P_{\mathrm{i,SP}}}{P_{\mathrm{i,ST}}} = \frac{1}{4Q} \frac{\hbar \omega_{\mathrm{p}}^2}{P_{\mathrm{s}}} \tag{3.18}$$

It is interesting to note how the ratio between spontaneous and stimulated emission strictly depends on the intrinsic quality factor of the resonator and the coupled seed power. This means that the quality factor of the cavity is fundamental when designing a resonator.

SFWM and energy-time entanglement

Eq. (3.11), not showing the frequency dependence, describes a quantum state of the type, whenever the integral is different from 0:

$$|\psi\rangle = |1_{\mathrm{i}} 1_{\mathrm{s}}\rangle \tag{3.19}$$

where $|1_{\mathrm{i,s}}\rangle$ indicates the state, respectively, for the idler and signal photon. Such a state can be used to generate energy-time entanglement, better described in Sec. 4.4.

Energy-time entanglement describes a quantum state that displays non-local quantum correlations over the frequency and time degrees of freedom. We can clearly display the frequency correlations by making an assumption: $\phi(\omega_3, \omega_4)$ is non-zero only at resonator resonances. Therefore, we can simply write the state as, recovering the frequency dependence, [84]:

$$|\psi\rangle = \sum_{\mathrm{j}=1}^{\mathrm{N}} \xi_{\mathrm{j},-\mathrm{j}} |1_{\mathrm{i,j}} 1_{\mathrm{s},-\mathrm{j}}\rangle \tag{3.20}$$

where j is the resonance index, $2N$ is the total number of considered resonances, and $\xi_{\mathrm{j},-\mathrm{j}}$ are the occupation coefficients respecting $\sum_{\mathrm{j}=1}^{\mathrm{N}} |\xi_{\mathrm{j},-\mathrm{j}}|^2 = 1$. Eq. (3.20) describes a quantum state displaying entanglement in the frequency domain, since the state is not factorizable between two states describing the signal and the idler separately.

Note that the resonances are not the reason for the frequency correlations; it is SFWM the cause. The resonances have simply the effect of discretizing the frequency domain and correlations. SFWM itself produces frequency correlations, but on a broad and continuous spectrum.

Knowing the frequency and time of arrival of a certain photon, the knowledge about the frequency and arrival time of its counterpart is also defined, within the time and frequency uncertainty relationship [85].

To conclude, we have shown how the quantum state of Eq. (3.11) displays frequency correlation. But, in order to effectively obtain energy-time entanglement to exploit it in a QKD setup, one must perform additional steps, which are better described in Sec. 4.4.

3.4 Four-wave mixing comb regimes

A resonating structure built using a $\chi^{(3)}$ material, namely a Kerr material, is called a Kerr resonator. When pumping a Kerr resonator with a CW pump, the joint effect of FWM and equally spaced resonances allows for the generation of a frequency comb.

A frequency comb is composed of equally spaced frequency components, corresponding in the time domain to a regular emission with a period equal to the inverse of the frequency separation. In some cases, depending on the phase relation between the emitted modes, a train of pulses is generated. In case the frequency comb emission corresponds to pulses in the temporal domain, the shorter the pulses, the wider the wavelength span of the comb [86]. Optical frequency combs (OFC) were initially invented as components of atomic clocks [87], converters from optical to RF frequencies, and as rulers for high precision spectroscopy [88]. Nowadays, OFC can be built using different technologies [88, 89], like e.g. with mode-locked lasers [90], electro-optic modulators inside a resonator [91], and using passive or active microresonators with Kerr non-linearities; these OFCs are here called Kerr combs [92, 93].

The theoretical framework used to describe the generation and evolution of Kerr combs is the one described by the Lugiato-Lefever Equation (LLE) [94].

These equations yield different types of Kerr combs, each associated with a distinct intracavity power regime defined by the pump power and detuning from resonance. We will now describe different Kerr comb regimes achievable in a Kerr resonator and compare them with our experimental observations.

Given a certain pump power input into the chip, it is possible to plot the behavior of the intracavity power as a function of the detuning, see Fig. 3.4.

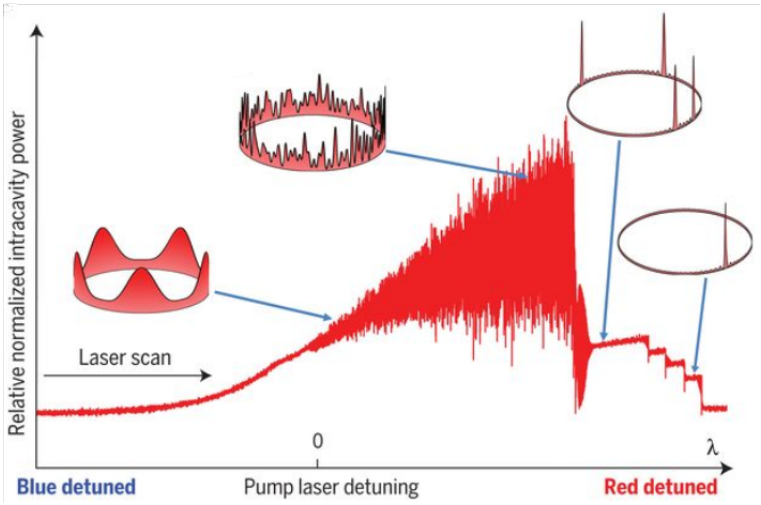

Figure 3.4: Behavior of the intracavity power as a function of the laser detuning in a Kerr resonator. The x-axis represents the detuning between the pump frequency and the cold-cavity (unshifted) resonance of the fundamental mode. From left to right: we represent Tuning rolls, modulation instability, multiple solitons, and single soliton regimes. Image taken from [92].

First, we recall the definition of detuning we have given through Eq. (2.6), which is: $\delta = f_{\mathrm{p}} - f_{0,\mathrm{cold}}$ where $f_{0,\mathrm{cold}}$ represents the resonance frequency in the absence of thermo-optic shifts. We distinguish four different regimes. Starting from the blue detuned side of the resonance ($\omega_{\mathrm{p}} > \omega_{0,\mathrm{cold}}$), the first regime is the primary comb or Turing rolls [21, 92, 95, 96]. Here, the frequency sidebands generated are separated by a discrete number of $FSRs$ of the cavity (mode spacings Δ of the order of THz). In agreement with this prediction, in Fig. 3.5, we show a primary comb generated by our Si_3N_4 microring, we find $\Delta = 12 \cdot FSR$.

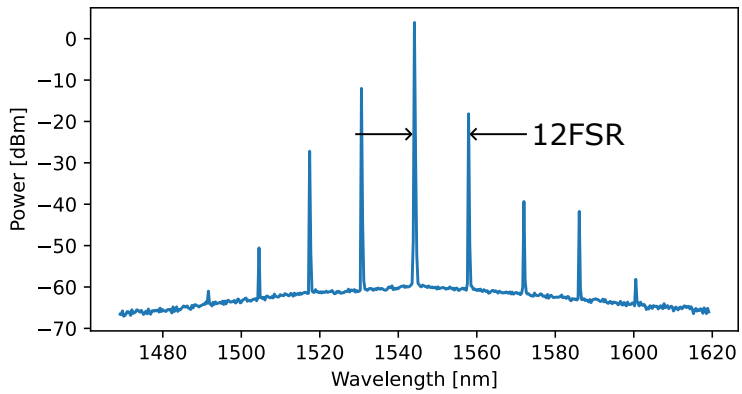

Figure 3.5: Frequency comb generated by the Si_3N_4 microring resonator. Note that the line spacing is equal to $\Delta = 12 \cdot FSR \sim 1.8\,\mathrm{THz}$ or $14.4\,\mathrm{nm}$.

The integer N, such that $\Delta = N \cdot FSR$, varies with the material and geometry of the resonator. Its value depends, in fact, on the interplay between the four-wave-mixing phase-matching conditions and the resonator's geometrical and optical constraints [97, 98]. Primary comb modes emerge at frequencies corresponding to the maximum overlap between the parametric gain profile and the cavity resonance spectrum, see Fig. 3.6 for the qualitative idea.

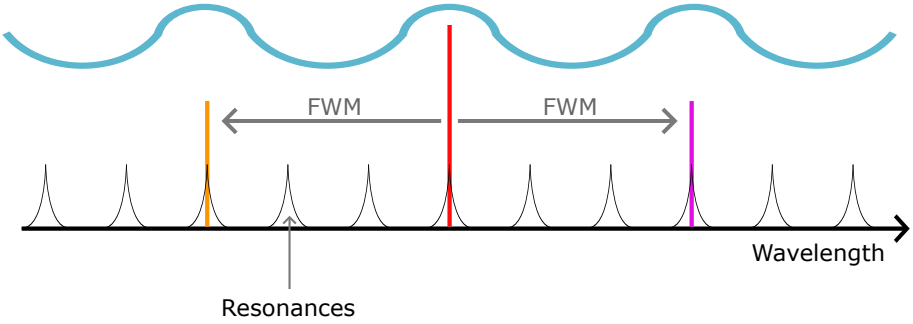

Figure 3.6: Schematic explanation of the generation of the sidebands separated by $\Delta = N \cdot FSR$ during the primary comb regime, in this example $N = 3$. In red, the two pump photons, in purple, the signal photon, in orange, the idler photon, and in blue, the parametric gain spectrum.

By increasing the pump laser detuning toward resonance, which corresponds to a higher intracavity power, a so-called "secondary comb" can be generated. This regime is characterized by the onset of degenerate and non-degenerate four-wave mixing, leading to the appearance of additional frequency components around the pump and near the sidebands of the primary comb. Again, in agreement with this prediction, in Fig. 3.7, we show the secondary comb generated by our ring.

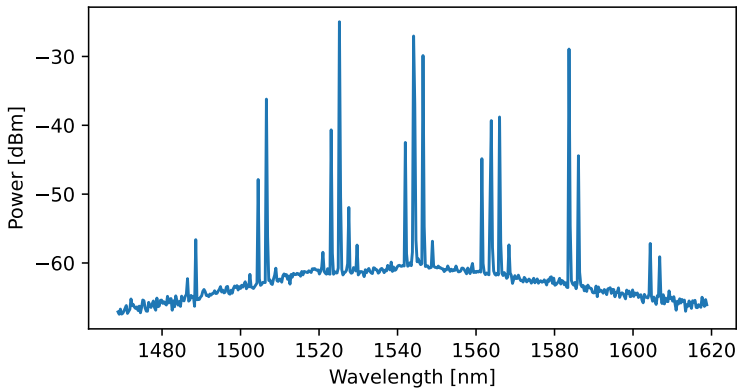

Figure 3.7: The secondary comb generated in the Si_3N_4 microring.

Shifting the detuning further, i.e., continuing to increase the intracavity power, all the resonator modes are populated by FWM. In Fig. 3.8b, we show that all 12 resonances are populated. Most of the generated sidebands achieved enough power to act as pump

photons for additional FWM. Such a condition is usually unstable (phase and amplitude noise affect multi-wavelength emission), and it may correspond to different types of regimes, like "breathers" [46, 99] or modulation instability [100]. It is not immediate to differentiate between the unstable regimes, since their output spectrum is similar. The main differences are in the temporal behavior of the oscillations inside the cavity, see [21, 101] for some simulations.

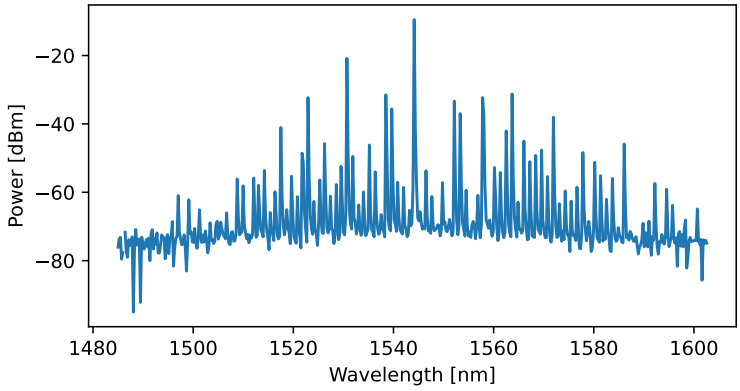

(a) Whole comb spectrum.

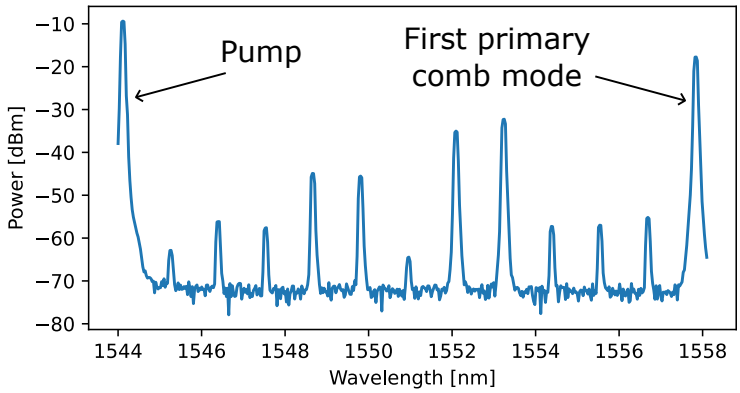

(b) Zoom of the spectrum between the pump and the first primary comb mode.

Figure 3.8: Unstable comb regime spectrum where all the resonances of the microresonator are populated. The ring was pumped with an input power $P_{\mathrm{p}} \approx 18\,\mathrm{dBm}$.

In Fig. 3.8, we show an example of unstable regime spectrum generated from the Si_3N_4 microring that we tested. From the figure, we can observe that the envelope of the spectrum exhibits irregular behavior, which we argue is characteristic of unstable regimes.

Reducing the effective detuning more, we surpass the instability regime, and the resonator enters the solitonic regime. Such a regime is characterized by a reduction in the circulating power, see Fig. 3.4. It happens because less power is necessary to sustain the oscillations within the resonator, thus the output comb can be more intense. Solitons

are self-reinforcing waves, which can maintain their speed and shape during time [102]. Optical solitons in Kerr materials are called dissipative Kerr solitons (DKS). Their self-reinforcing nature is due to the balance between dispersion and Kerr effect, and linear losses and parametric gain [92, 103].

It is important to note that fixing the detuning and instead tuning the input power does not reproduce the same dynamical regimes shown in Fig. 3.4. In fact, while the same intracavity power can be reached, which is sufficient to enter unstable regimes, the stability and behavior of the cavity depend critically on whether the pump is blue- or red-detuned relative to the cavity resonance. In particular, the self-sustained formation of temporal Kerr solitons requires the pump to be red-detuned [46].

The ring resonator used in this work did not support soliton formation, likely due to its dispersion properties. Moreover, we did not pursue this regime further, as the focus of this thesis is on below-threshold OPO operation and the generation of entangled states of light.

In summary, the regime reached in a non-linear microresonator depends on the circulating power and the phase-matching conditions. The parameters we can actively control to tune the regime are the effective detuning (including thermal effects) and the pump intensity. The observation on our ring are: (a) $P_\mathrm{p} \sim 5\,\mathrm{dBm}$, the OPO threshold is not reached, so only spontaneous four-wave mixing (SFWM) occurs (b) $P_\mathrm{p} \sim 15\,\mathrm{dBm}$, the system exhibits primarily spontaneous processes but can reach stimulated FWM, generating a primary comb with $N = 12$ (c) $P_\mathrm{p} \sim 18\,\mathrm{dBm}$, the ring exhibits both spontaneous and stimulated degenerate FWM, and also enters a regime of instability corresponding to degenerate and non-degenerate FWM. Overall, these kinds of systems display clear threshold behavior.

From this point onward, whenever we refer to the primary comb regime in the ring under study, unless otherwise specified, we will assume it corresponds to the comb with $N = 12$.

3.4.1 Simulations

Here, we present a selection of numerical results oriented to qualitatively predict the dynamical evolution of the comb regimes within the microresonator. They have been obtained using an in-house MATLAB simulator to integrate the LLE for parameters close to the experimental ones.

We start with a generalized version of the LLE for an active or a passive ring resonator in the presence of coherent injection in a longitudinal reference frame rotating in the resonator at the group velocity of the radiation [104]:

$$\tau_\mathrm{L}\frac{\partial E}{\partial t} = E_\mathrm{p} + (-1 - i\theta_0)E + (d_\mathrm{R} + id_\mathrm{I})\frac{\partial^2 E}{\partial z^2} + \mu(1 - i\Delta)(1 - |E|^2)E \tag{3.21}$$

where E_p and E are the normalized (dimensionless) slowly varying envelopes of the injected (pump) electric field and of the intracavity electric field, respectively [105, 106]. $\theta_0 = (f_0 - f_\mathrm{p})/\Delta\nu = (\omega_0 - \omega_\mathrm{p})\tau_\mathrm{L} = -2\pi\delta_{eff}\tau_\mathrm{L}$ is the normalized detuning, and d_R and d_I account for both field diffusion and dispersion. $\mu < 0$ is the unsaturated absorption/gain coefficient and Δ is linked to the system Kerr non-linearity.

Now, it is possible to simplify the latter equation, considering a passive resonator, in the form:

$$\frac{\partial F}{\partial \tau} = F_{\mathrm{p}} - [1 + i(\theta - |F|^2)]F + i\frac{\partial^2 F}{\partial \eta^2} \tag{3.22}$$

where $\theta = \theta_0 + \mu\Delta$, $F_{(\mathrm{p})} = \sqrt{\mu\Delta}E_{(\mathrm{p})}$, $\tau = t/\tau_{\mathrm{L}}$, and $\eta = z/\sqrt{d_{\mathrm{I}}}$. We transformed the variables t and z into dimensionless quantities, which is a standard procedure to make numerical integration more efficient.

We ran the simulation sweeping θ_0 from -2 to 2, which in physical quantities corresponds to a sweep of 4 FWHMs centered around a resonator resonance (which corresponds to $\delta_{\mathrm{eff}} = 0$). We used the data obtained through the COMSOL simulations in Sec. 2.1.4 to estimate the dispersion parameter $d_{\mathrm{I}} = -v_{\mathrm{g}}^3\kappa_2\tau_{\mathrm{L}}/2$. Instead, F_{p} was defined using a trial-and-error approach, since its scaling is based on quantities that are not directly measurable in an optical laboratory.

Note, this mathematical model does not take into account the thermo-optic effect; therefore, the resonance bending is only due to the Kerr effect.

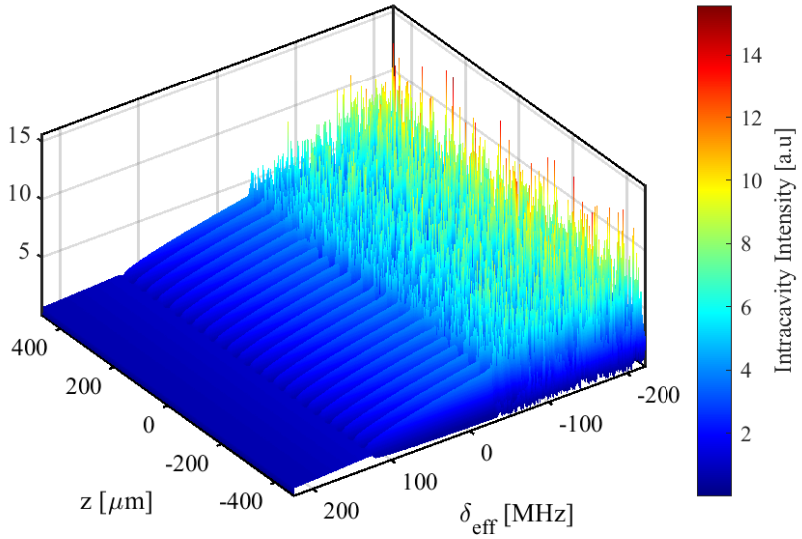

(a) Intracavity intensity in arbitrary units as a function of the effective detuning and the ring longitudinal direction.

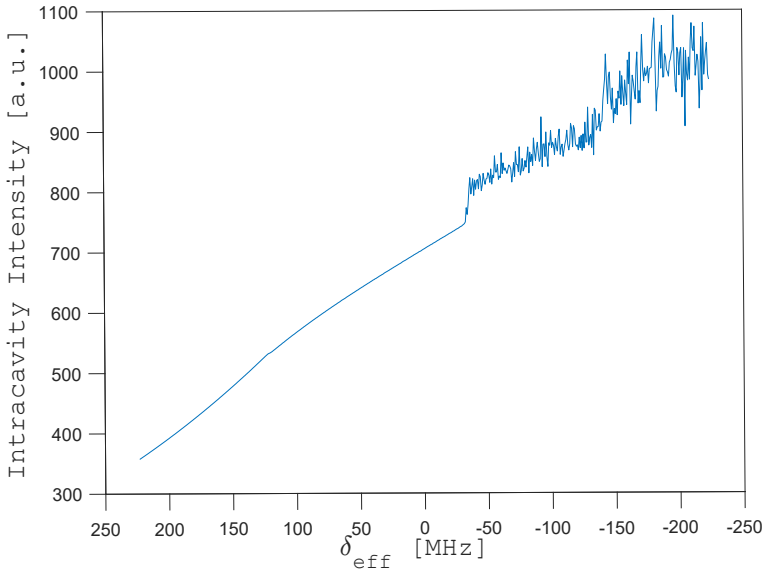

(b) Intracavity intensity in arbitrary units as a function of the effective detuning.

Figure 3.9: Behavior of the intracavity intensity and power during δ_{eff} sweep from $2\Delta\nu$ to $-2\Delta\nu$, with $\Delta\nu$ the resonator linewidth approximated to $\Delta\nu = 112\,\text{MHz}$. The simulation was performed with $E_{\text{p}} = 2.4$.

In Fig. 3.9, we show the results of simulations. In Fig. 3.9b, we are reconstructing only a small portion of the behavior described by Fig. 3.4. Of more interest is Fig. 3.9a,

because it shows the generation of periodic patterns of light within the resonator. At $\delta_{\text{eff}} \approx 120\,\text{MHz}$ we observe the generation of a regular and periodic oscillation. We recall that the reference system is moving in the ring at the group velocity of the radiation; whatever is displayed in the graph is actually rotating at speed v_{g}.

These results align well with our predictions. For $\delta_{\text{eff}} \gtrsim 120\,\text{MHz}$ we do not see any periodic structure within the resonator, which is congruent with the results of Fig. 5.10, where we show that for $\delta_{\text{eff}} \lesssim 130\,\text{MHz}$ we enter the stimulated region. The periodic structure generated for $120\,\text{MHZ} \gtrsim \delta_{\text{eff}} \gtrsim -35\,\text{MHz}$ is effectively a Turing rolls pattern; we will investigate it.

Interestingly, we can also predict the triggering of a chaotic regime after the first rolls, which aligns with our experimental observations.

Now, we want to better understand the type of Turing rolls that are generated right after the OPO threshold is surpassed. We performed a simulation fixing $\theta_0 = -\delta_{\text{eff}} 2\pi\tau_{\text{L}}$ with $\delta_{\text{eff}} = 50\,\text{MHz}$, and obtained the results shown in Fig. 3.10.

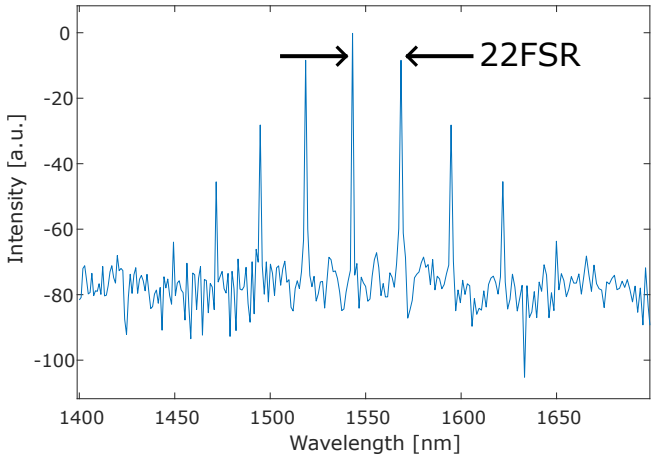

(a) Turing rolls spectrum.

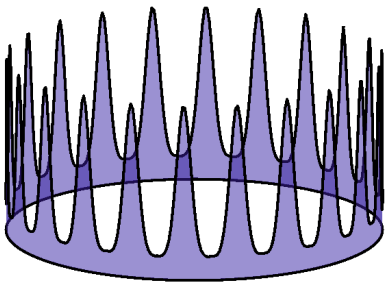

(b) Qualitative idea of the wave circulating within the microring.

Figure 3.10: Turing rolls simulated with $E_{\text{p}} = 2.4$ and $\delta_{\text{eff}} = 50\,\text{MHz}$.

The spectrum in Fig. 3.10a is really similar to that observed in the laboratory shown

in Fig. 3.5. But, there is a substantial difference, $\Delta_{\text{sim}} = 22$ while $\Delta_{\text{exp}} = 12$. Therefore, our simulation states that in our condition we should observe rolls with 22 maximums, see Fig. 3.10b, while in reality we only have 12. In the simulator, we empirically found that tuning the space variable $\eta = z/\sqrt{d_{\text{I}}}$, we are able to easily modify the number of rolls. If we want a smaller number of rolls, one needs to use a smaller cavity, in the sense of the normalized variable η. Therefore, the main limitations to finding a coincidence between simulation and experiment could be in estimating d_{I}, which contains the dispersion terms. Due to the third-order dependence on the group velocity, a small change in v_{g} can significantly modify the value of d_{I} and supposedly help in achieving a better congruence.

In conclusion, we qualitatively reproduced the experimental dynamical observations simulating the Lugiato-Lefever Equations in a one-dimensional resonating geometry. To find a complete overlap between simulations and experiment, we should use more complex mathematical tools and models. The model we used for the LLE makes some assumptions that can modify the behavior, such as neglecting thermo-optic red-shifts of the resonance, not considering the radial dimension of the waveguide of the ring, or considering a constant v_{g} or κ_2 over the whole spectrum.

3.5 Source characterization

We wanted to characterize the performance of the microring as a source of entangled states of light generated through SFWM. The parameters estimated to check if quantum correlations are present are the photon-pair generation rate (PGR), the coincidence-to-accidental ratio (CAR), and the heralding efficiency. All the parameters are widely employed in literature to describe the performances of a Kerr resonator [13, 72, 107, 108]. The PGR describes how many correlated photons are generated for a given input power. The CAR is a setup-dependent parameter; it specifies the ratio of correlated photon pairs over the background photon pairs in a given interval of time, and it is analogous to the signal-to-noise ratio (NSR). Lastly, given a detection event on the idler (or signal) channel, the heralding efficiency defines the probability of having a detection event on the signal (or idler) channel.

All of the parameters rely on the measurement of the cross-correlation between two symmetric modes, namely the SFWM signal and idler. This measurement will be better described in a later section (Sec. 4.2), but for ease of understanding of the current section, a brief description will be given here. Photons generated through SFWM are correlated in time. This feature can be unveiled by sending the signal and idler photons to two separate SNSPDs, and using a cross-correlation measurement, which means studying the number of detector clicks between two SPDs as a function of the click time delay between the two. If the emitted photons exhibit time correlation, the cross-correlation data will show a double exponential peak centered at zero time delay.

The three parameters were evaluated as a function of the input power, always minimizing δ_{eff}, thus maximizing the intracavity power and the generation process. To do so, one simply needs to tune the laser forward until the point before the generation is lost. It can be empirically seen by monitoring the coincidence plot that, when SFWM is active,

a peak is present. If the resonance is surpassed, then the cross-correlation measurement will just show a flat background. As stated at the beginning, we wanted to characterize the SFWM performances of the source; therefore, the OPO threshold was never reached, and the stimulated process was never initiated.

3.5.1 Coincidence-to-Accidental Ratio (CAR)

The coincidence-to-accidental ratio or CAR is calculated as [13]:

$$CAR = \frac{C - A}{A} \tag{3.23}$$

where C is the integral of the central peak coincidence counts in a given window around the origin, while A is the integration of the coincidences far from the peak, with the same window width, see Fig. 3.14. The coincidence window must be defined carefully; an integration window too small will return CAR values unexpectedly high. While increasing the integration span would lower the CAR. In literature, there have been used different window sizes, but the important point is to always specify it. A good choice is to use the $FWHM$ of the coincidence peak [109, 110]. This choice allows for using a window size that depends on the peak size, but it is independent of the peak lineshape.

The CAR depends on the pump power following a behavior similar to the one shown in Fig. 3.11. With low pump intensities, the emitted photons are not detected correctly since their events are covered by background photons and dark counts of the detector [110]. Therefore, there is a majority of accidental counts returning a low CAR. Then, the coincidence-to-accidental ratio increases until a maximum point. Further increasing the pump, the CAR lowers because the pump photons cannot be easily filtered. Moreover, at higher power, the probability that a circulating photon pair stimulates the emission of another pair is higher, which reduces the CAR [110, 111].

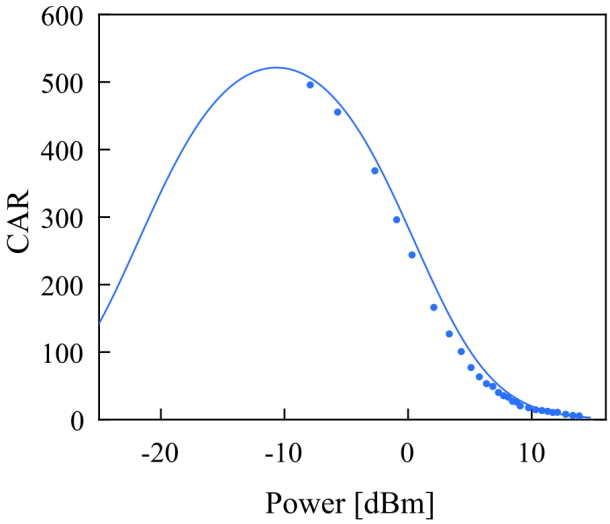

Figure 3.11: Example of the behavior of the CAR as a function of the on-chip power. Image taken from [110].

CAR is a parameter that not only characterizes the source, it strongly depends on the experimental apparatus. The main limiting factors are: pump filtering after the ring, since any pump photon reaching the detectors will contribute to the accidental counts. Length of the fibers from the ring to the pump rejection station, because Raman scattering may generate photons at the signal and idler wavelengths. The generation of photons through Raman scattering is directly proportional to the fiber length [53, 112]. One last important feature of the experimental setup is the detection efficiency of the detectors. A lower detection efficiency would make it harder to reconstruct a high peak over the flat accidental background.

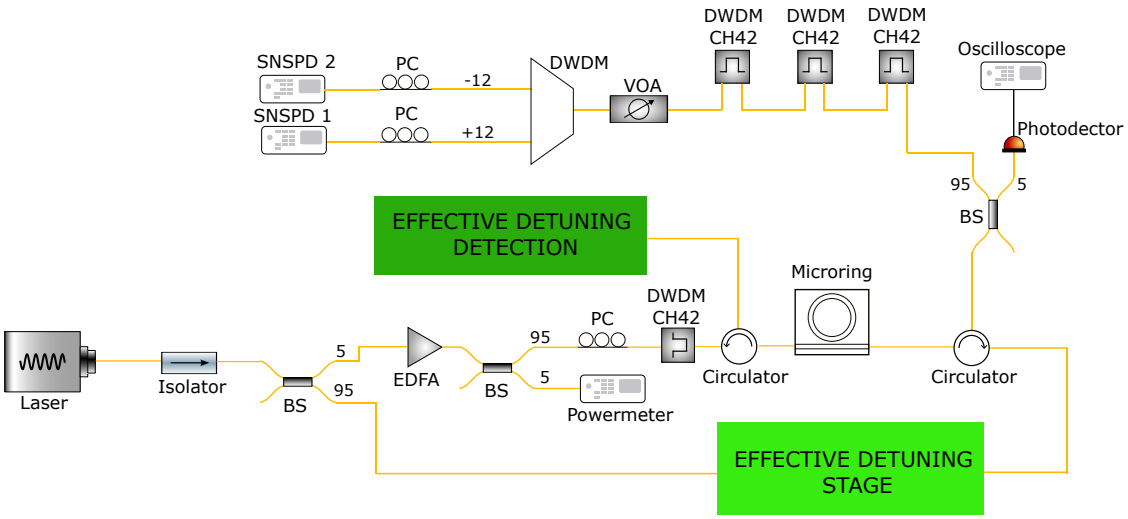

Figure 3.12: Experimental setup used for the characterization of the CAR and the PGR. The power meter after the EDFA is necessary to monitor the power pumping into the microring. The photodetector before the cascade of three DWDM filters is useful to monitor the transmission. The cascade of three DWDM filters is a pump rejection section, fundamental to removing accidental photons. Note, the part of the setup relative to the effective detuning is not necessary.

We measured the CAR between the modes ± 12, which are the first primary comb modes, and they have the strongest generation rate, also, below the OPO threshold. They were chosen due to the higher emission rate at lower pump powers, in contrast with the non-primary comb modes. In Fig. 3.12, the experimental setup used for the characterization of the CAR is shown. Note, the section relative to the measurement of the effective detuning is present, but we did not need it. For every pump power, the detuning was always minimized in order to achieve the highest generation rate possible. The most critical point in the apparatus is the cascade of three DWDM filters placed before the optical attenuator (VOA). Their role is to filter the pump as much as possible, since, as stated before, it is a source of accidental counts. Another important point is the DWDM placed right after the EDFA, which is aimed at removing the Amplified Spontaneous Emission (ASE) noise, which is the noise generated by the EDFA. The ASE is a broad-spectrum noise generated by the amplification of the background photons inside

the EDFA. In Fig. 3.13, we show our experimental estimation of the CAR as a function of the on-chip power. The on-chip power was evaluated by monitoring the power meter and then rescaling its reading after measuring all the losses from the power meter to the chip.

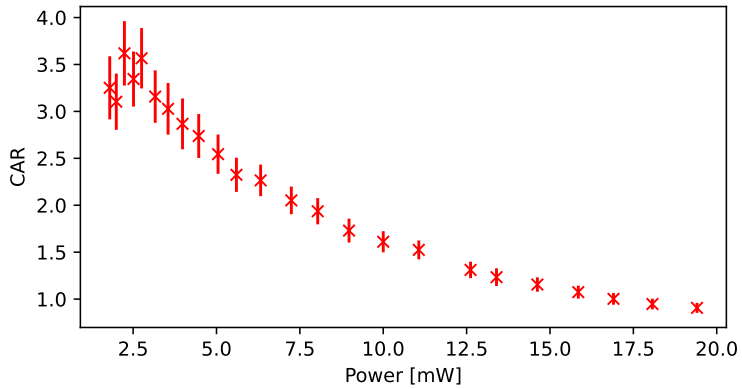

Figure 3.13: Experimental estimation of the CAR parameter as a function of the on-chip power.

The estimation of the CAR and its uncertainty was done in the following way, taking inspiration from [113], see Fig. 3.14 for a visual representation. The coincidence plots were fitted with the equation:

$$f = \begin{cases} Ae^{\frac{x_0 - x}{\tau_{\text{left}}}} + b & if\ x < x_0 \\ Ae^{-\frac{x - x_0}{\tau_{\text{right}}}} + b & if\ x >= x_0 \end{cases} \tag{3.24}$$

The $FWHM$ window is centered on the left and right sides of x_0, respectively, at $x^{(1)}_{\text{FWHM}} = -\tau_{\text{left}} \ln 2 + x_0$ and $x^{(2)}_{\text{FWHM}} = \tau_{\text{right}} \ln 2 + x_0$. Obviously, $x^2_{\text{FWHM}} - x^1_{\text{FWHM}} = FWHM$. To calculate the "good" coincidences, namely those generated by SFWM, we integrated the function $f - b$ between x^1_{FWHM} and x^2_{FWHM}, obtaining $C - A = 0.5 \cdot A \cdot (\tau_{\text{left}} + \tau_{\text{right}})/bin\_width$. Then, we integrated f far from the peak, where the exponential can be assumed to be zero, with a window large $FWHM$ to estimate the accidental coincidences $A = b \cdot FWHM/bin\_width$. Both coincidence values are divided by the bin_width, which is the dimension of a bin in time in the coincidences histogram. This is necessary because we need to discretize the x-axis of our fit in bins, like the data acquisition software did (TimeTaggerLab). The uncertainty on $C - A$ and A was estimated using the propagation law of the uncertainties, starting from the fit parameters. The uncertainty of the fit parameter was extracted automatically from the fitting algorithm in Python.

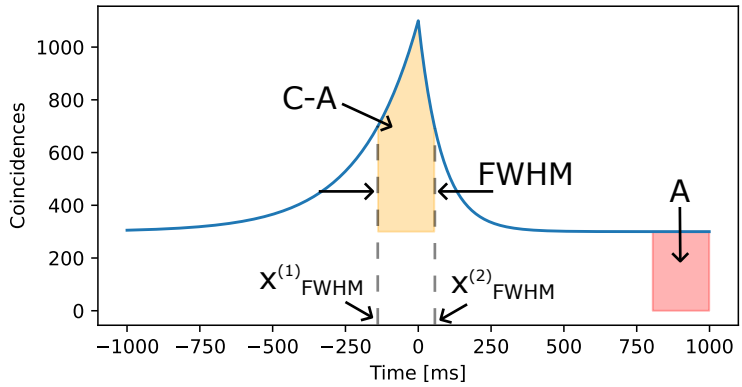

Figure 3.14: Visual representation of how the calculation of the fitted curve was performed.

The resulting behavior of the CAR follows the expected trend. Initially, the CAR is maximized, while at high on-chip power, it lowers due to the frequent accidental coincidences. It was not possible to appreciate the growing trend at low powers, as the acquisition time would have been too high (days or even longer). We are only able to reproduce the decreasing part of the curve shown in Fig. 3.11. Usual CAR values are at least two or three orders of magnitude bigger than what we measured [107–110, 113, 114]. The highest CAR measured by us was 3.6(3), which is definitely small in comparison with the state of the art. Such a low result can be due to different reasons. Low pump rejection, we are using three DWDM filters with a 30 dB filtering capability each, adding a filter could reduce the accidental counts. Moreover, the filter responsible for the ASE removal can have some ripples, namely some non-zero pass-band outside the DWDM channel-42. This unwanted radiation is then reflected by the pump rejection stage, sent to the SNSPDs, and will contribute to the degradation of the CAR. In addition, the signal and idler photons may experience losses or other non-idealities in the ring, which could cause inelastic scattering or absorption, therefore transforming a "good" coincidence into a "bad" one. Lastly, such a low value can be due to the type of mode chosen. The resonances ±12 are the first primary comb sidebands, thus very prone to the emission of stimulated FWM, which does not produce independent photon pairs. Because the multi-pair generation, due to the stimulated effect, correlates the photon pair with other pairs. We did not measure it, but the CAR measured on non-primary comb resonances may be higher, since they are less affected by the stimulated process.

3.5.2 Photon Pair Generation Rate (PGR)

The other parameter experimentally characterized was the photon-pair generation rate. From equation Eq. (3.17) we see that the emission of SFWM photons depends on the square of the power coupling into the ring. The PGR is defined as the number of photons emitted per unit of P_p^2. Starting from equation Eq. (3.17) and simplifying it we obtain

the PGR:

$$PGR = \frac{\gamma_{\mathrm{NL}}^2 Q^3 v_{\mathrm{g}}^4}{\omega_{\mathrm{p}}^3 R^2 \pi^2} \tag{3.25}$$

Using the simulations and results from Sec. 2.1.4, we can estimate the photon-pair generation rate. The values inserted in the equation are $Q = 1.765$ (average of Q_1 and Q_2), $v_g = 1/k_1$ with $k_1 = 6.944 \times 10^{-9}\,\mathrm{s/m}$, $\omega_{\mathrm{p}} = 194.228\,\mathrm{THz}$. While, $R = 182.3\,\mu\mathrm{m}$ was obtained using Eq. (2.3), where $n = 1.8368$ and $FSR = 142.6\,\mathrm{GHz}$. The estimation of γ_{NL} was performed using Eq. (3.13), where $A_{\mathrm{eff}} = 1.16\,\mu\mathrm{m}^2$, while n_2, which is the non-linear refractive index or Kerr coefficient, had to be qualitatively chosen. The non-linear refractive index heavily depends on the fabrication process and material properties [115]. It describes the variation of the linear refractive index as a function of the circulating power, effectively the Kerr effect [116]. Since the microring was fabricated using LPCVD [117] and given the similar waveguide dimensions with [118], we chose to take the n_2 value they report, which is $1.1 \times 10^{-19}\,\mathrm{m}^2/\mathrm{W}$. The resulting PGR is $593.308\,\mathrm{kHz/mW}^2$, no uncertainty range is reported, since the parameter estimation was not precise, especially for n_2. Therefore, this result can be considered a qualitative estimation of the photon-pair generation rate.

The experimental estimation of the PGR was performed following the work done in articles [107, 109]. The experimental setup used is still the one shown in Fig. 3.12. For a given input power, we measured the coincidences and the single counts of modes ± 12. Then, the singles counts were fit using the following equation:

$$f_{\mathrm{s/i}} = a_{\mathrm{s/i}} P_{\mathrm{in}}^2 + b_{\mathrm{s/i}} P_{\mathrm{in}} + c_{\mathrm{s/i}} \tag{3.26}$$

where $a_{\mathrm{s/i}} = \eta_{\mathrm{s/i}} PGR$ ($\eta_{\mathrm{s,i}}$ is the transmissivity), $b_{\mathrm{s/i}}$ is the linear contribution accounting for noise effects (such as Raman), and $c_{\mathrm{s/i}}$ takes into account the constant background.

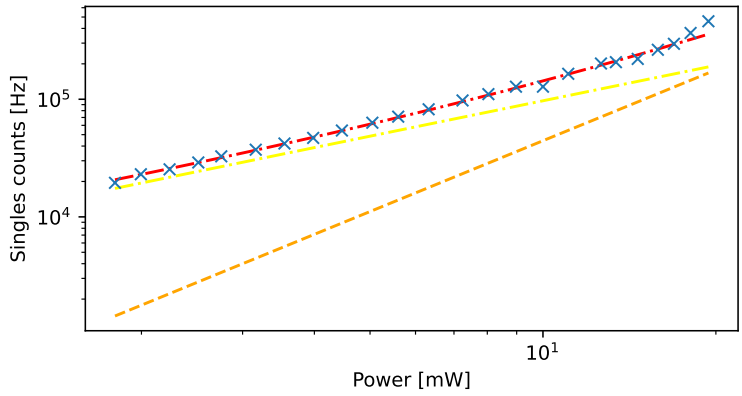

(a) Mode -12. Fit parameters are $a_{-12} = 443.0(6)\,\mathrm{Hz/mW^2}$, $b_{-12} = 9.704(9) \times 10^3\,\mathrm{Hz/mW}$, and $c_{-12} = 1.78(2) \times 10^3\,\mathrm{Hz}$.

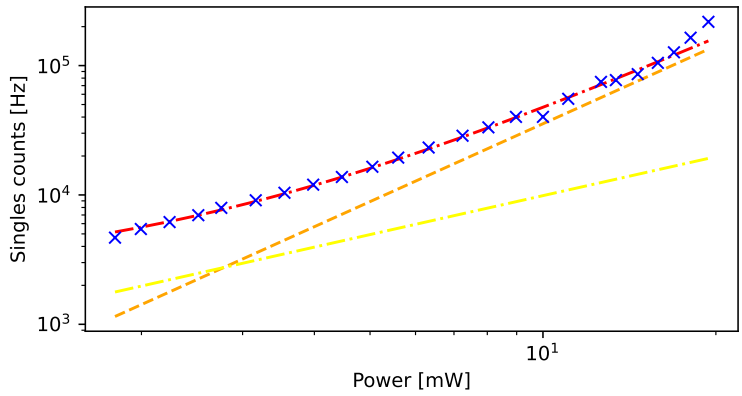

(b) Mode $+12$. Fit parameters are $a_{+12} = 355.1(4)\,\mathrm{Hz/mW^2}$, $b_{+12} = 986(5)\,\mathrm{Hz/mW}$, and $c_{+12} = 2.244(13) \times 10^3\,\mathrm{Hz}$.

Figure 3.15: Singles counts of modes ± 12. In blue, the experimental data. In red, the fit. In orange, the quadratic component of the fit. In yellow, the linear component of the fit.

In Fig. 3.15 we show the experimental data and fit curves. Note how mode -12 experiences a higher level of noise (Fig. 3.15a) than mode $+12$ (Fig. 3.15b). The latter could be due to different optical paths or other differences in the frequency channels. The power reported on the x-axis of the figures is the estimation of the actual power reaching the Si_3N_4 microring. We calculated all the losses separating the power meter and the microchip, then we estimated the waveguide-fiber coupling losses by measuring the power in and out of the chip, minimizing the coupling in the ring with the PC. The waveguide-ring coupling was not estimated experimentally, but only qualitatively.

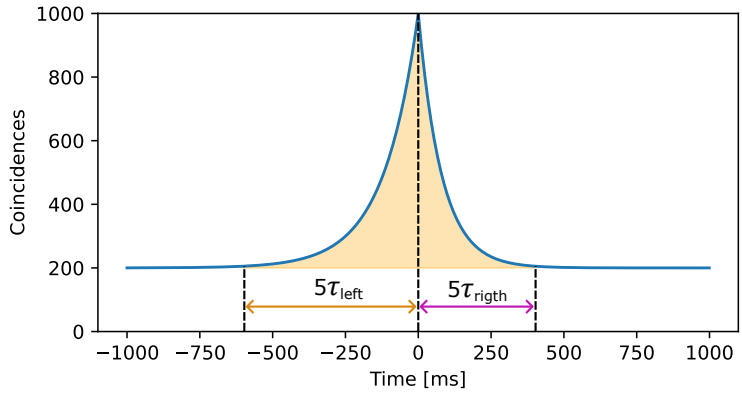

Figure 3.16: Example of the calculation of the photons generated through SFWM at a given input power. Note, we used different exponential time constants in the example to make it as generic as possible. The orange area represents the number of generated photons through SFWM.

At every pump power, we also analyzed the coincidence data, as in the CAR estimation, the integral of the coincidence peak was performed. In this case, the whole peak was considered, since all the coincidences lying above the constant background can be assumed to be generated by SFWM. Therefore, the integration distance from the center was five times the exponential constant, see Fig. 3.16. Performing the integral of Eq. (3.24) between $-5\tau_{\text{left}} + x_0$ and $5\tau_{\text{right}} + x_0$ returns $-A(e^{-5} - 1)(\tau_{\text{left}} + \tau_{\text{right}})$. Afterward, we analyzed the coincidences as a function of the pump power, which were fit using the following equation:

$$f_{\text{cc}} = a_{\text{cc}} P_{\text{in}}^2 \tag{3.27}$$

where $a_{\text{cc}} = \eta_{\text{s}}\eta_{\text{i}} PGR$. In Fig. 3.17, the resulting data and fit are shown. We note how, at high power, therefore close to the stimulated regime, the fit curve is not aligned with the data points. This is due to the stimulated FWM effect that is taking over as the main generation process within the resonator since we are approaching the OPO threshold.

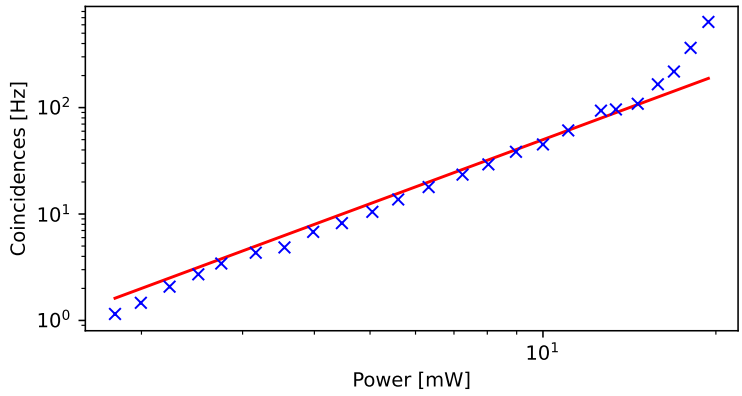

Figure 3.17: Coincidences as a function of the on-chip power. In blue, the experimental data. In red, the fit. Fit parameter is $a_{\mathrm{cc}} = 0.500(3)\,\mathrm{Hz/mW^2}$.

All uncertainties reported from now on are obtained from the fit algorithm and propagated to the final quantities. It is now possible to estimate the transmissivity/losses experienced by the signal and idler photons from the generation to the detection. $\eta_{+12} = a_{\mathrm{cc}}/a_{-12} = 1.125(6) \times 10^{-3}$ and $\eta_{-12} = a_{\mathrm{cc}}/a_{+12} = 1.407(8) \times 10^{-3}$, they correspond, respectively, to losses of $\alpha_{+12} = 29.49(2)\,\mathrm{dB}$ and $\alpha_{-12} = 28.52(2)\,\mathrm{dB}$. These results are consistent with other experiments [109] and with our experimental setup. We can estimate the losses due to the microchip materials, waveguide-ring, and waveguide-fiber coupling to be responsible for $\sim 8\,\mathrm{dB}$ of losses. Then, the circulator adds $\sim 2\,\mathrm{dB}$, the DWDM filters around 3 dB all together, the VOA $\sim 2\,\mathrm{dB}$ of insertion losses, the DWDM demultiplexer is responsible for at least 6 dB of losses, and finally polarization controllers and detectors non-unitary efficiency can reach 3 dB. We reached 24 dB of losses without considering connections and other non-idealities in the setup. Therefore, the estimation of the losses, through the fits, experienced by the generated photons can be considered realistic. Then, the photon-generation rate is obtained as $PGR = a_{\mathrm{cc}}/(\eta_{+12}\eta_{-12}) = 316(3)\,\mathrm{kHz/mW^2}$. This result is not compatible, but of the same order of magnitude, with the theoretical estimation, but as we said earlier, it would have been unlikely that the results would have been similar. It is important to note that there are different criticalities in the estimation of the experimental PGR. First of all, the evaluation of the ring input power. We calculated it by measuring all the losses between the power meter and the ring, trying to consider also the coupling losses, which we did not quantitatively measure. We estimated that light exiting the BS after the EDFA undergoes $\approx 7\,\mathrm{dB}$ of attenuation before reaching the ring. For example, assuming an additional dB of losses, we would have obtained $PGR_{+1\mathrm{dB}} = 500(5)\,\mathrm{kHz/mW^2}$, while considering a lower attenuation, we get $PGR_{-1\mathrm{dB}} = 199.1(19)\,\mathrm{kHz/mW^2}$. Moreover, when approaching the ring resonance and the stimulated FWM process starts, the power pumping the non-linear process has the following relationship with coincidence counts [109, 119]:

$$P_{\mathrm{in}} = \sqrt{\frac{CC}{at^4}}(1 - r\tau(1 + CC\frac{b}{a})^{-1/4})^2 \tag{3.28}$$

where CC is the number of SFWM coincidences per second, α is the non-linear parameter linking CC and the circulating power, r and t are the reflection and transmission coefficients of the ring-waveguide coupling. b is the non-linear coefficient responsible for free carrier absorption, and $1-\tau$ is the round-trip amplitude reduction factor. Therefore, it is immediate to note how the relationship between the pump power and the coincidence counts is fragile, but at the same time fundamental for the estimation of the PGR.

3.5.3 Heralding efficiency

Using the results and the data acquired for the estimation of PGR and CAR, it is possible to calculate the heralding efficiency of the entangled photon source. This parameter describes the probability that, given a herald detection event, the heralded photon will also be detected. We evaluate the heralding efficiency, first, using the Klyshko efficiency [13, 120]:

$$\eta_{\mathrm{K}}^{\mathrm{s(i)}} = \frac{CC}{C_{\mathrm{i(s)}}} \tag{3.29}$$

where $C_{\mathrm{i(s)}}$ are the singles counts of the idler (signal) in the unit of time. The Klyshko efficiency is strictly dependent on the experimental setup. Higher attenuation between generation and detection will lower such a parameter; therefore, it must be used accordingly. In Fig. 3.18, the result is shown.

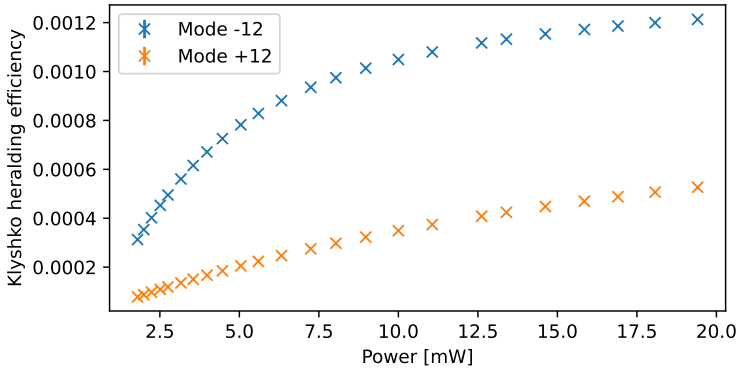

Figure 3.18: Klyshko efficiency evaluated for both the mode $+12$ and -12.

The maximum Klyshko efficiencies measured are $\eta_{\mathrm{K,max}}^{+12} = 5.267(10) \times 10^{-4}$ and $\eta_{\mathrm{K,max}}^{-12} = 1.213(2) \times 10^{-3}$ at $P_{\mathrm{in}} = 19.4\,\mathrm{mW}$. These values are low, meaning that once every $\sim$ a thousand herald photons, there is a coincidence with a correlated counterpart.

To estimate the heralding efficiency of the heralded single-photon source independently of the experimental apparatus, it is possible to use the intrinsic heralding efficiency [13]:

$$\eta_{\mathrm{I}}^{\mathrm{s(i)}} = \frac{\eta_{\mathrm{K}}^{\mathrm{s(i)}}}{\eta_{\mathrm{s(i)}}} \tag{3.30}$$

The latter parameter separates the Klyshko efficiency from the losses of the channels experienced by the two photons. It is therefore possible to estimate the performance of

the heralded single-photon source.

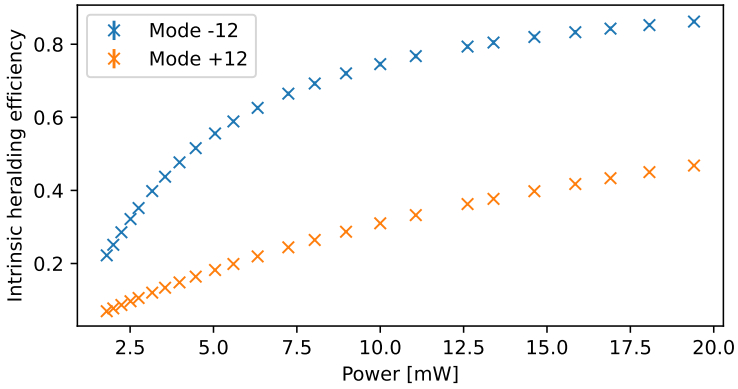

Figure 3.19: Intrinsic heralding efficiency evaluated for both the mode +12 and −12.

In Fig. 3.30, the intrinsic heralding efficiency is shown. The efficiency calculated for the mode +12 is lower than that calculated for mode −12. At the maximum input power of 19.4 mW, $\eta^{+12}_{\mathrm{I,max}} = 0.468(3)$ and $\eta^{-12}_{\mathrm{I,max}} = 0.862(5)$. Therefore, at the specified power, given a detection event of the mode −12, with a probability of 46.8(3) %, a photon of the mode +12 will be detected.

The discrepancy in the intrinsic heralding efficiencies is due to the different single counts measured on the two channels, see Fig. 3.15a and Fig. 3.15b. Different noise and losses experienced during the propagation toward the detection stage can be responsible for such a discrepancy. However, a more realistic cause is that the demultiplexer channel is poorly aligned with the mode emission frequency +12. The border of the filter pass-band probably cuts off some SFWM photons, thus lowering their counts, reducing CAR, and heralding efficiencies. The difference in transmissivity experienced by the two modes can be a result of both noise and attenuation differences, and of poor filtering. Therefore, we cannot state with certainty which effect is dominant.

The trend of the heralding efficiency as a function of the input power correctly aligns with those found in literature [121, 122]. The probability of detecting both signal and idler is reduced by Raman noise, which scales linearly while SFWM scales quadratically with power; therefore, linear noise is more present at lower power [121]. Then, increasing the input power, the heralding efficiency grows since the counts are scaling quadratically, overcoming linear noise photons.

When working with quantum information applications, it is preferable to have low input power. Since it coincides with a high CAR, and we will see this in a later section, the generated photons exhibit a good quantum nature. The drawback is that such a regime exhibits very low heralding efficiencies, $\eta^{+12}_{\mathrm{K,min}} = 7.82(6) \times 10^{-5}$ and $\eta^{-12}_{\mathrm{K,min}} = 3.13(3) \times 10^{-4}$. In a real-life application, where losses can be of the order of those present in our experimental setup, one must throw away thousands of photons just to obtain a single entangled state. Therefore, the balance between input power and CAR against the heralding efficiency must be carefully considered.

Chapter 4

Entangled states characterization

In this chapter, we present the characterization of the photons emitted by the microresonator. We studied the quantum nature of the photon pair using different approaches. The goal is to fully understand these properties, as a microresonator of this type could be integrated into an entangled-photons QKD protocol in the future or be used as a heralded single-photon source.

First, the autocorrelation of a single mode is presented. It is an important measurement that describes the nature of the photons emitted and their temporal statistics [123]. After that, we measured the cross-correlation between symmetric modes around the pump to show the temporal correlations [124]. Afterward, we measured the heralded second-order correlation; this parameter demonstrates the quantum nature of the emitted radiation [125]. It is essential to state that the microresonator can serve as a heralded source of single photons, which is crucial for implementing a QKD protocol. Lastly, we performed an interferometric measurement using an unbalanced interferometer. It allows us, again, to demonstrate the quantum nature of the emitted light and the time correlations within the photon pair. In addition, we are also able to state if these quantum correlations are non-local, and if, therefore, they imply entanglement. The measurement we performed is not a loophole-free violation of the Bell inequality. We did not rigorously violate the locality principle, and we also exploited the post-selection; therefore, the post-selection loophole (PSL) is not resolved as well.

All of these measurements focus on the measurement of coincidences between two or three photon channels; the coincidences must be recorded as a function of the arrival time delay between the channels. Therefore, it is mandatory to have single-photon detectors, in our case SNSPD (see Sec. 2.2), and high precision timing electronics. The latter consists of an instrument that can receive ultra-short, $\sim 40\,\text{ps}$, and frequent, $\sim 10\,\text{GHz}$, voltage pulses. It must be able to handle the signals emitted by the SPDs and extract the arrival time delay between them via software. In our experiments, we used a Time Tagger 20 by Swabian Instruments.

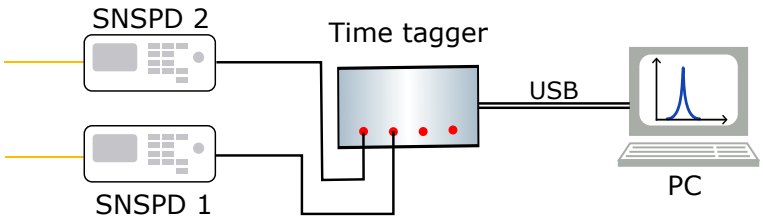

Figure 4.1: Schematic of the connections between the single-photon detectors, the time-tagging electronics, and the data software.

The connections among the devices necessary for the coincidence measurements are shown in Fig. 4.1. The time tagging electronics is acting as a gateway between the SNSPDs and the user computer. It transforms the short pulses generated by the SPDs into a digital transmission sent to the user's PC.

4.1 Autocorrelation

4.1.1 Theory

The autocorrelation of an optical beam is the second-order expansion of the single-beam n-th correlation function. The n-th order correlation function calculates the n-th order temporal correlation within the electric field. It can be generally expressed as [126]:

$$g^{(n)}(t_1, t_2, ..., t_n) = \frac{\langle E^{(-)}(t_1)...E^{(-)}(t_n)E^{(+)}(t_1)...E^{(+)}(t_n)\rangle}{\langle E^{(-)}(t_1)E^{(+)}(t_1)\rangle...\langle E^{(-)}(t_n)E^{(+)}(t_n)\rangle} \tag{4.1}$$

and setting $n = 2$:

$$g^{(2)}(t_1, t_2) = \frac{\langle E^{(-)}(t_1)E^{(-)}(t_2)E^{(+)}(t_2)E^{(+)}(t_1)\rangle}{\langle E^{(-)}(t_1)E^{(+)}(t_1)\rangle\langle E^{(-)}(t_2)E^{(+)}(t_2)\rangle} \tag{4.2}$$

where the quantized electric field at time t is $E(t) = E^{(-)}(t)+E^{(+)}(t)$, with $E^{(+)}(t) \propto \hat{a}(t)$ and $E^{(-)}(t) \propto \hat{a}^{+}(t)$ [127]. Eq. (4.2) describes the time correlation in the fluctuations of the electric field intensity at t_1 and t_2. Note that $g^{(2)}(t_1, t_2) = 1$ means that the fluctuations of the electric field intensities $I(t_1)$ and $I(t_2)$ are completely independent.

We can express the $g^{(2)}(t_1, t_2)$ as a function of the creation and destruction operators:

$$g^{(2)}(t_1, t_2) = \frac{\langle \hat{a}^{+}(t_1)\hat{a}^{+}(t_2)\hat{a}(t_2)\hat{a}(t_1)\rangle}{\langle \hat{a}^{+}(t_1)\hat{a}(t_1)\rangle\langle \hat{a}^{+}(t_2)\hat{a}(t_2)\rangle} \tag{4.3}$$

We can make further simplifications, naming $t_2 = t_1 + \tau$ and $t_1 = t$. Then we recall that the number operator $\hat{n}$, which is the operator that returns the number of photons in a given Fock state, is $\hat{n} = \hat{a}^{+}\hat{a}$:

$$g^{(2)}(\tau) = \frac{\langle \hat{n}(t)\hat{n}(t+\tau)\rangle}{\langle \hat{n}(t)\rangle\langle \hat{n}(t+\tau)\rangle} \tag{4.4}$$

Usually, the measurement is carried out using two different detectors, see Fig. 4.2:

$$g^{(2)}(\tau) = \frac{\langle \hat{n}_1(t)\hat{n}_2(t+\tau)\rangle}{\langle \hat{n}_1(t)\rangle\langle \hat{n}_2(t+\tau)\rangle} \tag{4.5}$$

where $\hat{n}_{1,2}$ are the number operators of the events recorded, respectively, by detectors 1 and 2. This last form is powerful, since it shows how the $g^{(2)}(\tau)$ describes the probability that two detectors would click more often simultaneously or not.

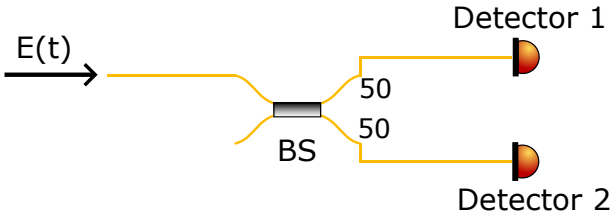

Figure 4.2: Simple schematic of the experimental setup used for the autocorrelation measurement.

We will now define the coherence time τ_c to make some insightful considerations about the autocorrelation function. τ_c can be defined as the time over which the electromagnetic field maintains its phase constant. During light propagation, its evolution is such that all its information previous to τ_c is lost. Therefore, the coherence time is a measure of how much the light can keep its form "fixed" during the evolution in time and space. An important relation is [128]:

$$\tau_c \propto \frac{1}{\Delta\nu_{ph}} \tag{4.6}$$

where $\Delta\nu_{ph}$ is the bandwidth of the photon. The quantitative relationship depends on the spectral lineshape, for example, for a Lorentzian lineshape it is [129]:

$$\tau_c = \frac{1}{\pi\Delta\nu_{ph}} \tag{4.7}$$

For $\tau >> \tau_c$ the correlations between the fluctuations are zero, since there is no shared information between waves distant more than the coherence time. Therefore, the $g^{(2)}(\tau)$ becomes:

$$g^{(2)}(\tau) = \frac{\langle \hat{n}_1(t)\hat{n}_2(t+\tau)\rangle}{\langle \hat{n}_1(t)\rangle\langle \hat{n}_2(t+\tau)\rangle} \xrightarrow{\tau>>\tau_c} \frac{\langle \hat{n}_1(t)\rangle\langle \hat{n}_2(t+\tau)\rangle}{\langle \hat{n}_1(t)\rangle\langle \hat{n}_2(t+\tau)\rangle} = 1 \tag{4.8}$$

Every optical radiation has a $g^{(2)}(\tau)$ that tends to 1 far from the origin for $\tau >> \tau_c$.

The value at $\tau = 0$ is also an important parameter; it changes depending on the type of temporal statistics of the radiation. It describes whether the generation exhibits a bunching in the emission, i.e, photons are likely to be emitted together, or anti-bunching, i.e., photons are likely to be emitted in single wavepackets.

Temporal statistics	$Var(\hat{\mathrm{n}})$	$g^{(2)}(0)$	$g^{(2)}(\tau >> \tau_c)$
sub-Poissonian	$< \bar{\mathrm{n}}$	< 1	1
Poissonian	$\bar{\mathrm{n}}$	1	1
super-Poissonian	$> \bar{\mathrm{n}}$	> 1	1

Table 4.1: Table showing the main properties of light with different emission temporal statistics.

A $g^{(2)}(0) = 1$ means that the field is perfectly coherent and that the photons have no particular correlation. It is demonstrated that a coherent radiation has a Poissonian temporal distribution of the wavepackets [71]. Which means that at a given time, the number of photons present follows a Poissonian distribution as:

$$p(\mathrm{n}) = \frac{\bar{\mathrm{n}}^{\mathrm{n}}}{\mathrm{n}!} e^{\bar{\mathrm{n}}} \tag{4.9}$$

where n is the number of photons, $\bar{\mathrm{n}}$ is the average number of photons, with $\bar{\mathrm{n}} = \langle \hat{\mathrm{n}} \rangle = P/(\hbar\omega)$ and P is the average optical power and ω the angular frequency. An important feature of the Poissonian distribution is that its variance is equal to the mean value:

$$Var(\hat{\mathrm{n}}) = \bar{\mathrm{n}} \tag{4.10}$$

If we have, instead, an optical beam with fluctuations smaller than the average number of photons, then the distribution is called sub-Poissonian. We have that $g^{(2)}(0) < 1$, which means that photons are emitted in single packets and are unlikely to be found in groups (bunches). This effect is called photon anti-bunching; it is a purely quantum effect and describes a quantum state of light. See Sec. 4.3 for a more detailed explanation.

If the fluctuations are larger than the average number of photons, then the distribution is called super-Poissonian and the radiation is named thermal or chaotic. Chaotic light displays a $g^{(2)}(0) > 1$, which means that light is usually emitted in bunches; it is more probable to find more than one photon at a time. This is typical of classical sources, e.g., light bulbs or multi-chromatic lasers.

In Tab. 4.1, we report the main properties of the three categories of temporal statistics that can be observed.

To retrieve the exact behavior of the $g^{(2)}(\tau)$, we need to understand its relationship with the frequency distribution of the beam. The Wiener-Khintchine theorem states that [130]:

$$PSD(\omega) \propto Re\{\int_0^\infty d\tau g^{(1)}(\tau) e^{i\omega\tau}\} \tag{4.11}$$

where $PSD(\omega)$ is the power spectral density of the radiation, and $g^{(1)}(\tau)$ is the first-order correlation function, which can be written as:

$$g^{(1)}(\tau) = \frac{\langle E^{(-)}(t) E^{+}(t+\tau) \rangle}{\langle E^{(-)}(t) E^{+}(t) \rangle} \tag{4.12}$$

The $g^{(1)}(\tau)$ measures the correlations in the fluctuations of the electric field, while the $g^{(2)}(\tau)$ measures the correlations in the fluctuations in the intensity of the field. The

relationship between the first and second-order correlation, for chaotic light, is given by [131]:

$$g^{(2)}(\tau) = 1 + |g^{(1)}(\tau)|^2 \tag{4.13}$$

Using Eq. (4.13) and Eq. (4.11), we note how the shape of the autocorrelation is strictly related to the spectral lineshape of the optical field. The quantitative relationship from which the proportionality of Eq. (4.6) arises comes from the Wiener-Khintchine theorem.

The temporal statistics of a single mode generated through SFWM is super-Poissonian, as a result of the amplification of vacuum fluctuations [72], and since we are working with light generated within a cavity, we assume that its lineshape is always Lorentzian, which allows us to write [131]:

$$g^{(2)}(\tau) = 1 + e^{-2\frac{|\tau|}{\tau_c}} \tag{4.14}$$

An important feature of a perfect thermal radiation is $g^{(2)}(0) = 2$, but it is not true for all super-Poissonian beams. We will show in the measurements that it is possible to measure an autocorrelation at zero delay $1 < g^{(2)}(0) < 2$. Thus, the specific value at zero delay gains importance.

Autocorrelation and purity

Given a biphoton quantum state of light, where each particle is emitted with thermal statistics, it is possible to estimate the purity of the state $\mathcal{P}$ using $g^{(2)}(0)$. Using the density matrix formalism, a quantum state has $\mathcal{P} = Tr\{\rho^2\}$. From the properties of a density matrix, we know that $Tr\{\rho\} = 1$, then the purity is bound by $1/d \leq \mathcal{P} \leq 1$ [132], where d is the dimension of the Hilbert space. When $\mathcal{P} = Tr\{\rho^2\} = 1$, then we are dealing with a pure state. If the purity is < 1, then the state is mixed and ρ is a statistical superposition of pure states. For example, in the case of a qubit 2-dimensional Hilbert space, the completely mixed state is $\rho = \mathbb{I}/2$, with $\mathbb{I}$ the identity matrix, it turns out that $\mathcal{P} = Tr\{\mathbb{I}^2/4\} = 0.5 = 1/2$.

To give a more formal description of the purity in the case of a biphoton state, first, we must introduce the Schmidt decomposition. It states that whichever joint spectral amplitude (JSA) can be written as a linear sum of products of orthonormal states for the system of the idler and the signal [133, 134]:

$$\phi(\omega_s, \omega_i) = \sum_{j=0}^{d} \sqrt{\lambda_j}\sigma_{s,j}\sigma_{i,j} \tag{4.15}$$

where the coefficients λ_j are the Schmidt coefficients and satisfy $\sum_j^d \lambda_j = 1$. $\sigma_{i(s),j}$ is the j-th orthonormal state describing the system of the idler (signal) photon. The Schmidt decomposition is a mathematical trick to express a complex biphoton wavefunction as a linear sum of components; it is possible that the components do not have any physical meaning.

The purity can also be written as $\mathcal{P} = 1/M$ [135], where M is the number of modes over which the quantum state is superimposed, and it is also called the Schmidt number.

M is defined as:

$$M = \frac{1}{\sum_{j=0}^{d} \lambda_j^2} = \frac{1}{\mathcal{P}} \tag{4.16}$$

We have found a strict link between the purity, the Schmidt number, and the JSA.

In a single-mode state, therefore, we can write $\phi(\omega_s, \omega_i) = \sqrt{\lambda}\sigma_s\sigma_i$; the JSA is separable. It means that the signal spectral distribution does not depend on the idler, and vice versa, in this case, its JSI will appear as a circle, as in Fig. 4.3a. While in a multimode state, in which the state is not separable and there are multiple non-zero λ_j, the JSI displays a squeezing, like in Fig. 4.3b. Therefore, the graphical representation of the JSI is a powerful tool to differentiate between single-mode and multimode states.

The thickness of the JSI is defined by the pump bandwidth, since given a certain idler frequency ω_i the signal must respect $\omega_s = 2\omega_p + \delta\omega_p - \omega_i$, where $\delta\omega_p$ are frequency deviations within the Lorentzian lineshape of the pump. Therefore, we can imagine that to retrieve a perfectly pure state, one must filter with a bandwidth comparable to the pump FWHM.

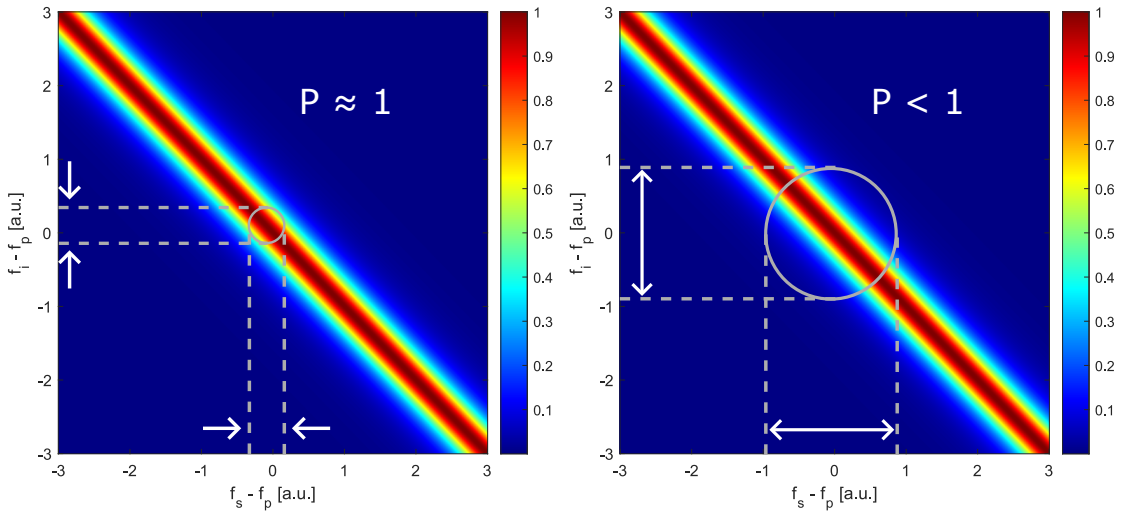

(a) The remained JSI is almost separable and $\mathcal{P} \approx 1$.

(b) The remained JSI is not separable, and spectral correlation are present within the filter bandwidth, thus $\mathcal{P} < 1$.

Figure 4.3: Qualitative example of normalized JSI, no resonator effect is considered here. The grey dashed lines represent the effect of spectral filters applied to the two photon channels, and the white arrows indicate the width of the transmitted photons' bandwidth. The grey circle represents the remaining biphoton wavefunction after filtering. On the x-axis (y-axis), we represent the distance in arbitrary units between the frequency of the signal (idler) photon and that of the pump.

In our system, the resonator resonances are not narrow enough to remove the spectral correlations among photons from the same mode. During the transition toward a stimulated process, the photons' linewidths are gradually narrowed. It can be imagined

as if the filter applied to the JSI is narrowing onto the phase-matching JSI. In summary, what we expect from the measurements is that photons have a very low purity for completely spontaneous processes. Increasing the circulating power, thus approaching the OPO threshold, photon bandwidths narrow and their purity increases. Reached the stimulated regime, the emitted photons should be in a pure state with a completely separable JSI displaying $\mathcal{P} = 1$.

Finally, the link between the autocorrelation function at zero delay, for thermal radiations, and the purity is [72, 133, 136]:

$$g^{(2)}(0) = 1 + \mathcal{P} = 1 + \frac{1}{M} \tag{4.17}$$

4.1.2 Results

We performed the measurements by pumping the microring at $\sim 16\,\mathrm{dBm}$ and counting the number of photons hitting the detectors at different time delays. The measured quantity is not actually the $g^{(2)}(\tau)$, but it is proportional to it. Therefore, we fit the coincidences using the function:

$$f = b + ae^{-\frac{2|\tau - \tau_0|}{\tau_c}} = bg^{(2)}(\tau) \tag{4.18}$$

where the purity can be retrieved as $P = a/b$. In Fig. 4.4, we show two examples of autocorrelation measurement on two of the resonance modes. Note that the coincidence peak is not centered exactly at zero delay; this effect is due to the different lengths of the fibers used to take the photons from the BS to the SNSPDs, otherwise it would be centered at the origin. Blue data points correctly align with the theoretical curve, effectively showing that every mode of the microresonator behaves as a single thermal source of photons.

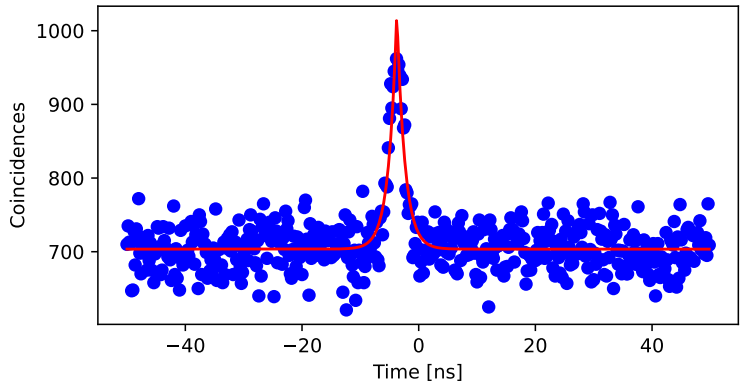

(a) Mode 7. Fit parameters are $\tau_c = 2.91(14)\,\text{ns}$, $\tau_0 = -3.69(3)\,\text{ns}$, $a = 6.4(2) \times 10^2$ and $b = 1.3947(19) \times 10^3$, which return a purity of 0.460(15).

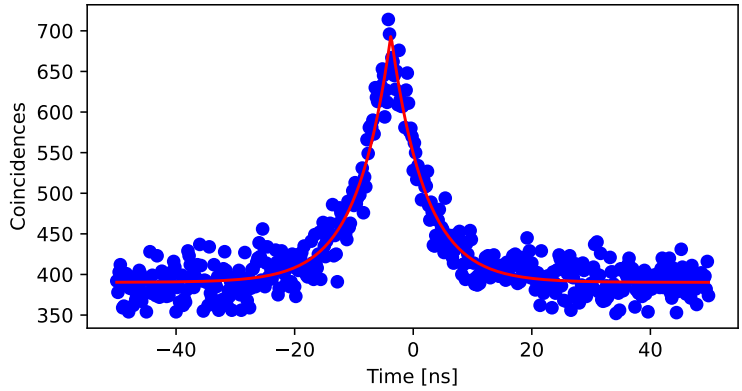

(b) Mode 11. Fit parameters are $\tau_c = 11.5(3)\,\text{ns}$, $\tau_0 = -3.76(7)\,\text{ns}$, $a = 3.05(5) \times 10^2$ and $b = 3.903(12) \times 10^2$, which return a purity of 0.781(13)

Figure 4.4: Examples of autocorrelation measurements. In blue, the data points, in red, the fit curve obtained using Eq. (4.18).

We performed the measurement on the modes: ±11, ±9, ±7, ±5, ±2, +8, and +10. We measured the coherence time of the photons and their purity in each resonance. Most of the resonances chosen are symmetrical with respect to mode 0; this choice was made to be able to make comparisons with the results of Sec. 4.2. All of the uncertainty of the results shown in the next figures is obtained from the fitting algorithm used in Python.

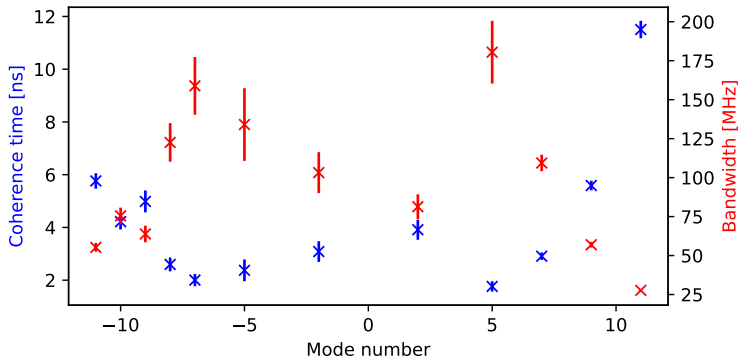

Figure 4.5: Coherence time and bandwidth measured as a function of the mode index. In blue, the coherence time. In red, the bandwidth of the photons.

In Fig. 4.5, we plot τ_c and $\Delta\nu_{ph} = 1/(\pi\tau_c)$ for each measured resonance. From the reported measurements, emissions far from modes ± 12 and 0 show a lower coherence time. This is because even though we are working below the OPO threshold, the stimulated process is, in part, present in modes closer to where the primary comb is more prone to arise. The latter result is congruent with the earlier statement. A clear example is the bandwidths of modes ± 11, which are three/four times narrower than that of modes ± 5.

An interesting result is the factor of ≈ 2 difference in coherence time between modes 11 and -11; it may seem a faulty measurement, but this is not the case (confirmed also in Sec. 4.2 at Fig. 4.9b) because a result like this is likely happening due to different phase-matching overlap with the resonance. A very small dispersivity of the FSR, not detectable with the simulations of the refractive index of Sec. 2.1.4, can introduce such variations.

We should note that the measured bandwidths for modes 5 and -7 are $\Delta\nu_{ph,5} = 180(20)$ MHz and $\Delta\nu_{pm,-7} = 158(19)$ MHz, which are bigger than the resonator linewidth obtained in Sec. 2.1.4. This problem can probably be traced back to a low acquisition time for the given coincidence counts; a longer acquisition would have helped the fitting function to retrieve a more correct result.

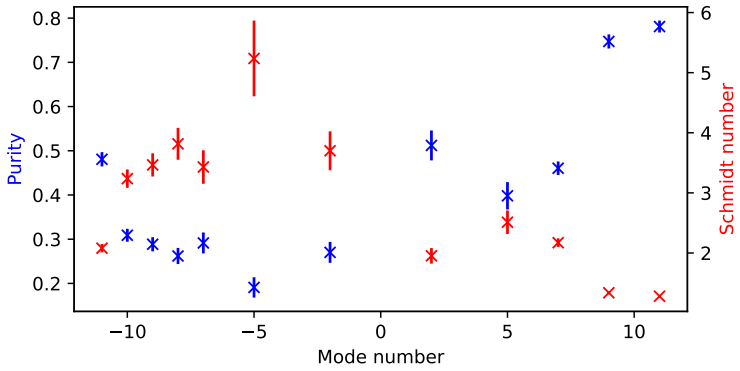

Figure 4.6: Purity and Schmidt number measured as a function of the mode index. In blue, the purity. In red, the Schmidt number.

In Fig. 4.6, the measured purity $\mathcal{P}$ and Schmidt number M are reported as a function of the resonator modes. In none mode $\mathcal{P} \approx 1$, therefore, no emission resolves a separable JSI. We can imagine that the filtering effect, which is a combination of resonator resonance linewidth, parametric gain, and dispersion, is never as narrow as the width of the FWM JSI. But, we can state with certainty that the main limitation in our results is the strong background, around 30 kHz on each single channel. With mode filtering, we can retrieve a single emission channel; however, this is not sufficient to isolate the single-mode state from environmental noise. This unwanted radiation contributes to the flat coincidence background, which covers the peak and reduces the purity.

4.2 Cross-correlation between modes

4.2.1 Theory

Pairs of photons emitted by SFWM are time-correlated, meaning they are emitted with a higher probability at the same time. This is because SFWM generates a couple of photons from the annihilation of the pump photons. Therefore, given the same optical path, it is clear that they will reach the detectors simultaneously.

In literature, it is theoretically and experimentally demonstrated that the photons emitted by degenerate SFWM (symmetric around the pump) are time-correlated [14, 107, 110, 113, 137]. Instead, above the OPO-threshold, the correlations exist among all the modes, since non-degenerate SFWM and stimulated FWM are also sustaining the photon emission [138]. Such multipartite entanglement has never been experimentally shown, due to the difficulty in recovering quantum correlations in high-intensity and coherent radiations.

Since we focused on working below threshold, we only measured correlations between symmetric modes. The time correlation between the modes was measured through the cross-correlation function, which is an extension of the autocorrelation on different modes. First, we start giving a general description of the inter-beam correlation function, which

is obtained by extending Eq. (4.1) as [126]:

$$g^{(n,m)}(t_1^{(a)}, t_2^{(a)}, ..., t_n^{(a)}, t_1^{(b)}, t_2^{(b)}, ..., t_m^{(b)}) = \frac{\langle E_a^{(-)}(t_1^{(a)})...E_a^{(-)}(t_n^{(a)})E_a^{(+)}(t_1^{(a)})...E_a^{(+)}(t_n^{(a)})E_b^{(-)}(t_1^{(b)})...E_b^{(+)}(t_m^{(b)})\rangle}{\langle E_a^{(-)}(t_1^{(a)})E_a^{(+)}(t_1^{(a)})\rangle...\langle E_a^{(-)}(t_n^{(a)})E_a^{(+)}(t_n^{(a)})\rangle...\langle E_b^{(-)}(t_m^{(b)})E_b^{(+)}(t_m^{(b)})\rangle} \tag{4.19}$$

where n and m are, respectively, the orders of the temporal correlations for the electric field of systems a and b. The cross-correlation is described by the function correlating the first-order fluctuations of the two different fields. It is obtained starting from the previous equation, and imposing $n = 1$ and $m = 1$:

$$g^{(1,1)}(t_1^{(a)}, t_1^{(b)}) = \frac{\langle E_a^{(-)}(t_1^{(a)})E_a^{(+)}(t_1^{(a)})E_b^{(-)}(t_1^{(b)})E_b^{(+)}(t_1^{(b)})\rangle}{\langle E_a^{(-)}(t_1^{(a)})E_a^{(+)}(t_1^{(a)})\rangle\langle E_b^{(-)}(t_1^{(b)})E_b^{(+)}(t_1^{(b)})\rangle} \tag{4.20}$$

Again, we can express the electric fields as a function of the creation and destruction operators:

$$g^{(1,1)}(t_1^{(a)}, t_1^{(b)}) = \frac{\langle \hat{a}^+(t_1^{(a)})\hat{a}(t_1^{(a)})\hat{b}^+(t_1^{(b)})\hat{b}(t_1^{(b)})\rangle}{\langle \hat{a}^+(t_1^{(a)})\hat{a}(t_1^{(a)})\rangle\langle \hat{b}^+(t_1^{(b)})\hat{b}(t_1^{(b)})\rangle} \tag{4.21}$$

Finally, calling $t_1^{(a)} = t$ and $t_1^{(b)} = t + \tau$, and sending the electric field E_a to detector 1 and electric field E_b to detector 2, as in Fig. 4.7, we write;

$$g^{(1,1)}(\tau) = \frac{\langle \hat{n}_1(t)\hat{n}_2(t+\tau)\rangle}{\langle \hat{n}_1(t)\rangle\langle \hat{n}_2(t+\tau)\rangle} \tag{4.22}$$

where $\hat{n}_1 = \hat{a}^+\hat{a}$ and $\hat{n}_2 = \hat{b}^+\hat{b}$. We obtained an equation identical to that of Eq. (4.5), but with a fundamental difference: the photons hitting the two detectors in this case come from different modes.

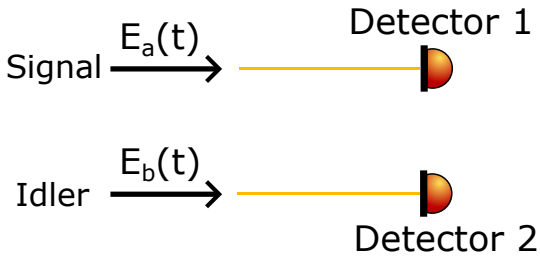

Figure 4.7: Schematic of the experimental setup used for the cross-correlation measurement.

Making an analogy with probability theory, we can link the cross-correlation to the covariance and the autocorrelation to the variance of a random variable. An important classical relationship between the variance and the covariance is the Cauchy-Schwarz inequality. We can extend this inequality also to our case, writing a relationship between autocorrelation and cross-correlation [139]:

$$(g^{(1,1)}(0))^2 \leq g_s^{(2)}(0)g_i^{(2)}(0) \tag{4.23}$$

where the subscripts $_{s,i}$ indicate signal and idler. Such inequality is violated by states of light exhibiting quantum correlations in the time degree of freedom.

We make an analogy with the autocorrelation, showing that also the biphoton spectral properties define the behavior of the $g^{(1,1)}(\tau)$. The temporal biphoton wavefunction, also called joint temporal amplitude (JTA), is strictly related to the $g^{(1,1)}(\tau)$ [140, 141]:

$$g^{(1,1)}(\tau) \propto \int_{-\infty}^{\infty} dt |JTA(t, t+\tau)|^2 \tag{4.24}$$

The $JTA(t_s, t_i)$ can be visualized as the temporal joint probability of detecting a pair of correlated photons at time t_s and t_i.

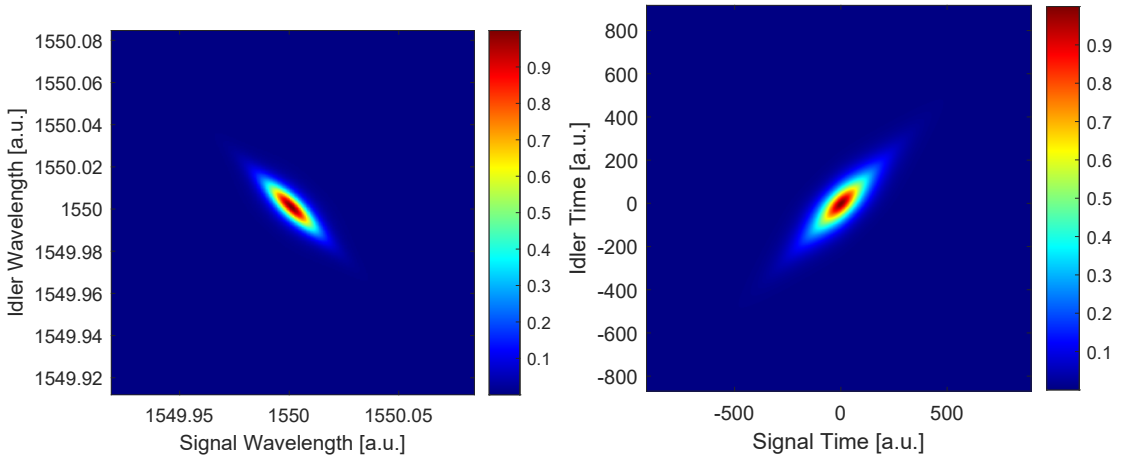

(a) Qualitative simulated JSI using SFWM conditions using a pump laser at 1550 nm.

(b) Qualitative simulation of the JTI obtained from the JSI in Fig. 4.8a.

Figure 4.8: Qualitative demonstration of the spectral and temporal correlations in the JTI and JSI of a biphoton state generated through SFWM.

It is possible to generalize the Wiener-Khintchine theorem to a biphoton state [142, 143]:

$$JSA(\omega_s, \omega_i) \propto \frac{1}{2\pi} \int_{-\infty}^{\infty} \int_{-\infty}^{\infty} dt_s dt_i JTA(t_s, t_i) e^{i\omega_s t_s + i\omega_i t_i} \tag{4.25}$$

which is the two-dimensional Fourier transform of the joint spectral amplitude.

In Fig. 4.8, we show a qualitative example of JSI and JTI simulated for a biphoton state generated through SFWM. We note how the spectral correlations, generated by the frequency and phase-matching conditions, are reflected in temporal correlations shown in the JTI, which is evidence of time and energy quantum correlations. Fig. 4.8b can be understood by imagining that the detection of a signal photon at time t_s is followed by a detection at $t_i = t_s$ of the idler photon with an almost unity probability. And the probability of receiving a signal and an idler photon separated by a time delay is almost zero. We recall that the figure shows a qualitative example and not a real simulation; in reality, the probability of detecting the counterpart photon is noticeably non-zero within a coherence time window.

Putting together Eq. (4.24) and Eq. (4.25), we understand that there is a strict link between the temporal properties of the cross-correlation and the joint spectral distribution of the signal and idler photon. In the same way, the PSD is strictly linked to the $g^{(2)}(\tau)$.

Starting from Eq. (4.24), we can now express the cross-correlation function in the case of a resonant cavity emitting time-correlated photons as [108, 144–146]:

$$g^{(1,1)}(\tau) = 1 + Ae^{-2\pi\Delta\nu_{\mathrm{ph}}|\tau|} = 1 + Ae^{-2\frac{|\tau|}{\tau_{\mathrm{c}}}} \tag{4.26}$$

where A is a multiplicative factor defining the peak height above the flat background, τ is the delay between the signal and idler detection times. In reality, signal and idler photons can exhibit different bandwidths, which is a condition that can happen for different reasons. Such as different alignment of the parametric gain with the cavity resonances or different resonator linewidths, which can be caused by dispersion or resonance splitting. Therefore, we generalize Eq. (4.26) as:

$$g^{(1,1)}(\tau) = 1 + \begin{cases} Ae^{2\pi\Delta\nu_{\mathrm{s}}\tau} = Ae^{2\frac{\tau}{\tau_{\mathrm{c,s}}}} & if\ \tau < 0 \\ Ae^{-2\pi\Delta\nu_{\mathrm{i}}\tau} = Ae^{-2\frac{\tau}{\tau_{\mathrm{c,i}}}} & if\ \tau \geq 0 \end{cases} \tag{4.27}$$

where $\Delta\nu_{\mathrm{s,i}}$ are the bandwidths of the signal and idler photons.

4.2.2 Results

This measurement was taken right after the autocorrelation one, and the ring is still pumped with $\sim$ 16 dBm. The data was taken between symmetric modes, specifically: ±11, ±9, ±7, ±5, and ±2. To fit the coincidences, the following equation was used:

$$f = b + \begin{cases} ae^{2\frac{\tau}{\tau_{\mathrm{c,s}}}} & if\ \tau < 0 \\ ae^{-2\frac{\tau}{\tau_{\mathrm{c,i}}}} & if\ \tau \geq 0 \end{cases} \quad = bg^{(1,1)}(\tau) \tag{4.28}$$

In all the measurements, in the coincidence histogram, the start click is triggered by the lower index mode, and the higher index mode triggers the stop click. Which means, for example, working with ±5, that the left side of the peak is representative of photons from mode 5 and the right side of mode -5. Therefore, using the convention of Eq. (4.28), modes > 0 are the signal and modes < 0 are the idler.

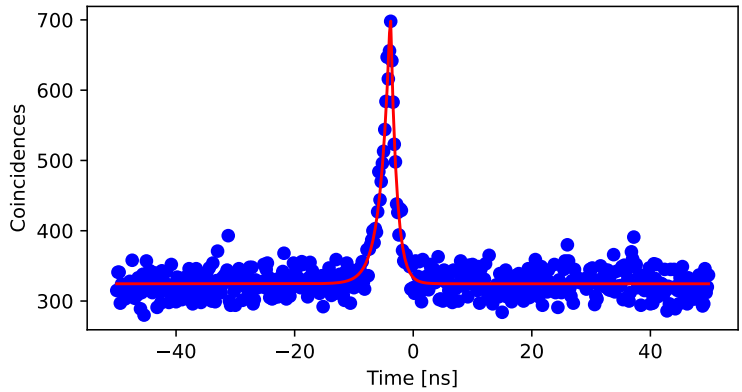

(a) Modes ± 7. Fit parameters are $\tau_{c,7} = 3.19(15)\,\text{ns}$, $\tau_{c,-7} = 2.04(11)\,\text{ns}$, $\tau_0 = -3.85(3)\,\text{ns}$, $a = 3.92(10)\times 10^2$, and $b = 3.246(8)\times 10^2$.

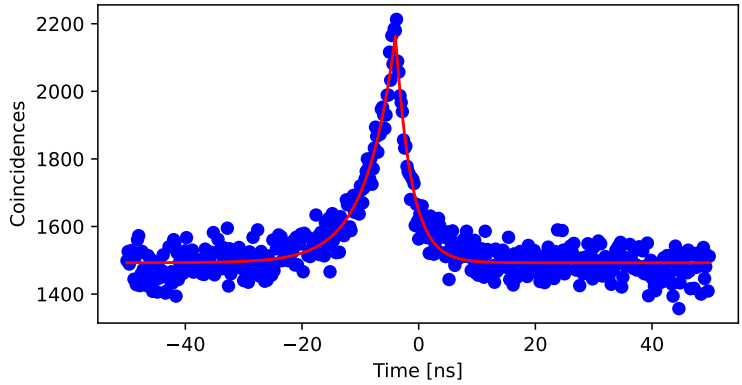

(b) Modes ± 11. Fit parameters are $\tau_{c,11} = 10.2(4)\,\text{ns}$, $\tau_{c,-11} = 5.4(3)\,\text{ns}$, $\tau_0 = -3.97(7)\,\text{ns}$, $a = 6.73(13)\times 10^2$, and $b = 1.493(2)\times 10^3$.

Figure 4.9: Cross-correlation measurements between modes ± 7 and ± 11. In blue, the data points, in red, the fit curve obtained using Eq. (4.28). Modes -7 and -11 are the start clicks, while 7 and 11 are the stop clicks.

In Fig. 4.9, we report two examples of coincidences measured between modes ± 7 and ± 11. As we can see, both plots are asymmetric, which means that the signal and idler have different bandwidths.

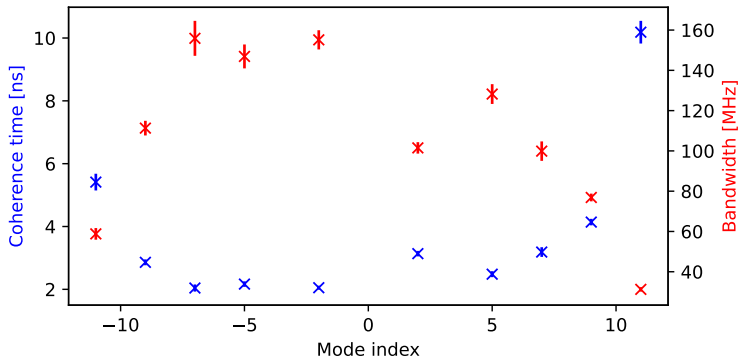

Figure 4.10: Coherence time and bandwidth measured as a function of the mode index using the cross-correlation.

Fig. 4.10 shows all the τ_c measured using the cross-correlation and the respective photon bandwidth. The behavior is similar to that found using the autocorrelation, see Fig. 4.5. We can try to check the single standard deviation compatibility between the auto and cross-correlation in estimating the photons τ_c.

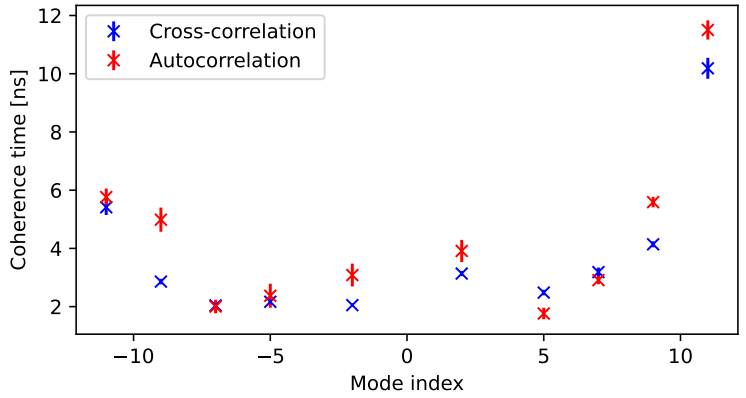

Figure 4.11: Coherence time as a function of the mode index. In red, values are obtained through the autocorrelation. In blue, values are obtained with the cross-correlation.

The comparison between the two measurements is shown in Fig. 4.11, where we find very good repetition of the qualitative behavior of the two curves. Compatibility of the measurements is found only for modes -11, -7, -5, and 7, but all the other results are really close to their respective counterpart. The non-compatibility of some of the measurements can be traced back to misalignments of the microchip, which reduces the input power. Lower circulating power means broader bandwidths of the emitted photons. The cross-correlation measurement was taken right after the autocorrelation one; in fact, the cross-correlation data points are almost always below the autocorrelation ones. One last limiting factor could be a short acquisition time; accumulating more coincidences for both the measurement types could help improve the compatibility.

Now, we can demonstrate the temporal correlations between the photons of modes ±2, ±5, ±7, ±9, and ±11 violating the Cauchy-Schwarz inequality of Eq. (4.23). Starting from the fit equation Eq. (4.28), we obtain $g^{(1,1)}(0) = 1 + a/b$ and from the purity measurements of Fig. 4.6 we get $g^{(2)}(0) = 1 + \mathcal{P}$.

Modes	$g_s^{(2)}(0)$	$g_i^{(2)}(0)$	$g^{(1,1)}(0)$	$(g^{(1,1)}(0))^2 \leq g_s^{(2)}(0)g_i^{(2)}(0)$
±2	1.51(3)	1.27(2)	2.44(4)	5.95(10) ≤ 1.92(5)
±5	1.40(3)	1.19(2)	2.55(5)	6.50(13) ≤ 1.67(5)
±7	1.460(15)	1.29(2)	2.21(6)	4.88(13) ≤ 1.77(4)
±9	1.747(16)	1.289(16)	2.14(3)	4.58(6) ≤ 2.25(3)
±11	1.781(13)	1.481(16)	1.45(3)	2.10(4) ≤ 2.64(3)

Table 4.2: Table displaying the values necessary for the evaluation of Cauchy-Schwarz inequality of Eq. (4.23). Modes highlighted in yellow violate the inequality.

In Tab. 4.2, we show the violation of the Cauchy-Schwarz inequality for the 5 couples of modes. Looking at the last column, we see how the first 4 couples largely violate such inequality. Modes ±11 do not violate it. This result means that the photons emitted from mode ±11 are not temporally correlated; even though they are still emitted in simultaneous bunches, their JTA and JSA are symmetric, namely a circle. In fact, this result is reasonable considering they showed almost unitary purities, see Fig. 4.6. For all the other modes, we demonstrated the violation of the inequality; therefore, we can state that they exhibit temporal correlations, a non-symmetric JTA, and JSA.

4.3 Heralded second-order correlation

4.3.1 Theory

In this section, we demonstrate that the Si_3N_4 microring is capable of emitting single quantum states of light. As we said in Sec. 4.1, a quantum state of light is characterized by $g^{(2)}(0) < 1$. More specifically, the autocorrelation function for a non-classical state of light can be written as [72]:

$$g^{(2)}(0) = 1 - \frac{1}{\bar{n}} \tag{4.29}$$

where $\bar{n}$ is the average number of photons in the field. Therefore, to state the existence of a single photon state, one must, ideally, obtain $g^{(2)}(0) = 1 - 1/1 = 0$ [147]. In practice it is accepted a $g^{(2)}(0) < 0.5$, because if $g^{(2)}(0) = 0.5 = 1 + 1/2$, it means that there are two photons. The fact that a $g^{(2)}(0) = 0$ describes a single-photon state can be easily visualized by thinking about the experimental apparatus, Fig. 4.2. When the wavepacket reaches the BS, it is forced to go into one of the two output ports, and it cannot split, since it is a single quantum of light. Therefore, it is ideally impossible to obtain a detection coincidence between detectors 1 and 2.

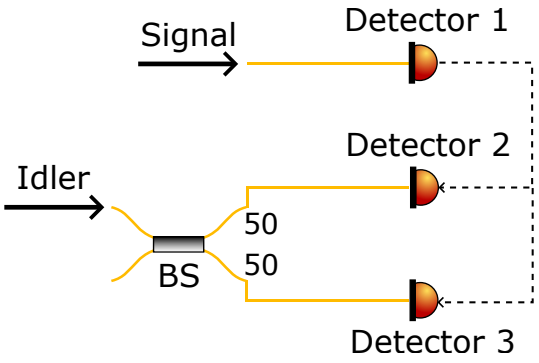

Figure 4.12: Simple schematic of the experimental setup used for the heralded second-order correlation measurement.

Since we are working with a source of entangled states of light, we must make some modifications to the experimental apparatus and measurement procedure. Measuring the autocorrelation of the signal or the idler, completely neglecting its counterpart, would return a thermal statistic as measured in Sec. 4.1. We want to measure the autocorrelation of a single photon source; therefore, we neglect the temporal statistics of the photons. To do so, we must project the entangled pair onto a single photon state. First, we simplify Eq. (3.20), assuming equal population probability of each resonance for ease of understanding:

$$|\psi\rangle = \frac{|1_{\mathrm{s},-1}1_{\mathrm{i},1}\rangle + |1_{\mathrm{s},-2}1_{\mathrm{i},2}\rangle + |1_{\mathrm{s},-3}1_{\mathrm{i},3}\rangle \ + \ ...}{\sqrt{N+1}} \tag{4.30}$$

where N is the number of pairs of resonances. Then mode filtering must be applied to reduce to the single mode state:

$$\frac{|1_{\mathrm{s},-1}1_{\mathrm{i},1}\rangle + |1_{\mathrm{s},-2}1_{\mathrm{i},2}\rangle \ + \ ...}{\sqrt{N+1}} \xrightarrow{\textit{Filter mode } j-th} |1_{\mathrm{s,j}}1_{\mathrm{i,j}}\rangle \tag{4.31}$$

Lastly, one must measure the presence of the signal (idler) photon, which acts as a herald, to project the idler (signal) onto the single photon state:

$$|1_{\mathrm{s,j}}1_{\mathrm{i,j}}\rangle \xrightarrow{\textit{Detection signal (idler)}} |1_{\mathrm{i(s),j}}\rangle \tag{4.32}$$

Now, it is possible to uncover the single-photon nature of the emitted radiation.

We introduce the heralded second-order correlation function $g_{\mathrm{h}}^{(2)}(\tau)$. It allows for measuring the autocorrelation of a single photon obtained from an entangled pair. The experimental setup used is shown in Fig. 4.12. The signal photon is detected by detector 1, which, as a consequence, projects the idler onto a single quantum state. The idler, then, enters a 50/50 BS, like in the normal autocorrelation measurement, and it is finally detected by either detector 2 or 3. The three detectors must be synchronized, since only when detector 1 clicks, the detections in the idler channel are recorded. The heralded second-order correlation function is defined as [148]:

$$g_{\mathrm{h}}^{(2)}(t_2, t_3|t_1) = \frac{\langle \hat{a}_1^+ \hat{a}_2^+ \hat{a}_3^+ \hat{a}_3 \hat{a}_2 \hat{a}_1 \rangle}{\langle \hat{a}_1^+ \hat{a}_2^+ \hat{a}_2 \hat{a}_1 \rangle \langle \hat{a}_1^+ \hat{a}_3^+ \hat{a}_3 \hat{a}_1 \rangle} \langle \hat{a}_1^+ \hat{a}_1 \rangle \tag{4.33}$$

where t_3 is the detection time of detector 3, t_2 is the detection time of detector 2, and the measurement is conditioned by an arrival on detector 1 at t_1. Typically, the measurement is prepared with the arrival time of the signal coinciding with the detection on arm 2, therefore $t = t_1 = t_2$ and $t_3 = t + \tau$. Moreover, substituting the creation and destruction operators with the number of coincidences, we obtain [13]:

$$g_{\mathrm{h}}^{(2)}(\tau) = \frac{N_{123}(\tau)}{N_{12}(t)N_{13}(\tau)} N_1(t) \tag{4.34}$$

where $N_{123}(\tau)$ are the number of threefold coincidences, $N_{12,13}$ are the number of twofold coincidences between detectors 1 and 2, and 1 and 3, and lastly, N_1 is the number of detection events on detector 1. The ideal behavior of $g_{\mathrm{h}}^{(2)}(\tau)$ measured for a single photon state is shown in Fig. 4.13.

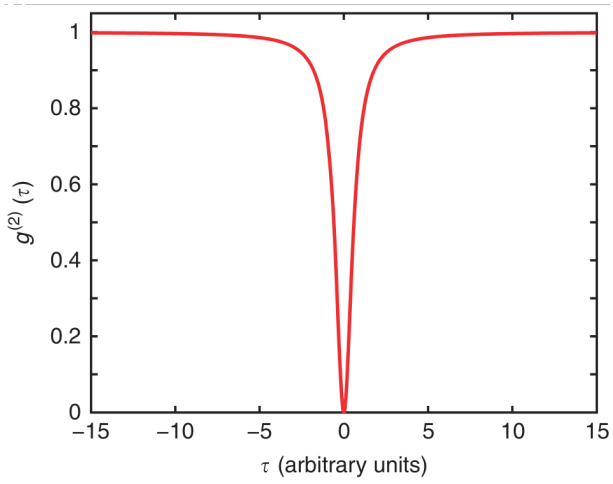

Figure 4.13: Example of ideal behavior of the $g_{\mathrm{h}}^{(2)}(\tau)$ for a single photon state. Note, the width of the dip depends on the specific process considered. Image taken from [72].

4.3.2 Results

We evaluated the $g_{\mathrm{h}}^{(2)}(0)$ using an equivalent estimator α [149–151]:

$$\alpha = \frac{P_{123}^{(\mathrm{true+bkg})}}{P_{12}^{(\mathrm{true+bkg})} P_{13}^{(\mathrm{true+bkg})}} = \frac{P_{123}}{P_{12}P_{13}} \tag{4.35}$$

where $P_{123}^{(\mathrm{true+bkg})} = N_{123}^{(\mathrm{true+bkg})}/N_1$ is the threefold coincidence probability, and $P_{12,13}^{(\mathrm{true+bkg})} = N_{12,13}^{(\mathrm{true+bkg})}/N_1$ are the two-fold coincidence probabilities. $N_{\mathrm{x}}^{(\mathrm{true+bkg})} = N_{\mathrm{x}} - N_{\mathrm{x}}^{(\mathrm{dark})}$ is the number of counts in the single channel or two-fold and three-fold coincidences, removing those generated by the dark counts, therefore only considering "true" SFWM counts and background light. N_{x} are the total coincidence counts. In this work, we assumed that the dark counts of the detectors are negligible since they are of the order of $\sim 10\,\mathrm{Hz}$,

see Sec. 2.2. This is one of the main differences with the work carried out in [151]; they did not assume the dark counts were negligible since the detectors they used were not SNSPD, but SPADs. Additionally, in the coincidence histograms, they considered a window centered around the peak as large as the optical switch itself. We do not use optical switches to control the emission, therefore we considered a window large five decay constants, hence $5\tau_{s,i,si} + 5\tau_{s,i,si}$, obtained from a fit using Eq. (4.28), centered on the peak, to consider all the correlated photons.

The calculation of N_{123} is now described. Using the software Time Tagger Lab (software necessary to interface with the Swabian time tagger), it is possible to trigger a count every time two inputs are received within the same window of arbitrary width; such a count is emitted by a "virtual channel". We created a "virtual channel" with the coincidences between detector 1 (herald) and detector 2 (one of the heralding) in a time window wide 1 ns. After that, we measured the cross-correlation between the "virtual channel" and the detection events of detector 3, making sure to use bins wide 1 ns.

$N_{12,13}$ is calculated using the usual cross-correlation measurement, again, being careful to use bins with the same width of 1 ns.

N_1 is simply measured by making a temporal trace of the detection events and then integrating it.

The experimental measurement was carried out with input power ~ 13 dBm. No precise value is reported due to the difficulty in evaluating the coupling losses, and because the ring starts misaligning after just minutes of acquisition. δ_{eff} was minimized to maximize the generation rate and reduce the acquisition time.

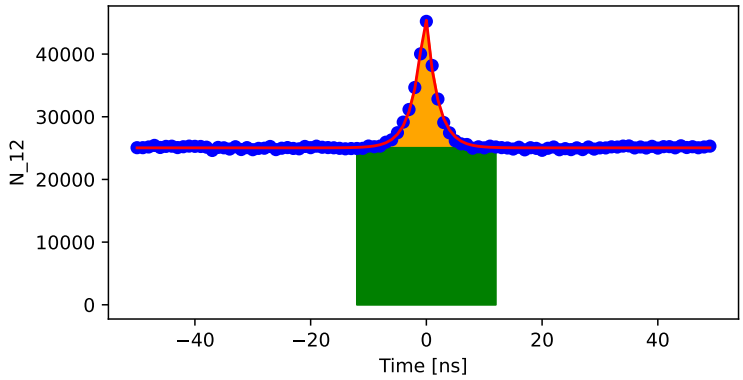

(a) Twofold coincidences N_{12} between detectors 1 and 2. From fit we obtained $\tau_s = 4.06(7)$ ns.

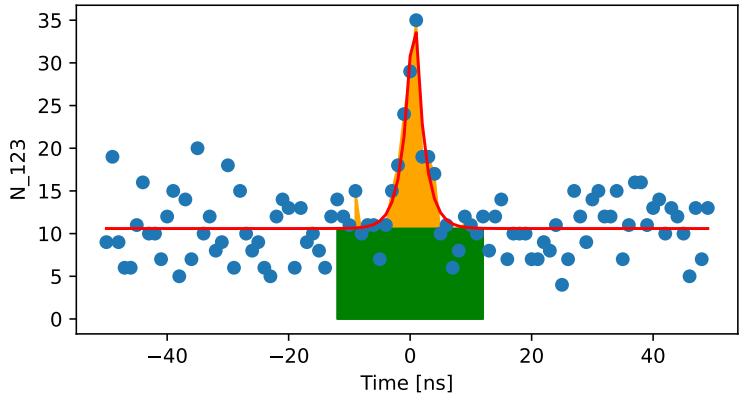

(b) Threefold coincidences N_{123} between the detectors 1, 2, and 3. From fit we obtained $\tau_{si} = 3.19(4)$ ns.

Figure 4.14: Twofold and threefold coincidences data. Coincidences between detectors 1 and 3 (idler arm) are not reported since it is similar to Fig. 4.14a. In red, the fit curves calculated using 4.28. In orange, the area where the $N_x^{(true)}$ reside and in green, the $N_x^{(bkg)}$ counts. The width of the green and orange areas is $5\tau_{s,i,si} + 5\tau_{s,i,si}$.

We obtained a $g_h^{(2)}(0) = \alpha = 0.113(10)$, which is compatible with the single photon condition. To evaluate the uncertainty, we followed the following steps:

- Evaluation of fit uncertainty on the decay constants $\delta\tau_{s,i,si}$ using Python.
- Estimation of the weight of the uncertainty of $\tau_{s,i,si}$ on the number of counts as:

$$K_{\tau_{s,i,si}} = 10(a + c)/bin\_width \tag{4.36}$$

  where a and c are evaluated from the fit of Eq. (4.28). This formula was chosen since it represents, in a conservative way, the number of additional counts that would be considered if the decay constant were one bin_width bigger; the factor 10 is added since we are summing over a window large ten decay constants.

- Estimation of the uncertainty on the photon counts as:

$$\delta N_{12,13,123} = \sqrt{m + (K_{\tau_{s,i,si}} \delta\tau_{s,i,si})^2} \tag{4.37}$$

  where m is the number of bins over which the integration window spans. The addition of m is trivial if we consider the counts $N = \sum_{n=1}^{m} x_n$, where x_n is the value of a single bin with $\delta x_n = 1$.

- The uncertainty on N_1 was calculated with Eq. (4.37) without the contribution of the decay constants.

- Lastly, the uncertainty on the heralded second-order correlation function was evaluated using the uncertainty propagation law:

$$\delta g_h^{(2)}(0) = g_h^{(2)}(0) \sqrt{(\frac{\delta N_{12}}{N_{12}})^2 + (\frac{\delta N_{13}}{N_{13}})^2 + (\frac{\delta N_{123}}{N_{123}})^2 + (\frac{\delta N_1}{N_1})^2} \tag{4.38}$$

Using Eq. (4.29), it is possible to estimate the average number of photons in the detected radiation as $\bar{n} = 1/(1 - g_h^{(2)}(0)) = 1.127(13)$. This result is compatible within one standard deviation of the mean with a single photon state, since it is incompatible with a multiple photon state ($\bar{n} \geq 2$). It is not unity; this happens since the source is not a perfect single photon emitter, and also, the presence of background radiation degrades such a value.

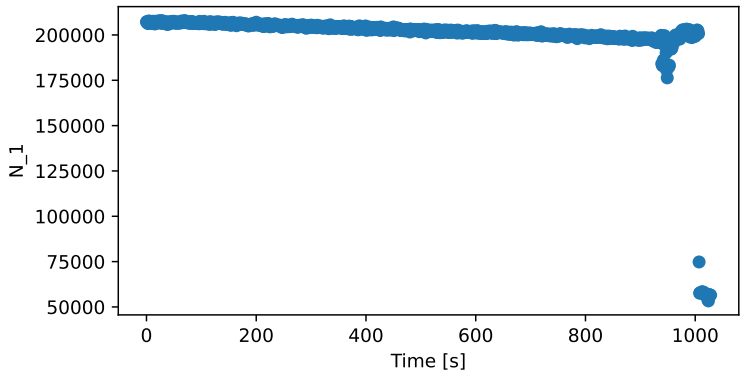

Figure 4.15: Time trace of the single counts reaching detector 1, therefore the herald photon. Note how the counts are slowly decreasing in time; this is a symptom of gradual misalignment of the microchip. At the end, due to misalignment, the comb is lost completely, and no generation of entangled pairs is present.

Such a result is one or two orders of magnitude bigger than the recent measurements in literature [107] (2024) and [152] (2022), but it is compatible with older articles [108] (2014). To obtain a lower $g_h^{(2)}(0)$, we would have had to work at lower pump powers, since the quality of the heralded second-order correlation at zero delay degrades increasing the pump [113, 152, 153]. But, we could not manage to lower the pump power below the

$\sim$ 13 dBm due to the misalignment of the ring with the lensed tapered fibers. Lower power means lower generation rate; therefore, a bigger acquisition time is required. But the ring we worked on was not perfectly controlled in temperature; these temperature changes would modify the chip alignment with the fibers due to thermal expansion and shrinkage. Thus, we could not work for an extended period of time. In Fig. 4.15, we show the temporal trace of the counts of the herald photon measured by detector 1. From the start, the counts are slowly decreasing; this is a symptom of the slow but continuous misalignment of the chip. As we can see, at the end of the acquisition window, the counts are lost, which obligated us to stop the measurement. This final and sharp count loss is due to the blue shift of the resonance, which "jumps" the pump, thus losing the generation. It happens when the circulating power is not enough to maintain a strong enough Kerr effect to keep the resonance red-shifted in the laser position. In addition, the acquisition time depends on the CAR of the source-setup system; a high CAR means that most of the photons have an entangled counterpart, which allows for a quicker accumulation of the coincidence peaks.

4.4 Two-photon interference and demonstration of time-energy entanglement

4.4.1 Theory

In this section, we will describe an alternative approach to demonstrate the quantum nature of the emitted photon pair and the non-local correlation that exists between the photons. Moreover, this measurement allows us to demonstrate the presence of entanglement in the time and energy degrees of freedom. To do so, we make use of what is called a single-path Franson interferometer [152, 154]. It is based on the work done by J.D. Franson in 1989 [155], in which he devised a way to create and demonstrate time-energy entanglement. His idea is based on systems where the emission time of a two-particle state is uncertain, but simultaneous (or nearly so), such as a three-level atom (his example) or a nonlinear crystal. He demonstrated that starting from a biparticle state of the type:

$$|\psi\rangle = |1_s 1_i\rangle \tag{4.39}$$

where we considered two photons, signal and idler, to keep coherence within the thesis. It is possible to produce time correlations, which are also reflected in the frequency domain.

Eq. (4.39) is a factorized state; in fact, it is possible to separate the component describing the two systems as $|\psi\rangle = |\psi_s\rangle \otimes |\psi_i\rangle$, therefore it is not entangled. To obtain the non-local correlations, Franson introduced the idea of postselection, which means that only specific output states are selected, while others are discarded.

Franson interferometry works in the following way, shown in Fig. 4.16. The two photons are sent in different channels, then both go through two different unbalanced Mach-Zehnder interferometers (UMZI), which must insert a temporal delay in the photons' path T_d bigger than the coherence time. This condition is necessary to ensure that no single-photon interference is present, because our goal is to show maximal two-photon interference. Then, after the interferometer, the channels are directed onto two

single-photon detectors, and the coincidences are recorded.

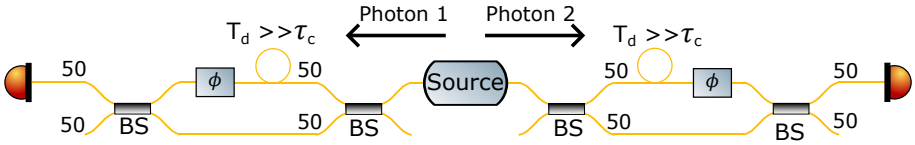

Figure 4.16: Schematic of the Franson interferometer measurement [155]. T_d is the time delay introduced by the additional fiber, and τ_c is the coherence time of the emitted photons, assuming that they are equal.

Now, we describe the behavior of the wavefunction through the Franson interferometer. We start considering the quantum state of Eq. (4.39). After the first beam-splitters, the biphoton state transforms as:

$$|1_\mathrm{s}1_\mathrm{i}\rangle \xrightarrow{BS} \frac{|1_\mathrm{s}^{(\mathrm{l})}1_\mathrm{i}^{(\mathrm{l})}\rangle + |1_\mathrm{s}^{(\mathrm{l})}1_\mathrm{i}^{(\mathrm{s})}\rangle + |1_\mathrm{s}^{(\mathrm{s})}1_\mathrm{i}^{(\mathrm{l})}\rangle + |1_\mathrm{s}^{(\mathrm{s})}1_\mathrm{i}^{(\mathrm{s})}\rangle}{2} \tag{4.40}$$

where with the superscript $|1^{(\mathrm{l,s})}\rangle$ we indicate, respectively, photons going through the longer and shorter arm of their respective interferometer. During the propagation through the UMZI, the wavefunction is changed as [156]:

$$\begin{aligned} &\frac{|1_\mathrm{s}^{(\mathrm{l})}1_\mathrm{i}^{(\mathrm{l})}\rangle + |1_\mathrm{s}^{(\mathrm{l})}1_\mathrm{i}^{(\mathrm{s})}\rangle + |1_\mathrm{s}^{(\mathrm{s})}1_\mathrm{i}^{(\mathrm{l})}\rangle + |1_\mathrm{s}^{(\mathrm{s})}1_\mathrm{i}^{(\mathrm{s})}\rangle}{2} \xrightarrow{Propagation} \\ &\frac{e^{i2\theta_\mathrm{l}}|1_\mathrm{s}^{(\mathrm{l})}1_\mathrm{i}^{(\mathrm{l})}\rangle + e^{i(\theta_\mathrm{l}+\theta_\mathrm{s})}|1_\mathrm{s}^{(\mathrm{l})}1_\mathrm{i}^{(\mathrm{s})}\rangle + e^{i(\theta_\mathrm{s}+\theta_\mathrm{l})}|1_\mathrm{s}^{(\mathrm{s})}1_\mathrm{i}^{(\mathrm{l})}\rangle + e^{i2\theta_\mathrm{s}}|1_\mathrm{s}^{(\mathrm{s})}1_\mathrm{i}^{(\mathrm{s})}\rangle}{2} \end{aligned} \tag{4.41}$$

where $\theta_\mathrm{l,s}$ are the phases acquired during the evolution in the longer and shorter arms. Now, we call $|\psi_\mathrm{i}\rangle$ the final state and can simplify it, removing the multiplicative phase components that do not modify the quantum state, obtaining:

$$|\psi_\mathrm{i}\rangle = \frac{e^{i2\theta}|1_\mathrm{s}^{(\mathrm{l})}1_\mathrm{i}^{(\mathrm{l})}\rangle + e^{i\theta}|1_\mathrm{s}^{(\mathrm{l})}1_\mathrm{i}^{(\mathrm{s})}\rangle + e^{i\theta}|1_\mathrm{s}^{(\mathrm{s})}1_\mathrm{i}^{(\mathrm{l})}\rangle + |1_\mathrm{s}^{(\mathrm{s})}1_\mathrm{i}^{(\mathrm{s})}\rangle}{2} \tag{4.42}$$

where we called the phase difference acquired in the interferometer arms $\theta = \theta_\mathrm{l} - \theta_\mathrm{s}$.

Both photons can reach the detector in two possible time bins, t and $t + T_\mathrm{d}$, independently. Therefore, in the coincidence detection, fixing one of the two photons as the *start* click and the other as the *stop* click, we obtain three different populated time delay bins. In the time delay axis (τ) we will find a peak with a width τ_c centered in $\tau = 0$, $\tau = -T_\mathrm{d}$, and $\tau = T_\mathrm{d}$. The three peaks of coincidence are populated with the following probabilities, assuming that the signal is the *start* and the idler is the *stop* of the histogram:

- Left peak centered at $\tau = -T_\mathrm{d}$:

$$\alpha_\mathrm{left} = |\langle 1_\mathrm{i}^{(\mathrm{s})}1_\mathrm{s}^{(\mathrm{l})}|\psi_\mathrm{i}\rangle|^2 = |\frac{e^{i\theta}}{2}|^2 = \frac{1}{4} \tag{4.43}$$

- Right peak centered at $\tau = T_{\mathrm{d}}$:

$$\alpha_{\mathrm{right}} = |\langle 1_{\mathrm{i}}^{(\mathrm{l})} 1_{\mathrm{s}}^{(\mathrm{s})} | \psi_{\mathrm{i}} \rangle|^2 = |\frac{e^{i\theta}}{2}|^2 = \frac{1}{4} \tag{4.44}$$

- Central peak centered at $\tau = 0$:

$$\begin{aligned} \alpha_{\mathrm{center}} =& |\frac{\langle 1_{\mathrm{i}}^{(\mathrm{s})} 1_{\mathrm{s}}^{(\mathrm{s})}| + \langle 1_{\mathrm{i}}^{(\mathrm{l})} 1_{\mathrm{s}}^{(\mathrm{l})}|}{\sqrt{2}} |\psi_{\mathrm{i}}\rangle|^2 = \\ & |\frac{e^{i2\theta}+1}{2\sqrt{2}}|^2 = |\frac{e^{i\theta}+e^{-i\theta}}{2\sqrt{2}}|^2 = \frac{\cos^2(\theta)}{2} \end{aligned} \tag{4.45}$$

Note, the dependence of α_{center} on θ means that the height of the central peak depends on the phase difference acquired in the interferometer. This dependence describes the two-photon interference. Analogously to the single-photon interference, where the wavefunction of a single photon can constructively or destructively mix after the BS due to the phase difference, here, it is the biphoton wavefunction that is interfering.

The quantum state $|\psi_{\mathrm{i}}\rangle$ does not exhibit any entanglement because it is factorizable into two states, in the signal and idler Hilbert spaces. Here, Franson introduced the postselection process. Watching the coincidence peaks center times, we can discard the states in which the photons do not reach the detectors simultaneously, and keep only those contributing to α_{center}. In this way, we are effectively performing the following:

$$\frac{e^{i2\theta}|1_{\mathrm{s}}^{(\mathrm{l})} 1_{\mathrm{i}}^{(\mathrm{l})}\rangle + e^{i\theta}|1_{\mathrm{s}}^{(\mathrm{l})} 1_{\mathrm{i}}^{(\mathrm{s})}\rangle + e^{i\theta}|1_{\mathrm{s}}^{(\mathrm{s})} 1_{\mathrm{i}}^{(\mathrm{l})}\rangle + |1_{\mathrm{s}}^{(\mathrm{s})} 1_{\mathrm{i}}^{(\mathrm{s})}\rangle}{2} \xrightarrow{PS} \frac{e^{i2\theta}|1_{\mathrm{s}}^{(\mathrm{l})} 1_{\mathrm{i}}^{(\mathrm{l})}\rangle + |1_{\mathrm{s}}^{(\mathrm{s})} 1_{\mathrm{i}}^{(\mathrm{s})}\rangle}{\sqrt{2}} \tag{4.46}$$

where we did not show the normalization of the post-selected quantum state, and PS means postselection. In this way, we have created time-energy entanglement between the two photons and a coherent superposition of $|1_{\mathrm{s}}^{(\mathrm{l})} 1_{\mathrm{i}}^{(\mathrm{l})}\rangle$ and $|1_{\mathrm{s}}^{(\mathrm{s})} 1_{\mathrm{i}}^{(\mathrm{s})}\rangle$, at the cost of discarding half the photons.

In a possible QKD setup, one can rename $|1_{\mathrm{s}}^{(\mathrm{s})}\rangle = |1_{\mathrm{Bob}}\rangle$, $|1_{\mathrm{i}}^{(\mathrm{s})}\rangle = |1_{\mathrm{Alice}}\rangle$, $|1_{\mathrm{s}}^{(\mathrm{l})}\rangle = |0_{\mathrm{Bob}}\rangle$, $|1_{\mathrm{i}}^{(\mathrm{l})}\rangle = |0_{\mathrm{Alice}}\rangle$. The final state after post-selection of Eq. (4.46) would be $|\psi_{\mathrm{QKD}}\rangle = (|0_{\mathrm{Bob}} 0_{\mathrm{Alice}}\rangle + e^{i2\theta}|1_{\mathrm{Bob}} 1_{\mathrm{Alice}}\rangle)/\sqrt{2}$, where each peer can recognize between state $|0\rangle$ and state $|1\rangle$ watching the time of arrival of the photons in singles channels. The main limitation of a QKD protocol with such a state is that there is no absolute time reference for the arrival time of the photons; therefore, it is difficult to define t and $t + T_{\mathrm{d}}$. To overcome this problem, time-bin entanglement was developed [157]. A pulsed pump on a superposition of two temporal time-bins is exploited; as a consequence, the arrival time bins t and $t+_{\mathrm{d}}$ can be directly obtained starting from the knowledge of the pump pulses.

To demonstrate that we are experimentally handling an entangled state, one must demonstrate the violation of one of the Bell inequalities [158], in our case, the CHSH inequality [159]. It can be shown that to violate the CHSH inequality in a setup like that of Fig. 4.16 with photons entangled in the energy and time degrees of freedom, one needs to analyze the behavior of the two-photon interference. It is done by monitoring

the behavior of α_{center} as a function of the phase acquired during the propagation in the interferometer. More precisely, the protocol states that if the behavior of the central peak height as a function of θ has a visibility $V > 70.7\,\%$, then we are in the presence of non-local quantum correlations [113, 154, 160, 161]. The visibility is measured as:

$$V = \frac{h_{\max} - h_{\min}}{h_{\max} + h_{\min}} \tag{4.47}$$

where $h = h(\theta)$ is the central peak height as a function of θ.

4.4.2 Results

In Fig. 4.17, we show the setup we used for the two-photon interference measurement. Light exiting from the ring and depleted of the pump passes through a single UMZI. Since the photons to perfectly interfere need to be indistinguishable, we inserted a PC in the longer arm to match the polarization of the other arm. This is necessary since the difference in fiber path rotates the polarization differently. Then, we recombine the two arms and send everything into a DWDM demultiplexer, which retrieves the two components of the biphoton state and sends each channel to an SNSPD.

Our setup differs from that of Fig. 4.16, because we used only a single UMZI. Because of this, we are not violating the locality principle, and we cannot state that we have performed a Bell violation test, even though the results are likely to be identical with the two setups. In our case, we are assuming that the spectral separation between the idler and the signal photon emitted by the microring makes them independent and pseudo-local. Other works stated to have violated the CHSH inequality using a single-path Franson interferometer [162], but to have a correct result, and, therefore, violate the locality principle, one must use two spatially separated UMZIs [163].

Since we are working with a nonlinear crystal, we need to add constraint on the value of T_{d}, which is: $T_{\text{d}} < \tau_{\text{c,p}}$ where $\tau_{\text{c,p}}$ is the coherence time of the pump. This condition is a necessary criterion to obtain two-photon interference. Given that the JSI has a width defined by the pump linewidth, the JTI width will be described by the pump coherence time; therefore, time correlations are null for $T_{\text{d}} > \tau_{\text{c,p}}$. Thus, the time delay introduced by the longer arm of the UMZI should respect:

$$\tau_{\text{c}} < T_{\text{d}} < \tau_{\text{c,p}} \tag{4.48}$$

The left inequality is necessary to ensure that the three peaks in the coincidence histogram are perfectly separable, since every peak will have a width defined by τ_{c}, and to remove any single-photon interference.

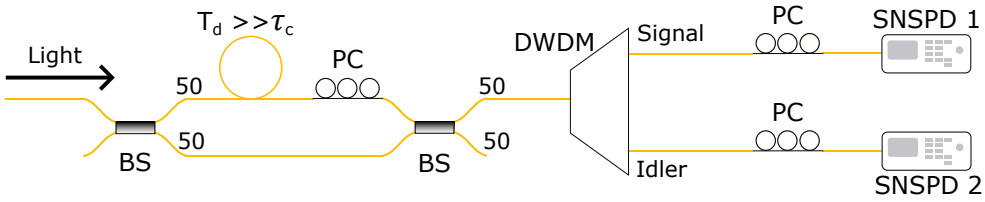

Figure 4.17: Schematic of the single-path Franson interferometric measurement. T_d is the time delay introduced by the additional fiber and τ_c is the coherence time of signal and idler.

We recorded the coincidences between the two SNSPDs and reported them in Fig. 4.18. We can clearly distinguish the three peaks. This plot helps us define the width of the coincidence window, large enough to contain the central peak, but not too much, in order to leave the sidepeaks out.

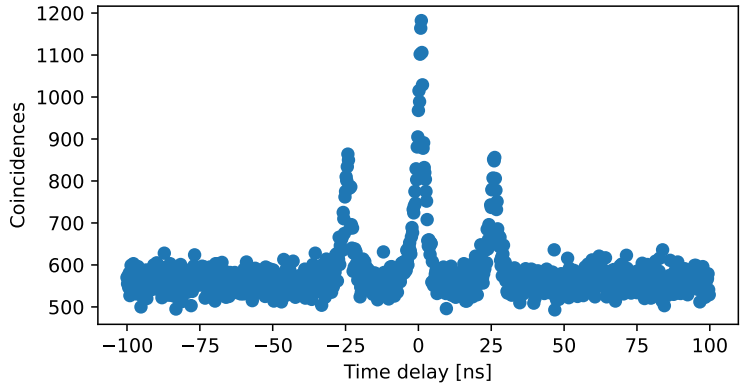

Figure 4.18: Coincidence measurement between signal and idler after their propagation through a Franson interferometer. Note, the peak distance is T_d.

In a fiber-based setup, such as ours, during the propagation, light acquires a phase, which may depend on many effects like fiber bendings, fiber temperature, fiber length, etc. Thermal fluctuations in the fiber make the main contributions to phase fluctuations; these thermal variations cause the fiber to shrink and expand due to thermal expansion. Even a stretch of tens of nm can add complete rotations of the phase. We empirically observed that just putting the hand above the fiber, without touching it, we can completely modify the interference. Therefore, it is useful to work in a temperature-controlled box to remove these thermal fluctuations.

In our laboratory, we did not have access to a temperature-controlled box. Therefore, we could not reconstruct the sinusoidal function dependent on θ; therefore, we analyzed the interference fringes generated by the thermal fluctuations. Fluctuations can also be increased by voluntarily heating the fibers, e.g., by touching them.

In Fig. 4.19, we show the effect of thermal fluctuations in the fiber on the coincidence temporal trace. The coincidences were evaluated using a window of 8 ns, since it is wide enough to contain only the central peak of Fig. 4.18. It is also important to use a time

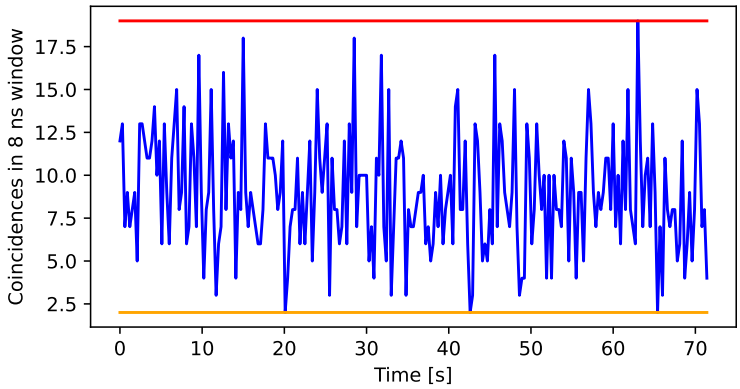

Figure 4.19: Temporal trace of the coincidences between signal and idler in a 8 ns window. In blue, the coincidences trace. In red and orange, respectively, the maximum and minimum values, that return a visibility of $V = 80.95\,\%$.

bin in the temporal trace that distinguishes thermal fluctuations but is insensitive to the chaotic statistics of the radiation. From empirical observations, we chose a time bin of 300 ms, which allows us to recognize the thermal fluctuations that are of the order of seconds.

Repeating the measurement performed in Fig. 4.19 10 times, we obtained an average visibility of $V = 84(3)\,\% >> 70.7\,\%$. Therefore, we can state that the radiation emitted from the Kerr resonator exhibits a quantum nature, and it shows non-classical time correlation between the two particles.

In the latest experiments in literature, they achieve visibilities $> 95\,\%$ [107, 110, 113, 152]. To achieve such a result, it is necessary to achieve a high degree of indistinguishability between the photons. To destructively or constructively interfere, they must be identical. Phase fluctuation, polarization mismatch, and background photons are all causes of imperfect interference. Sensible improvements can be achieved by inserting the setup in a temperature-controlled environment, as already said. In addition, it is possible to phase lock one arm of the interferometer with respect to the other, thereby reducing higher-order fluctuations that are not removed by a controlled environment. Moreover, to precisely control the polarization, it can be useful to work with polarization-maintaining components (beam-splitters and fibers). They are optical components that transmit only a specific polarization, but are capable of keeping it constant during propagation, even if stressed, bent, or heated.

Again, we stress that the latter is not a loophole-free violation of the Bell inequality, but we still have two loopholes to solve; we have demonstrated time-energy entanglement under the assumptions that the spectral separation and the post-selection still violate the locality and realism principles. The locality loophole can be solved simply by implementing the setup devised by Franson [152, 155, 161, 163]. Second, the postselection loophole (PSL) is also something that needs to be solved, since it has been shown that the PSL can allow for a hidden variable theory to describe the two photons' behavior [164]. Solutions have been found to work with time-energy or time-bin entanglement without

postselection. For example, with time-bin, by inserting an additional interferometer that forces the path of the photons in the longer or shorter arm depending on the time-bin of the pump, one can remove the PSL [165].

Chapter 5

Coherence time and detuning

5.1 Introduction and motivations

In this chapter, we study how the bandwidth (inverse of coherence time) of the emitted photons changes as a function of the effective detuning δ_{eff}. This study provides a detailed characterization of the coherence of photons generated in a Kerr resonator, exploring aspects that have not been experimentally examined before, as most of the literature focuses on the dependence on input power. The behavior of spectral properties as a function of the laser frequency-bare cavity resonance distance is known and has been thoroughly treated theoretically. Experimentally, however, the transition from spontaneous four-wave mixing (FWM) to stimulated FWM (or the optical parametric oscillation regime) has not yet been characterized. A key element of our approach is the ability to monitor δ_{eff} in real time, thanks to the setup developed, as described in Sec. 2.1.3.

Manipulating the circulating power, which we recall is the main factor defining the temporal and spectral properties of the quantum and classical light generated, is fundamental to governing Kerr resonators. While tuning this parameter by only modifying the pump power seems the simpler approach, it also has some hidden subtleties. In particular, when fixing a certain laser-cavity detuning but then changing the power, we inevitably modify the δ_{eff} as well. This happens because, for example, increasing the pump power will also add a red shift of the resonance because of the increased heating, which must be compensated by tuning the laser wavelength, to keep δ_{eff} fixed. A more critical condition is when lowering the power, which cools the resonator and its resonance blue shifts, going toward the laser. If the pump decrease is large enough, the blue shift could "jump" the laser, effectively losing all the generation within the resonator.

An alternative approach is, then, tuning δ_{eff} by keeping the pump power fixed. In this way, one can remain in the blue detuned region and be aware when there is the risk of getting "jumped" by the cooled resonance. As we said, tuning the circulating power with this method requires an adjustment of only the laser wavelength. Therefore, it is necessary to monitor only a single parameter and not both the laser wavelength and laser power, simplifying operations.

In the following, we show measurements of the photon's linewidth starting from the

below threshold regime, with very few counts, up until the stimulated regime. We highlight that we will measure τ_c both in the quantum and the classical case; as it is not trivial to measure the same quantity in both regimes, different techniques will be used, each well-suited to the specific case. In particular, while the bandwidth in the quantum regime is measured by the previously introduced coincidences measurements, see Sec. 4.1 and Sec. 4.2, the measurements in the classical regime are performed with the so-called "heterodyne beat".

In Fig. 5.1, we show how the heterodyne beat is exploited to measure the signal spectrum. The optical signal is mixed with a stabilized frequency comb by Menlo Systems that has a repetition rate of 250 MHz and each line has a FWHM of ~ 1 Hz. Such a comb is stabilized against an ultrastable cavity and on the optical lattice clock IT-Yb1 [166], the narrow linewidth is due to the locking on these two stable references. The output of the mixing is an RF frequency equal to the distance between the signal and the comb teeth; therefore, there exist multiple RF components. These new components are called beatnotes, and an important effect is that their lineshape is the convolution of that of the two initial signals. But, since the comb lines are way narrower than the signal, the beatnote features will be dominated by the signal lineshape. Then, given that the linespacing is 250 MHz, there will be only one beatnote below 125 MHz. Thus, after the photodetector, we inserted a 120 MHz low-pass filter to keep only the first-order beatnote. This RF signal is finally sent to an RF spectrum analyzer (FSW by Rohde & Schwarz).

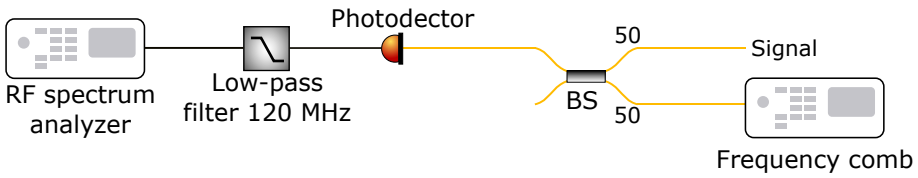

(a) Experimental setup of the heterodyne beatnote.

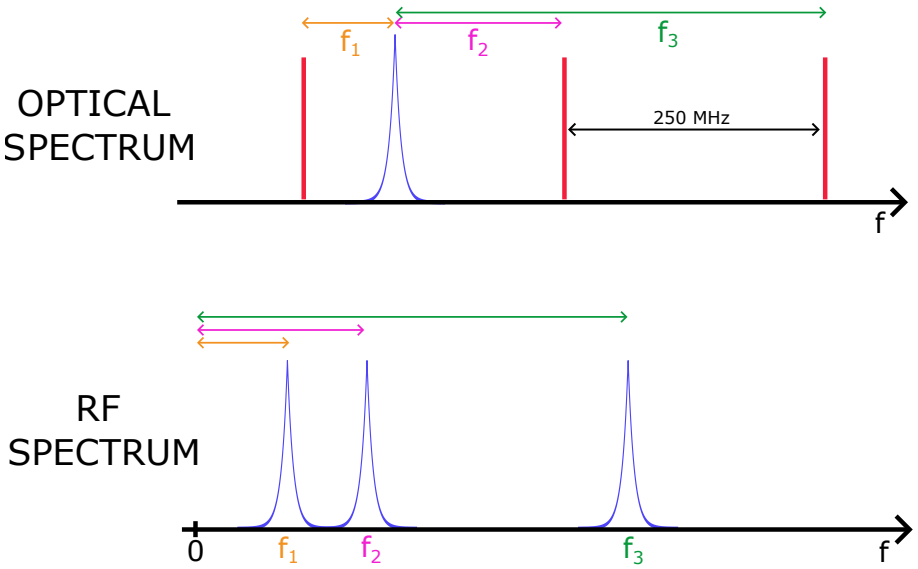

(b) Graphical representation of the working principle. In red, the frequency comb lines, in blue, the signal and the beatnotes. Note $f_1 + f_2 = 250\,\mathrm{MHz}$.

Figure 5.1: Explanation of the heterodyne beatnote measurement.

To connect the measurement of the photon linewidth in both the quantum and classical regimes and demonstrate that they return the same quantity, we use the visibility decay of a Mach–Zehnder interferometer, as described in the next subsection.

In conclusion, we mention that the content of this chapter will be part of a publication in preparation.

5.2 Interferometry: bridging quantum and classical regimes

Here, we describe how the interferometric measurement we performed works.

It consists of measuring the visibility of the single photon interference fringes observed when sending the light through an unbalanced Mach–Zehnder interferometer (UMZI). It is almost the same process as in Sec. 4.4, with the difference that here we measure the fringes in the single arm and not in the coincidences, because we are interested in single-photon interference. We show the detection stage setup in Fig. 5.2. Light emitted by the microring and filtered of the pump frequency is coupled into a DWDM demultiplexer, and with the latter, we chose the frequency mode we want to study. Then light is split in

two equal arms by a balanced BS, one of the two arms has a longer optical path, precisely of L_d. Then, light is rejoined in a single fiber by another balanced BS. Afterward, a VOA is used to control the number of photons reaching the detector. In this way, with the same setup, we can work both in the quantum and classical regimes by simply modifying the attenuation on the VOA. And finally, light is coupled in an SNSPD with a proper polarization control. Note that we also inserted a PC in the longer arm of the UMZI. Its role is to align the polarization of the light between the shorter and longer arms, because light must be identical to correctly interfere.

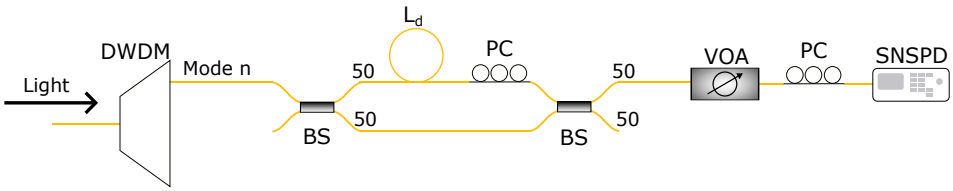

Figure 5.2: Detection stage exploited for the interferometric measurement. The VOA is necessary to reduce the radiation to the single photon level.

The behavior of the visibility as a function of the delay length gives an estimation of the coherence time. A high visibility is achieved when photons come from the same temporal mode, thus they are within the coherence time and can interfere both destructively and constructively. In contrast, ideally, zero visibility is expected when photons are independent. The ideal dependence of the visibility on L_d for a Lorenztian lineshape is [131]:

$$V = |g^{(1)}(L_d)| = e^{-\frac{|L_d|}{l_c}} \tag{5.1}$$

where $l_c = c/\tau_c$, with c the speed of light, is the coherence length.

To find a compatibility between the heterodyne beat and the correlation functions, we must obtain the same result using the interferometric approach. The interferometric measurement is powerful, since it estimates the same quantity in both regimes, simply with a few or a lot of photons. The interference fringes were measured in both cases on the SNSPD single-arm counts temporal trace.

In our experimental setup, we are not able to reproduce the perfect behavior of the visibility. For example, if there is a certain background radiation, at $L_d = 0$, it will not be possible to reproduce exactly $V = 1$, see Fig. 5.3 for an example.

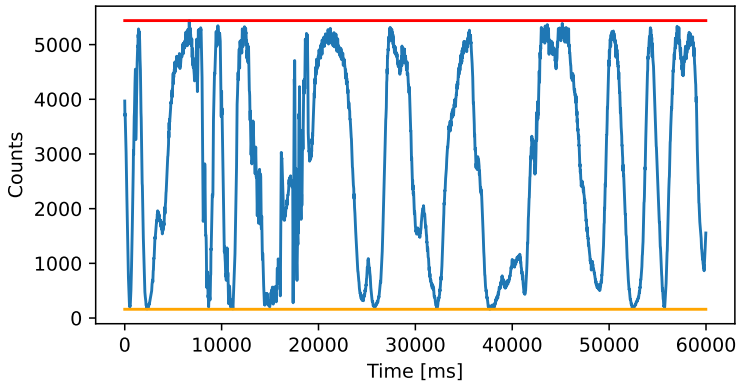

Figure 5.3: Interference fringes obtained with a delay length $L_\mathrm{d} = 0$ of mode 12. Note, the maximum is 5439 and the minimum 160, yielding a visibility of $V = 0.943$, instead of the ideal value $V = 1$.

To study the behavior of the V with different L_d, we use the fit function:

$$f = ae^{-\frac{|L_\mathrm{d}|}{l_\mathrm{c}}} + b \tag{5.2}$$

where a and b are necessary to consider the effect of background photons and other noise sources.

We started in the quantum and mostly spontaneous regime, pumping the ring at $\sim$ 16 dBm and with $\delta_\mathrm{eff} = 141.1(7)$ MHz and 148.5(10) MHz. The uncertainty on δ_eff is the uncertainty of the fit, obtained when studying the two resonance dips on the oscilloscope, see Fig. 2.7. The obtained results are shown in Fig. 5.4.

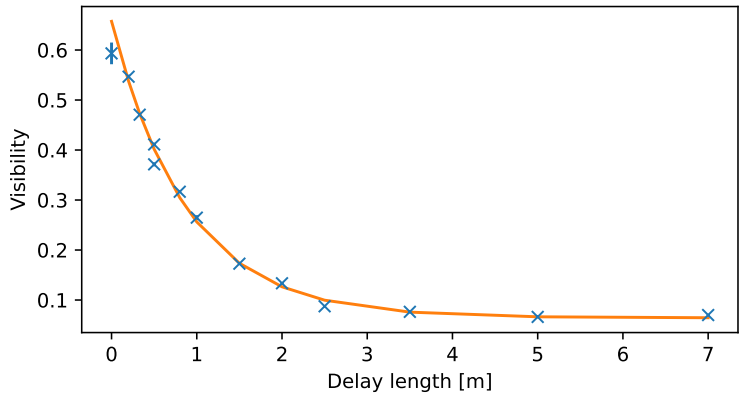

(a) $\delta_{\text{eff}} = 141.1(7)\,\text{MHz}$. Fit parameters are $a = 0.593(11)$, $b = 0.0643(9)$, and $l_c = 0.886(11)\,\text{m}$ which correspond to $\tau_c = 2.96(4)\,\text{ns}$.

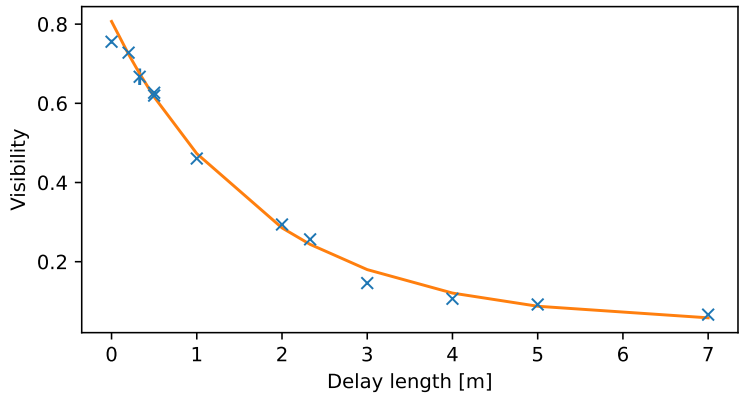

(b) $\delta_{\text{eff}} = 148.5(10)\,\text{MHz}$. Fit parameters are $a = 0.762(2)$, $b = 0.045(2)$, and $l_c = 1.735(15)\,\text{m}$ which correspond to $\tau_c = 5.79(5)\,\text{ns}$.

Figure 5.4: Visibility measure of cavity mode -12 as a function of the delay length of the unbalanced interferometer, measured in the sub-threshold regime. In blue, the data points, in orange, the fit curve obtained using Eq. (5.2).

We measured for $\delta_{\text{eff}} = 141.1(7)\,\text{MHz}$ a coherence time of $\tau_c = 2.96(4)\,\text{ns}$, which corresponds to a $\Delta\nu_{\text{ph}} = 107.5(15)\,\text{MHz}$. While at $\delta_{\text{eff}} = 148.5(10)\,\text{MHz}$ we got a coherence time of $\tau_c = 5.79(5)\,\text{ns}$, which corresponds to a $\Delta\nu_{\text{ph}} = 55.0(5)\,\text{MHz}$. From the reported results, we note how a small variation of δ_{eff} can double the coherence time. Given the difficulty in reproducing a specific value of δ_{eff}, for the coincidences approach, we measured in a range of δ_{eff} that contained the previous values as well. The results are reported in Fig. 5.5, where we show the results of Fig. 5.4a and Fig. 5.4b (interferometric measurement) with the results obtained by measuring coincidences.

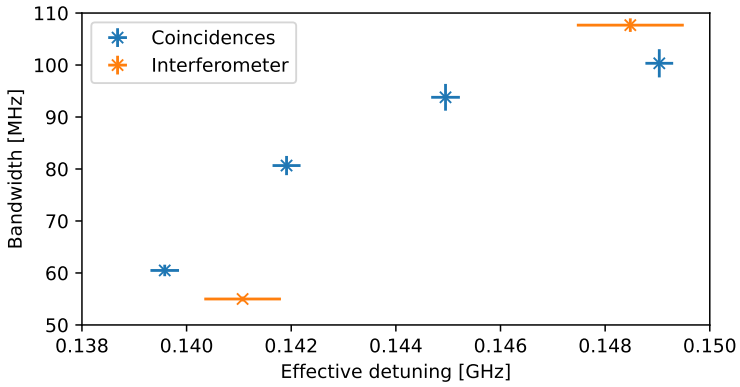

Figure 5.5: Bandwidth of the photons as a function of the effective detuning. In orange, the data points measured with the interferometric process, and in blue, the results obtained by measuring coincidences.

We can state that the results obtained with the two different measurements shown in Fig. 5.5 are qualitatively compatible. The small displacements that the interferometric measurement reports with respect to the trend of the coincidences measurement are due to the already mentioned non-idealities occurring in the system. Probably the main limitation is due to misalignments of the chip between the different acquisitions. For example, a better fiber-chip alignment in the interferometric measurement with respect to the coincidences measurement could reproduce a narrower bandwidth given the same detuning, due to a higher intracavity field. Other limitations that can introduce inaccuracies are a short acquisition time and strong background radiation.

Therefore, we have demonstrated that the coincidences and the interferometer are measuring the same quantity.

Next, we will perform the same measurement, but with classical radiation. To verify the validity of the interferometric measurement also in this regime, we measured both the pump and cavity mode -12 linewidth in the stimulated regime. No effective detuning is reported for the pump since that is unaffected by the laser-resonator alignment. During the measurement for the 12^{th} cavity mode, δ_{eff} was dynamically tuned in order to keep the generation state constant and neglect possible fluctuations in the intracavity power due to the limitations mentioned above. The results of the interferometric measurements are shown in Fig. 5.6.

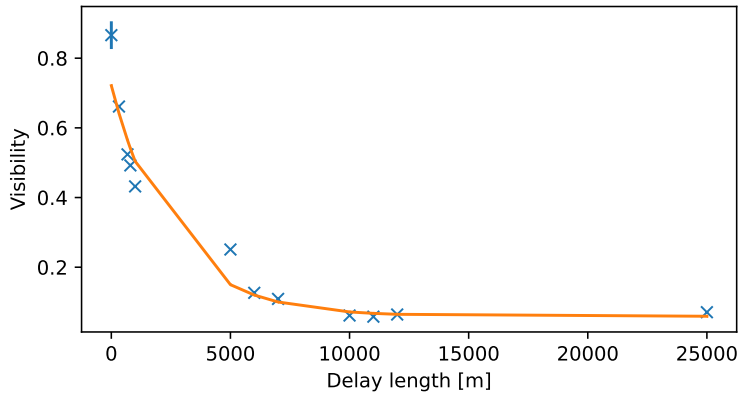

(a) Pump. Fit parameters are $a = 0.66(3)$, $b = 0.059(16)$, and $l_c = 2.5(5)\,\mathrm{km}$ which correspond to $\tau_c = 8.4(18)\,\mu\mathrm{s}$.

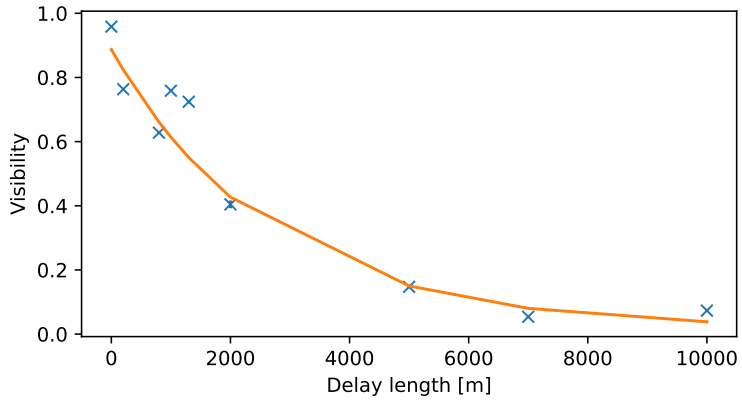

(b) Mode -12. Fit parameters are $a = 0.87(6)$, $b = 0.02(6)$, and $l_c = 2.7(9)\,\mathrm{km}$ which correspond to $\tau_c = 8(3)\,\mu\mathrm{s}$.

Figure 5.6: Visibility measured for the pump laser and the mode -12 of the cavity, as a function of the delay length of the unbalanced interferometer. The measurement for the cavity mode is performed in the above-threshold regime. In blue, the data points, in orange, the fit curve obtained using Eq. (5.2).

The obtained coherence time, for the pump and mode -12 respectively, is $8.4(18)\,\mu\mathrm{s}$ and $8(3)\,\mu\mathrm{s}$, corresponding to $\Delta\nu_{\mathrm{ph}} = 38(8)\,\mathrm{kHz}$ and $36(13)\,\mathrm{kHz}$. The significant error bars are defined by the uncertainty of the fit, which struggles to converge to the optimal parameters. The first problem is definitely the small number of data points and their "bad" alignment. The latter is attributed to the difficulty in maintaining the polarization in the UMZI fixed. Thermal fluctuations induced to generate the interference fringes also modify the polarization. Moreover, in the case of mode -12, it was not easy to maintain the regime fixed over time.

We compare these results with the heterodyne beatnotes on the spectrum analyzer;

the results are shown in Fig. 5.7. The data points were fitted with a Lorentzian curve as:

$$f = \frac{A}{2\pi} \frac{\Delta\nu}{\frac{\Delta\nu^2}{4} + (x - x_0)^2} + c \tag{5.3}$$

where the height at x_0 can be obtained as $f(0) = 2A/(\Delta\nu\pi) + c$. The measured pump linewidth is $\Delta\nu = 29(2)\,\mathrm{kHz}$, while for mode -12 we find $\Delta\nu = 38.8(2)\,\mathrm{kHz}$. These values are compatible within one standard deviation with the values obtained using the interferometer.

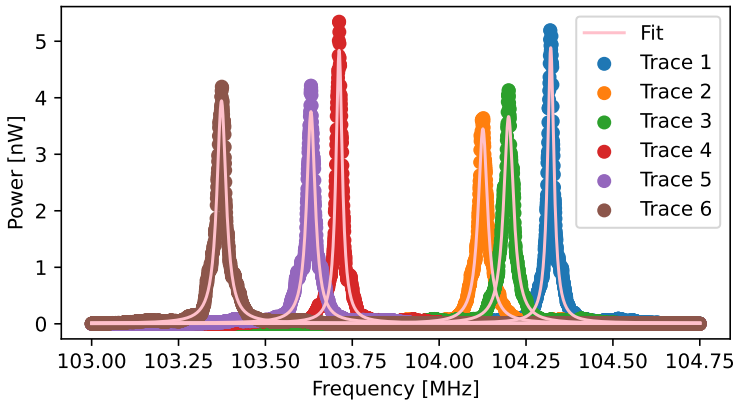

(a) Pump. Average linewidth $\Delta\nu = 29(2)\,\mathrm{kHz}$.

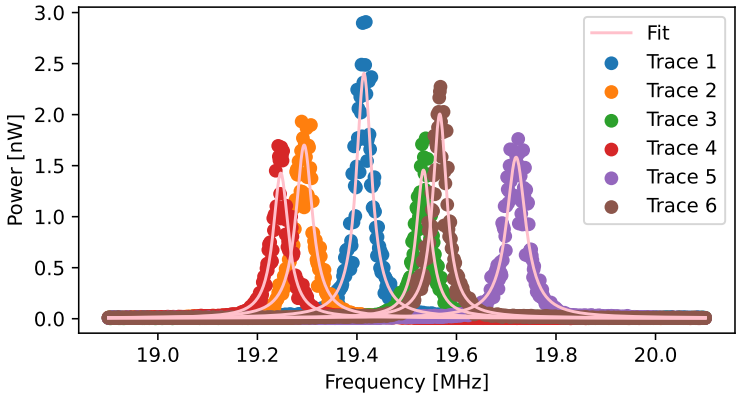

(b) Mode -12. Average linewidth $\Delta\nu = 38.8(2)\,\mathrm{kHz}$.

Figure 5.7: Six traces for the heterodyne beatnote against the Menlo frequency comb of both the pump and mode -12. The fit curve is a Lorentzian function obtained through Eq. (5.3).

So far, we have demonstrated that all our measurements evaluate the same quantities and yield compatible results. In the following, we show the linewidth behavior as a function of the effective detuning.

5.3 Coherence time as a function of the effective detuning

Now, we present the results obtained by monitoring the coherence time of mode -12 during a sweep of the pump frequency. The laser wavelength is modified by changing the temperature of the device, which modifies the laser's cavity length, thus affecting the emission frequency. We start by defining a frequency f_0, which is the point where the OPO is triggered, and the generation rate is such that the single-photon detectors cannot be used anymore, because blinded by the photon flux, see Sec. 2.2. We set the laser frequency strongly blue-detuned with respect to the resonance, and then tune the laser toward f_0, decreasing its frequency. Therefore, effectively going from a completely spontaneous and weak process toward the OPO and stimulated regime.

We measured the linewidth using the heterodyne beat method when the process was stimulated, and the single photon detectors with the coincidence measurement during the quantum regime. In Fig. 5.8, we report the results. On the x-axis, the quantity $f_\mathrm{p} - f_0$ represents the sweep of the pump frequency and not δ_eff. The fact that we can move the pump by multiple linewidths of the resonator, here $\approx 16\Delta\nu$, and still generate photons, means that the resonance is moving with us due to thermo-optic effects. It is interesting to note how we are able to tune the coherence time by three orders of magnitude by simply tuning the laser wavelength.

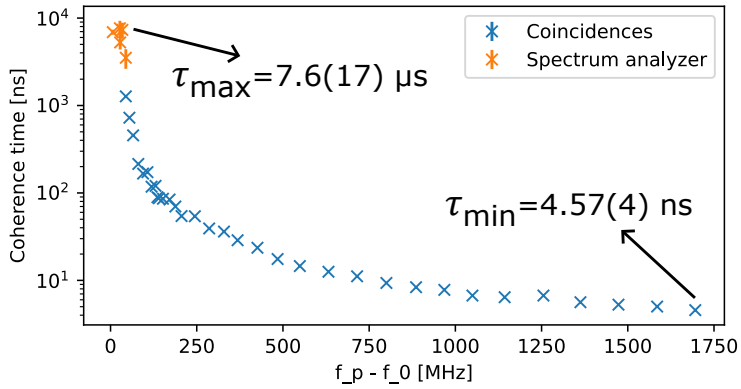

Figure 5.8: Photon's coherence time of mode 12 as a function of the frequency sweep of the pump (f_p) with respect to f_0.

Now, we show the same results but plotting $\Delta\nu_\mathrm{ph}$ instead of τ_c, because it gives a clearer idea of what relationship the emitted photons have with the pump and the resonator linewidths. The data are reported in Fig. 5.9.

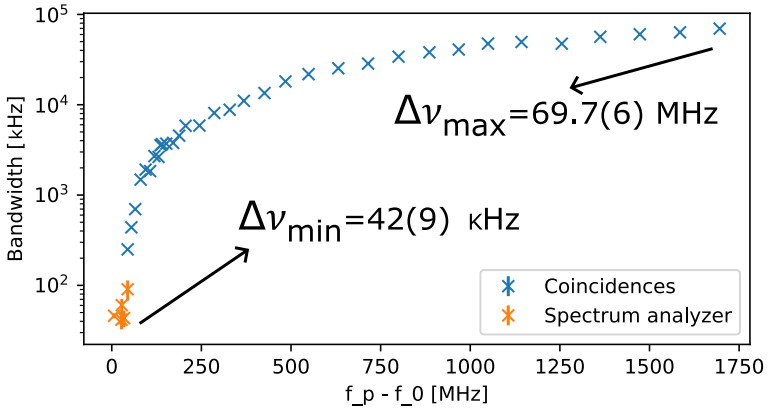

(a) Semi-logarithmic scale.

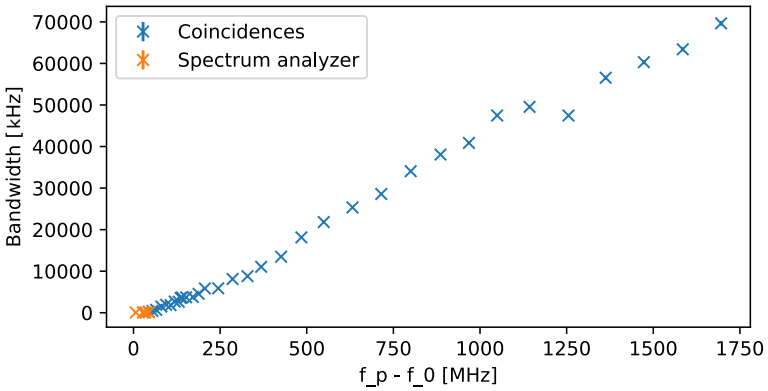

(b) Linear scale.

Figure 5.9: Photon's bandwidth of mode 12 as a function of the frequency sweep of the pump (f_p) with respect to f_0.

We note how the photon bandwidth grows, increasing the detuning between the resonator and the laser. During the stimulated process $\Delta\nu_{ph}$ is compatible with the pump's linewidth, measured around 30 kHz. Far from the OPO threshold, instead, $\Delta\nu_{ph}$ approaches the resonator linewidth. In this regime, the resonances of the microresonator effectively act as filters for the light exiting the ring. Therefore, the bandwidth of the photons cannot exceed that of the filter, unless they are modified afterward.

Moreover, in Fig. 5.9b, we note that the bandwidth scales linearly with the frequency sweeping. This could be an advantage, as a linear relationship between two basic quantities is easily exploited in a controlled and automated system.

We mention at this point that when we recorded the results reported in Fig. 5.8 and Fig. 5.9, we had not developed the δ_{eff} probing setup, yet. Therefore, we cannot report these results as a function of the effective detuning.

After developing the measurement for the effective detuning, we performed the measurements again, but only from the completely spontaneous regime until the OPO threshold is almost triggered. In fact, all the results are obtained by measuring the coincidences.

We report the results in Fig. 5.10.

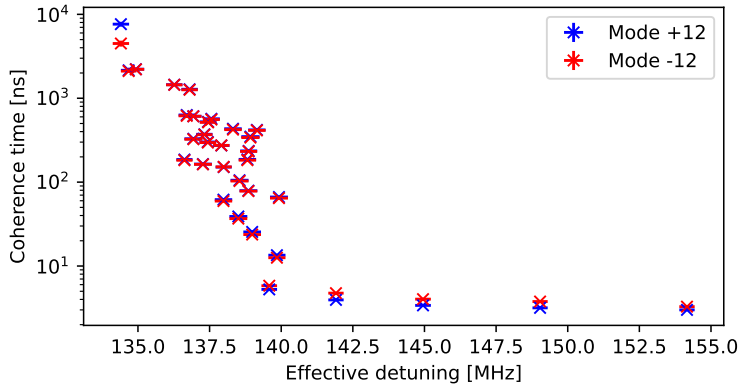

(a) Coherence time.

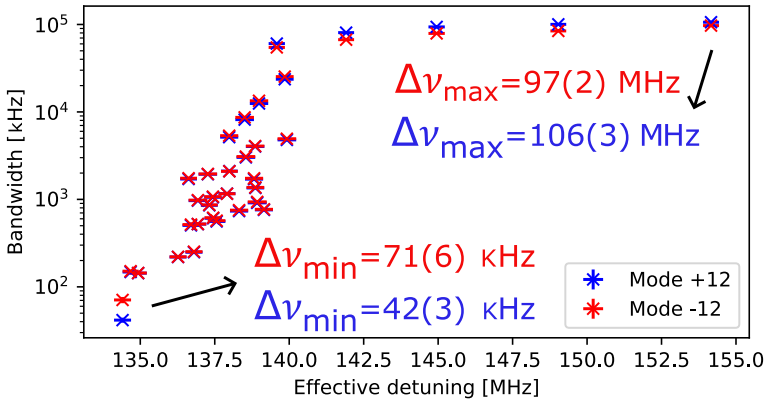

(b) Bandwidth.

Figure 5.10: Photon's bandwidth and coherence time of modes ± 12 as a function of δ_{eff}.

In these measurements, we used a longer acquisition time than in the previous measurements of Fig. 5.9 and Fig. 5.8. Therefore, we were able to accumulate enough photon counts to resolve the coincidences peak at weaker regimes. In fact, we report bandwidths of $\Delta\nu_{\text{ph}}^{(-12)} = 97(2)\,\text{MHz}$ and $\Delta\nu_{\text{ph}}^{(12)} = 106(3)\,\text{MHz}$ at $\delta_{\text{eff}} = 154.2(3)\,\text{MHz}$, which are close to the resonator linewidth. From Fig. 5.10b, we note how the minimum bandwidth measured right before the OPO threshold is comparable with those found just above threshold in Fig. 5.9.

5.4 Stimulated regime bandwidth analysis

When approaching the OPO regime, the bandwidth of the emitted photons seems to tend to that of the laser pump. To verify this hypothesis, we performed the same measurements deeply in the OPO regime for two different pump linewidths. Firstly, we use the free-running laser linewidth $\sim 30\,\text{kHz}$, and then, through a phase stabilization of the laser

or also called laser locking, we reduced its linewidth to sub-1 Hz. We performed the measurement only for a given value of δ_{eff}, because in the stimulated regime, the bandwidth seems to reach a constant value. We demonstrate this statement with the data shown in Fig. 5.11, in which we show that the bandwidth is constant above the OPO threshold as a function of the pump wavelength.

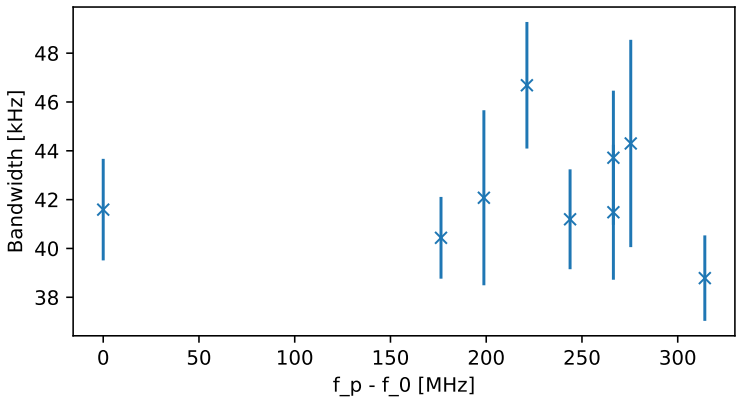

Figure 5.11: Bandwidth of photons from mode −12 as a function of the frequency sweep of the pump, measured in the stimulated regime using the heterodyne beat with the Menlo frequency comb. The x-axis presents the same quantity as Fig. 5.9 and Fig. 5.8.

In Fig. 5.12, we show the setup for locking the laser, while in Fig. 5.13, the overall measurement setup locking and measuring, to show how the locking stage is inserted in the overall experimental apparatus. To lock the laser, it is essential to have access to a stabilized frequency reference; in our case, it is the stabilized frequency comb. We do not present the comb stabilization procedure; the only important thing to keep in mind is that the frequency comb has ultra-narrow ($\Delta\nu \sim 1\,\text{Hz}$) and ultra-stable modes (no frequency drifts). We want to transfer the stability of the comb on our laser that is pumping the microring. To do so, we must create a feedback loop on the pump laser in order to compensate for all the fluctuations. We describe it in the following.

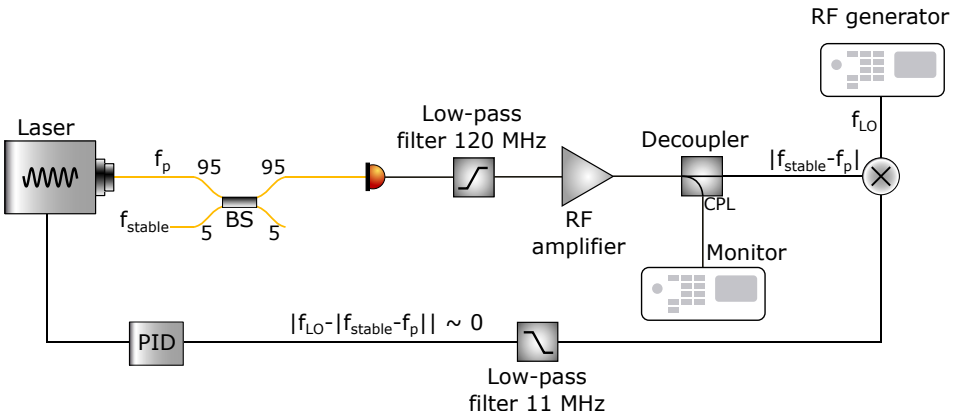

Figure 5.12: Schematic of the laser locking setup we exploited. Note that for the system to work, the condition $f_{\mathrm{LO}} \approx |f_{\mathrm{stable}} - f_{\mathrm{p}}|$ must hold. The *monitor* component can be either a spectrum analyzer, an oscilloscope, or any instrument that allows for monitoring the RF frequency at $|f_{\mathrm{stable}} - f_{\mathrm{p}}|$. *PID*: device returning an output proportional, integrative, and derivative of a given input signal, *Decoupler*: device that sends a small amount of the RF signal into a side port (CPL) and most of the signal to the main output.

We start by filtering the pump radiation from the light generated by the microring using the "common" port of the first DWDM (channel 42) filter encountered after the resonator. In this way, we send all the generated modes on the "reflect" port and keep only the pump component in the "pass" port. Then we combine, using a BS, the pump radiation with that emitted by the stabilized Menlo frequency comb, first filtered with another CH42 DWDM filter. At the BS output, we get a signal containing all the frequencies of the beatnotes between the comb components and the pump frequency. Since the frequency comb has a repetition rate of 250 MHz, we can understand which beatnote is the one between the laser and the closest comb component. The signal is then sent to a photodetector and a low-pass filter with a bandwidth of 120 MHz (ZLPF-120+ by Mini-Circuits) to keep only the beat with the closest comb line. Then the signal is sent through an RF amplifier (ZFL-500HLN+ by Mini-Circuits) and lastly to a decoupler (ZEDC-10-2B by Mini-Circuits). The latter sends a small portion of the signal in the "coupling" (CPL) port and lets all the rest through. The CPL signal is detected by an RF spectrum analyzer and is used to monitor the beatnote position and intensity. The output of the decoupler is, instead, sent to a mixer (ZFM-3+ by Mini-Circuits), which combines it with a signal generated by an RF wavefunction generator. We will call this last signal the local oscillator (LO), and the output of the mixer is the IF or the error signal. LO is set at a value ideally equal to that of the beatnote. In this way, the error signal will contain multiple frequency components, mainly: $|f_{\mathrm{LO}} - f_{\mathrm{RF}}|$ and $f_{\mathrm{LO}} + f_{\mathrm{RF}}$, where f_{RF} is the frequency of the beatnote. We want to filter only the first component to keep the lowest frequency component, which is almost-DC due to the condition $f_{\mathrm{LO}} \approx f_{\mathrm{RF}}$. To do so, we send the demodulated signal into a low-pass filter with a 11 MHz bandwidth (SLP-10.7+ by Mini-Circuits). This final error signal is sent into a Falc 110 by Toptica,

which contains an integrated PID (Proportional Integrative Derivative). A PID is a device that returns a single output signal that is proportional, integrative, and derivative with respect to the input signal, in our case, the error signal. Essentially, its response depends on the value of the input, on its slope/variation, and on its average value. The goal of the PID is to return a signal that can be used to feed back on an element, in our case, the laser current, to keep the error signal at zero. The output of the PID is connected to the laser current modulation port, and if the PID parameters are correctly set, the locking is achieved.

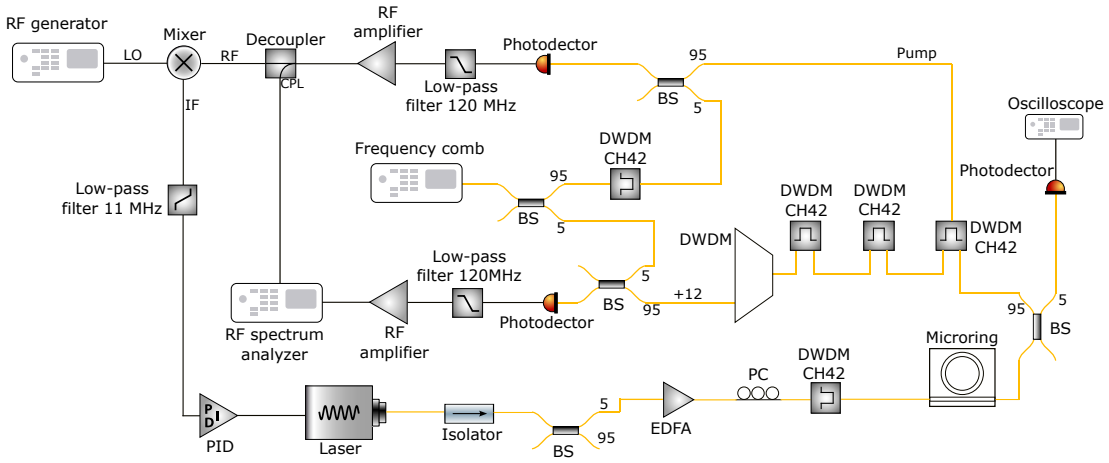

Figure 5.13: Experimental setup used for the measurement of the beatnotes with both the laser locked and unlocked.

The strength of the setup shown in Fig. 5.13 is that it can be used both for the locked and for the unlocked case. One simply needs to switch the output of the PID on or off. In Fig. 5.14, we show the beatnotes measured on the RF spectrum analyzer for a free-running laser.

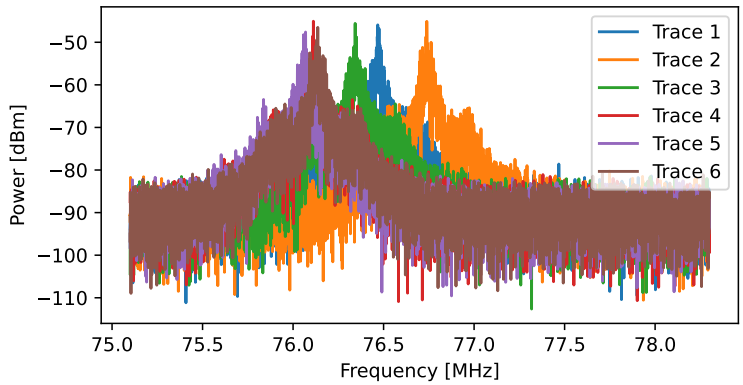

Figure 5.14: Six traces of the beatnote between the Menlo comb and the unlocked or free-running pump laser.

Each trace is taken at a different time; from the image, it is clear that the laser emission is not fixed in frequency but wanders over a range of several MHz.

Instead, in Fig. 5.15, we show the resulting beatnotes for the locked laser. We note how the laser has an ultra-narrow emission, and even using a resolution bandwidth of 1 Hz, it was not possible to resolve the emission lineshape. Moreover, the emitted frequency is not fluctuating anymore, and it is fixed in time.

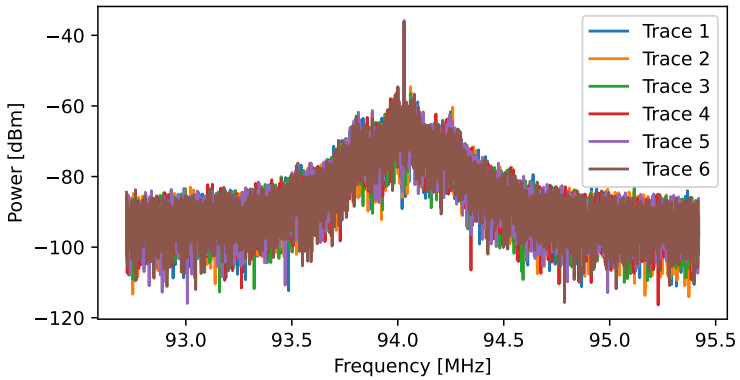

(a) 500 Hz of resolution bandwidth of the spectrum analyzer.

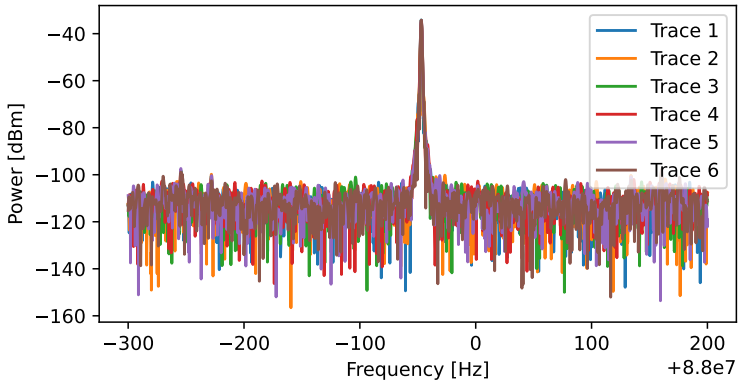

(b) 1 Hz of resolution bandwidth of the spectrum analyzer.

Figure 5.15: Six traces of the beatnotes between the Menlo comb and the locked pump laser.

We pumped the microring with ≈ 17 dBm for both linewidth conditions and measured the mode emission in the same stimulated regime. We want to demonstrate the qualitative dependence of the stimulated regime emission on the pump linewidth, without revealing or confirming a quantitative relation.

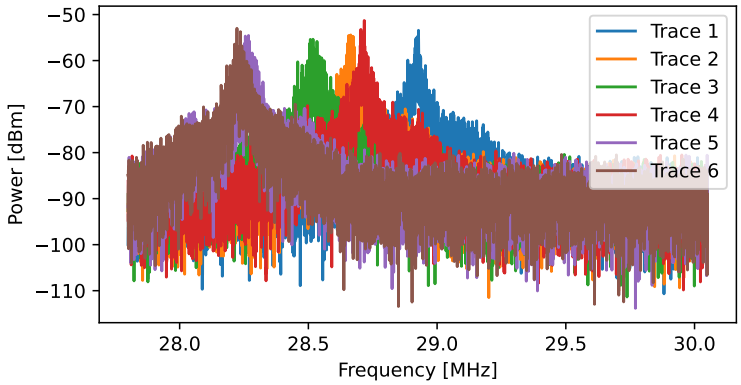

(a) With an unlocked pump.

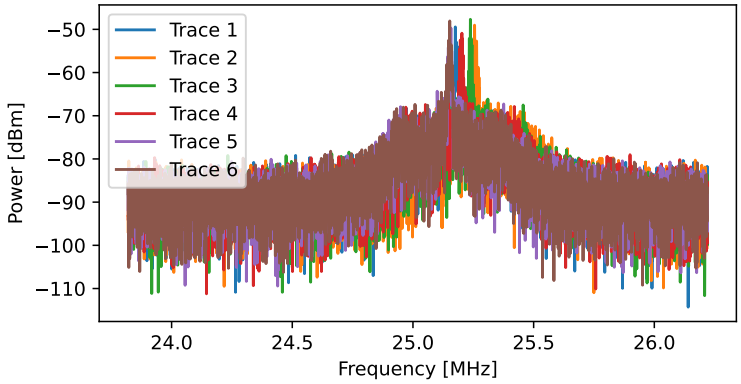

(b) With a locked pump.

Figure 5.16: Six traces of the beatnote of the mode 12 against the Menlo frequency comb.

In Fig. 5.16, we show how the generated mode (in this case, it is mode 12) inherits the properties of the pump. In Fig. 5.16a, the resonator is pumped without locking, and in fact, the emission linewidth is similar to that of the pump (tens of kHz of linewidth). Moreover, the frequency shifts are of the same order as that of the unlocked pump. Instead, in Fig. 5.16b, we clearly see a strong reduction in the linewidth with respect to the unlocked case. But it is not as narrow as the locked pump laser. Fig. 5.15a (locked pump) and Fig. 5.16b (mode 12) have both a resolution bandwidth of 500 Hz, and we can clearly see a difference in the width of the beatnote, which is larger in the output radiation. Additionally, the frequency drifts are not completely compensated, as in contrast to the pump.

Therefore, we have demonstrated how the FWM-generated modes' stability definitely depends on the pump properties. But it is not the only contribution, we can assume that the emission linewidth is also dominated by the thermal noise in the microring or other non-idealities, which increase the phase noise, broadening the line, and increasing frequency fluctuations with respect to the pump.

Chapter 6

Conclusions

In this work, we presented a complete characterization of a Kerr microring resonator used for the generation of quantum states of light, namely entangled and single photons. We presented a study that covered all the important features of a $\chi^{(3)}$ integrated quantum light source. This work is important since it allows to get an overview of the parameters and important metrics necessary to design and study such devices. Moreover, we also introduced two innovative studies, not yet present in the literature, which give researchers additional tools for the development of quantum communication applications.

The device displays a distance between the resonances of $\approx 142.65\,\mathrm{GHz}$ and can be pumped within the C-band at $\sim 1550\,\mathrm{nm}$. It is easily overlapped with DWDM technologies used in existing infrastructures, which divide the optical spectrum used for telecommunication into 100 GHz-wide channels.

Other key results we obtained are the photon-pair generation rate, which is $PGR = 316(3)\,\mathrm{kHz/mW^2}$, which means that pumping the ring with, for example, 2.5 mW, the device generates ≈ 2 million photon pairs per second. Which is a nice result when working with 10 dB to 20 dB attenuated optical links, which correspond to optical fibers of maximum 100 km. This seems a promising result, and one could imagine that increasing the pump power, the maximum distance could increase. In reality, we measured a high level of noise in the detected photon pair, which is not acceptable in a real-life environment. In addition, such noise increases with stronger pump fields. The latter is one of the main limitations in the device and setup we used in this work; the solution could be reducing the noise introduced by the pump with better filtering before and after the microring. Another possible solution, not available to us, could be the design and fabrication of a ring with better properties, such as lower losses and stronger optical field confinement.

We underlined the strong link between the temporal correlations and the spectral properties, both on the single and biphoton states. This is important since it gives strong evidence of the time-energy entanglement exhibited by these photons.

We also demonstrated that these photons exhibit an undeniable quantum nature. Their heralded second-order correlation at zero delay was evaluated to be $g_{\mathrm{h}}^{(2)}(0) = 0.113(10)$, this result is below the threshold for a single photon state of 0.5. Therefore, we confirm the possibility of using such a device as a heralded single-photon source. Additionally, we demonstrated the presence of time-energy entanglement, allowing us to

utilize this device as a compact entangled-photon source. We violated the non-loophole-free CHSH inequality, demonstrating a two-photon interference visibility of $V = 84(3)\,\%$, which is higher than the threshold $V = 70.7\,\%$ by more than four standard deviations.

With these results, we can confirm that such devices are perfect candidates for developing integrated, telecom-compatible, and narrow-band quantum light sources.

Additionally, we made two novel contributions to the research on single-photon technologies. The first is the introduction of a quantitative model describing the behavior of the detection efficiency η of Superconducting Nanowire Single Photon Detectors (SNSPDs) as a function of the light polarization. We found experimental evidence that η changes following a cosine squared law, dependent on the angle of alignment between the polarization of the photon and the nanowire direction.

The second one is the study of the SFWM photons' coherence time as a function of the operational regime. We analyzed how their bandwidth changes as a function of the distance between the pump laser and the pumped resonator's resonance. This is an innovative contribution in literature since most of the works study the properties of the emitted field as a function of the pump power circulating within the microring, which cannot be easily estimated. We provided our results as a function of a quantity that is experimentally measurable and easily controllable. This quantity, which we called effective detuning δ_{eff}, can also be controlled in a commercial setup, by simply tuning the pump laser wavelength. We demonstrated the possibility of modifying the bandwidth over three orders of magnitude, important to integrate the device with different components that may have different coherence requirements. The obtained bandwidths are also compatible with future devices needed in a fully operational quantum network, such as quantum memories [167, 168]. Most of these devices exploit atomic transitions to store qubits; therefore, their linewidths are in the MHz range [169], giving perfect overlap with our source. Moreover, this study also provides an investigation of the optical field behavior during the transition between the quantum and classical regimes. It is a major description since we are able to link the quantum and classical nature of the same phenomenon.

However, we must underline that our device requires careful temperature control (TEC) to be integrated into a real-life telecommunication channel. Ideally, the requirements are: temperature control of the whole chip and coupling system, temperature control of the environment (box, room, or laboratory in which the device is placed), and integrated temperature control to precisely tune the microring resonance. We had the first and second requirements, but lacked the last. An integrated TEC allows for a precise tuning of the resonance; in this way, one can control the effective detuning by either changing the laser wavelength or shifting the resonance. Moreover, one would be able to tune the emission frequency with a very high precision, in the order of the GHz [170]. These requirements make it difficult to deploy it in harsh environments and force careful protection of the device from strong temperature fluctuations.

In addition, the tunability of the photon's bandwidth is not free of cost, since in order to achieve it, one must modify the circulating power, which also affects the quantum nature of the emitted photons. Increasing the amount of intracavity radiation, the process diverges from a completely spontaneous phenomenon toward stimulated FWM. Additionally, a stronger circulating power means a stronger pump oscillating within the

resonator, therefore an increase in the background radiation and noise, as we already mentioned. Both these effects are detrimental for the generation of single-photon states; therefore, a higher heralded second-order correlation at the origin ($g_{\mathrm{h}}^{(2)}(0)$) is expected, which means a lower probability to effectively emit a single photon. Moreover, we showed that the non-classical correlations between the photon pairs are ruined when increasing the effect of the stimulated process. Which means a less "pure" entanglement.

Looking to the future, it would be an interesting work trying to evaluate the biphoton wavefunction or Joint Spectral Intensity (JSI) evolution during the circulating power increase. In this way, it would be possible to extract many of the measured properties, like cross-correlation and autocorrelation at the source, photon's bandwidth and purity, from just one quantity. In principle, one needs to, with a fixed photon-pair generation rate, filter separately the signal and idler channels with ultra-narrow filters and detect the number of SFWM pairs reaching the detectors. Then, plotting the number of coincidences in a two-dimensional plot, in which on the x- and y-axis there are the signal and idler filter center frequency, it is possible to reconstruct the behavior of the JSI. The main requirement is that the filters are narrow enough to resolve variation within the resonator's linewidth, which is $\approx 110\,\mathrm{MHz}$. Therefore, one would need a kHz-wide optical filter, which does not exist. Additionally, toward the OPO threshold, the bandwidth narrows to tens of kHz; therefore, the filter requirements become even more stringent. However, it is possible to resolve the JSI of a biphoton state generated by SFWM, exploiting stimulated FWM [171]. The idea is based on the discovery that the JSI between the spontaneous and stimulated effects, in second-order non-linear materials, is related [172]. Such a result was then extended to higher-order non-linearities, such as materials exhibiting FWM [171]. The stimulated FWM output signal is proportional to the spontaneous one by a factor that only depends on the stimulating power. Therefore, to exploit such a discovery, researchers can use an additional tunable laser to stimulate FWM, on top of the spontaneous process, at a specific signal (idler) frequency, and then measure the idler (signal) power. Since a laser is finely tunable and narrow relatively to an optical filter, one can reconstruct the JSI with unprecedented precision.

Another interesting achievement would be implementing an entangled photon QKD protocol, exploiting the time-energy or time-bin degree of freedom. A few works have demonstrated QKD protocols in the first [51, 173] and second [174] degrees of freedom. The latter articles present a secret key rate (SKR) of maximum $\sim 200\,\mathrm{bits/s}$ with optical link lengths of at most 25 km. These results are far from the commercial requirements necessary to transition toward an operational quantum network. The main limitations are always noise in the system, which degrades the entanglement fidelity, and losses in the system.

A further possibility could be exploiting frequency-bin entanglement, which gives the advantage of using classical RF electronics to perform quantum gates and control the qubits. Some demonstrations have been reported [170], but again, the results are not close to the real-life requirements, since the researchers presented an SKR of 4.5 bits/s over a 26 km of fiber. Frequency-bin entanglement presents additional challenges. Correctly performing quantum gates on the qubits using RF electronics requires careful control of the modulation frequencies and amplitudes. Even small deviations in these parameters

can introduce great errors and strongly limit the SKR. Therefore, more work is needed to effectively demonstrate the feasibility of implementing a quantum communication network with these devices.

Although the results presented so far prove that Kerr microresonators are excellent candidates for high-rate, integrated quantum light sources, several technological obstacles still limit their full deployment. In particular, reducing noise contributions, ensuring long-term thermal stability, and mitigating the impact of stimulated processes on the quality of the quantum state remain open challenges. Improvements in filtering stages, integrated temperature tuning, resonator design, and on-chip stabilization could significantly enhance performance without altering the fundamental operating principles of the device. Therefore, despite the remaining challenges, this work contributes substantial experimental and conceptual evidence that integrated Kerr resonators represent a realistic and versatile foundation for next-generation quantum communication systems. With further technological refinement, these devices could transit from proof-of-principle demonstrations toward deployable quantum network nodes, enabling the distribution of entanglement, secure communication, and hybrid interfacing with emerging quantum technologies.

Bibliography

[1] Muhammad Annas Khan et al. «From quantum communication fundamentals to decoherence mitigation strategies: Addressing global quantum network challenges and projected applications». In: *Heliyon* 10.14 (2024), e34331. ISSN: 2405-8440 (cit. on p. 1).

[2] *Polarization-entangled photon source*. TPS_1550_TYPE_II. Aurea technology (cit. on p. 1).

[3] *CORRELATED PHOTON PAIR SOURCES*. DTS0199. OZ Optics (cit. on p. 1).

[4] C. I. Osorio et al. «Heralded photon amplification for quantum communication». In: *Phys. Rev. A* 86 (2 Aug. 2012), p. 023815 (cit. on p. 1).

[5] Xiao-Hai Zhan et al. «Experimental demonstration of long distance quantum communication with independent heralded single photon sources». In: *npj Quantum Information* 11 (May 2025) (cit. on p. 1).

[6] Xiao-Hai Zhan et al. «Quantum Key Distribution with a Continuous-Wave-Pumped Spontaneous-Parametric-Down-Conversion Heralded Single-Photon Source». In: *Phys. Rev. Appl.* 19 (3 Mar. 2023), p. 034027 (cit. on p. 1).

[7] G. Paganini et al. «High-quality entangled photon source by symmetric beam displacement design». In: *APL Photonics* 10.3 (Mar. 2025), p. 031302. ISSN: 2378-0967 (cit. on p. 1).

[8] Brianna Farella et al. «Spectral characterization of an SPDC source with a fast broadband spectrometer». In: *AIP Advances* 14.4 (Apr. 2024), p. 045034. ISSN: 2158-3226 (cit. on p. 1).

[9] Xucheng Zhang et al. «Advances in resonator-based Kerr frequency combs with high conversion efficiencies». In: *npj Nanophotonics* 1.1 (2024), p. 26 (cit. on p. 1).

[10] Nianqin Li et al. «Platform for designing bipartite entangled quantum frequency combs based on silicon nitride microring resonators». In: *Phys. Rev. Appl.* 21 (5 May 2024), p. 054058 (cit. on p. 1).

[11] C. Lecaplain et al. «Quantum cascade laser Kerr frequency comb». In: *2015 European Conference on Lasers and Electro-Optics - European Quantum Electronics Conference*. Optica Publishing Group, 2015 (cit. on p. 1).

[12] Andre Kovach et al. «Emerging material systems for integrated optical Kerr frequency combs». In: *Adv. Opt. Photon.* 12.1 (Mar. 2020), pp. 135–222 (cit. on p. 1).

[13] S. Signorini and L. Pavesi. «On-chip heralded single photon sources». In: *AVS Quantum Science* 2.4 (Oct. 2020), p. 041701. ISSN: 2639-0213 (cit. on pp. 1, 50, 51, 59, 78).

[14] Lucia Caspani et al. «Multifrequency sources of quantum correlated photon pairs on-chip: a path toward integrated Quantum Frequency Combs». In: *Nanophotonics* 5.2 (2016), pp. 351–362 (cit. on pp. 1, 70).

[15] Muhammad Annas Khan et al. «From quantum communication fundamentals to decoherence mitigation strategies: Addressing global quantum network challenges and projected applications». In: *Heliyon* 10.14 (2024), e34331. ISSN: 2405-8440 (cit. on p. 1).

[16] «Nonlinear Optics». In: *Fundamentals of Photonics*. John Wiley & Sons, Ltd, 1991. Chap. 19, pp. 737–798. ISBN: 9780471213741 (cit. on pp. 1, 36, 37).

[17] Robert W. Boyd. «Chapter 1 - The Nonlinear Optical Susceptibility». In: *Nonlinear Optics (Fourth Edition)*. Ed. by Robert W. Boyd. Fourth Edition. Academic Press, 2020, pp. 1–64. ISBN: 978-0-12-811002-7 (cit. on pp. 1, 36).

[18] Zhichao Ye et al. «Low-loss high-Q silicon-rich silicon nitride microresonators for Kerr nonlinear optics». In: *Opt. Lett.* 44.13 (July 2019), pp. 3326–3329 (cit. on p. 2).

[19] S. Clemmen et al. «Continuous wave photon pair generation in silicon-on-insulator waveguides and ring resonators». In: *Opt. Express* 17.19 (Sept. 2009), pp. 16558–16570 (cit. on p. 2).

[20] David Moss, Alexander Gaeta, and Michal Lipson. «New CMOS-compatible platforms based on silicon nitride and Hydex for nonlinear optics». In: *Nature Photonics* 7 (July 2013), pp. 597–607 (cit. on p. 2).

[21] Yanne K. Chembo. «Quantum dynamics of Kerr optical frequency combs below and above threshold: Spontaneous four-wave mixing, entanglement, and squeezed states of light». In: *Phys. Rev. A* 93 (3 Mar. 2016), p. 033820 (cit. on pp. 2, 18, 39, 43, 45).

[22] A. Einstein, B. Podolsky, and N. Rosen. «Can Quantum-Mechanical Description of Physical Reality Be Considered Complete?» In: *Phys. Rev.* 47 (10 May 1935), pp. 777–780 (cit. on p. 2).

[23] Marissa Giustina et al. «Significant-Loophole-Free Test of Bell's Theorem with Entangled Photons». In: *Phys. Rev. Lett.* 115 (25 Dec. 2015), p. 250401 (cit. on p. 2).

[24] B. Hensen et al. «Loophole-free Bell inequality violation using electron spins separated by 1.3 kilometres». In: *Nature (London)* 526.7575 (2015), pp. 682–686. ISSN: 0028-0836 (cit. on p. 2).

[25] Quantum Economic Development Consortium (QED-C). *Single-photon measurement infrastructure for quantum applications (SPMIQA): Needs and priorities*. Tech. rep. Arlington, VA: SRI International, July 2022 (cit. on p. 2).

[26] Christopher Chunnilall et al. «Metrology of single-photon sources and detectors: A review». In: *Optical Engineering* 53 (Aug. 2014), p. 081910 (cit. on p. 2).

[27] Joshua Bienfang et al. *Single-photon Sources and Detectors Dictionary*. en. Sept. 2023 (cit. on pp. 2, 3, 25, 26).

[28] Naeem Akhtar et al. «Enhancement in the temperature sensing of a reservoir by a Kerr-nonlinear resonator». In: *Phys. Rev. A* 111 (1 Jan. 2025), p. 012412 (cit. on p. 2).

[29] Hang Cheng et al. «Quantum torque sensing with Kerr cavity optomechanics». In: *Opt. Express* 33.19 (Sept. 2025), pp. 40317–40327 (cit. on p. 2).

[30] M. del Pilar Campos Marino et al. «Microfabricated resonators for sensing applications». Poster at Quantum Timekeepers 2025 Summer School. Sept. 2025 (cit. on p. 2).

[31] Yoshitomo Okawachi et al. «Chip-scale frequency combs for data communications in computing systems». In: *Optica* 10.8 (Aug. 2023), pp. 977–995 (cit. on p. 2).

[32] Zachary L. Newman et al. «Architecture for the photonic integration of an optical atomic clock». In: *Optica* 6.5 (May 2019), pp. 680–685 (cit. on p. 2).

[33] Kyle W. Martin et al. «Compact Optical Atomic Clock Based on a Two-Photon Transition in Rubidium». In: *Phys. Rev. Appl.* 9 (1 Jan. 2018), p. 014019 (cit. on p. 2).

[34] *RUBRIComb Frequency Comb*. RUBRIComb. Vescent (cit. on p. 2).

[35] *Compact Optical Frequency Comb Precision in Every Pulse*. SmartComb-ULN. Menlo Systems (cit. on p. 2).

[36] David J. Moss et al. «New CMOS-compatible platforms based on silicon nitride and Hydex for nonlinear optics». In: *Nature Photonics* 7.8 (July 2013), pp. 597–607. ISSN: 1749-4893 (cit. on p. 7).

[37] M.K. Chin and S.T. Ho. «Design and modeling of waveguide-coupled single-mode microring resonators». In: *Journal of Lightwave Technology* 16.8 (1998), pp. 1433–1446 (cit. on p. 7).

[38] Ch Fabry and A. Perot. «Théorie et applications d'une nouvelle méthode de spectroscopie interférentielle». In: *Annales de Chimie et de Physique, 7. Série* 16 (Jan. 1899) (cit. on p. 8).

[39] Warren Nagourney. *Quantum Electronics for Atomic Physics and Telecommunication*. Oxford University Press, May 2014. ISBN: 9780199665488 (cit. on pp. 8, 9).

[40] Nur Ismail et al. «Fabry-Pérot resonator: spectral line shapes, generic and related Airy distributions, linewidths, finesses, and performance at low or frequency-dependent reflectivity». In: *Opt. Express* 24.15 (July 2016), pp. 16366–16389 (cit. on p. 8).

[41] Manfred Hammer, Kirankumar Hiremath, and Remco Stoffer. «Analytical Approaches to the Description of Optical Microresonator Devices». In: 709 (Jan. 2004) (cit. on p. 8).

[42] F. Della Valle et al. «Extremely long decay time optical cavity». In: *Opt. Express* 22.10 (May 2014), pp. 11570–11577 (cit. on p. 9).

[43] Shun Fujii and Takasumi Tanabe. «Dispersion engineering and measurement of whispering gallery mode microresonator for Kerr frequency comb generation». In: *Nanophotonics* 9.5 (2020), pp. 1087–1104 (cit. on p. 10).

[44] Xiaoxiao Xue et al. «Thermal tuning of Kerr frequency combs in silicon nitride microring resonators». In: *Opt. Express* 24.1 (Jan. 2016), pp. 687–698 (cit. on p. 10).

[45] Lukas Max Weituschat et al. «Photonic and Thermal Modelling of Microrings in Silicon, Diamond and GaN for Temperature Sensing». In: *Nanomaterials* 10.5 (2020). ISSN: 2079-4991 (cit. on p. 10).

[46] Tobias Herr et al. «Temporal solitons in optical microresonators». In: *Nature Photonics* 8 (Nov. 2012) (cit. on pp. 10, 45, 46).

[47] Tal Carmon, Lan Yang, and Kerry J. Vahala. «Dynamical thermal behavior and thermal self-stability of microcavities». In: *Opt. Express* 12.20 (Oct. 2004), pp. 4742–4750 (cit. on p. 10).

[48] Erwan Lucas et al. «Detuning-dependent properties and dispersion-induced instabilities of temporal dissipative Kerr solitons in optical microresonators». In: *Phys. Rev. A* 95 (4 Apr. 2017), p. 043822 (cit. on pp. 11, 12).

[49] Brent E. Little, Juha-Pekka Laine, and Sai T. Chu. «Surface-roughness-induced contradirectional coupling in ring and disk resonators». In: *Opt. Lett.* 22.1 (Jan. 1997), pp. 4–6 (cit. on p. 18).

[50] Poolad Imany et al. «50-GHz-spaced comb of high-dimensional frequency-bin entangled photons from an on-chip silicon nitride microresonator». In: *Opt. Express* 26.2 (Jan. 2018), pp. 1825–1840 (cit. on p. 19).

[51] Wenjun Wen et al. «Realizing an Entanglement-Based Multiuser Quantum Network with Integrated Photonics». In: *Phys. Rev. Appl.* 18 (2 Aug. 2022), p. 024059 (cit. on pp. 19, 108).

[52] T. Hansson, D. Modotto, and S. Wabnitz. «Analytical approach to the design of microring resonators for nonlinear four-wave mixing applications». In: *J. Opt. Soc. Am. B* 31.5 (May 2014), pp. 1109–1117 (cit. on p. 22).

[53] Govind Agrawal. «Chapter 1 - Introduction». In: *Nonlinear Fiber Optics (Fifth Edition)*. Ed. by Govind Agrawal. Fifth Edition. Optics and Photonics. Boston: Academic Press, 2013, pp. 1–25 (cit. on pp. 22, 52).

[54] *InGaAs Photodiodes*. FGA04. Thorlabs (cit. on p. 24).

[55] *Photodetectors*. ET-3010. Electro Optics Technologies (cit. on p. 24).

[56] *High Speed InGaAs Photodiodes*. FCI-InGaAs. OSI Optoelectronics (cit. on p. 24).

[57] Chandra M Natarajan, Michael G Tanner, and Robert H Hadfield. «Superconducting nanowire single-photon detectors: physics and applications». In: *Superconductor science and technology* 25.6 (2012), p. 063001 (cit. on p. 25).

[58] *Single Quantum Eos*. Eos. Single Quantum (cit. on p. 25).

[59] *SNSPD*. ID281 Pro SNSPD System. ID Quantique (cit. on p. 25).

[60] *InGaAs SPAD*. ID Qube ULN. ID Quantique (cit. on p. 25).

[61] Alan Migdall et al. *Single-photon generation and detection: physics and applications*. Vol. 45. Academic Press, 2013 (cit. on pp. 26, 29).

[62] Marco López et al. «A study to develop a robust method for measuring the detection efficiency of free-running InGaAs/InP single-photon detectors». In: *EPJ Quantum Technology* 7 (Dec. 2020) (cit. on p. 26).

[63] S. Virzì et al. «Detection efficiency characterization for free-space single-photon detectors: Measurement facility and wavelength-dependence investigation». In: *Applied Physics Letters* 125.22 (Nov. 2024), p. 221108. ISSN: 0003-6951 (cit. on pp. 26, 29).

[64] BIPM et al. *Evaluation of measurement data — Guide to the expression of uncertainty in measurement*. Joint Committee for Guides in Metrology, JCGM 100:2008 (cit. on p. 29).

[65] S Castelletto, I P Degiovanni, and M L Rastello. «Theoretical aspects of photon number measurement». In: *Metrologia* 37.5 (Oct. 2000), p. 613 (cit. on p. 29).

[66] SN Dorenbos et al. «Superconducting single photon detectors with minimized polarization dependence». In: *Applied Physics Letters* 93.16 (2008) (cit. on p. 33).

[67] Varun B. Verma et al. «A three-dimensional, polarization-insensitive superconducting nanowire avalanche photodetector». In: *Applied Physics Letters* 101.25 (2012) (cit. on p. 33).

[68] Kai Zou et al. «Fractal superconducting nanowire single-photon detectors working in dual bands and their applications in free-space and underwater hybrid LIDAR». In: *Opt. Lett.* 48.2 (Jan. 2023), pp. 415–418 (cit. on p. 33).

[69] T. H. Maiman. «Optical and Microwave-Optical Experiments in Ruby». In: *Phys. Rev. Lett.* 4 (11 June 1960), pp. 564–566 (cit. on p. 35).

[70] D. A. Kleinman, A. Ashkin, and G. D. Boyd. «Second-Harmonic Generation of Light by Focused Laser Beams». In: *Phys. Rev.* 145 (1 May 1966), pp. 338–379 (cit. on p. 36).

[71] Anthony Mark Fox. *Quantum optics: an introduction*. Vol. 15. Oxford University Press, 2006 (cit. on pp. 36, 64).

[72] Lucia Caspani et al. «Integrated sources of photon quantum states based on nonlinear optics». In: *Light: Science & Applications* 6.11 (June 2017), e17100–e17100. ISSN: 2047-7538 (cit. on pp. 36, 50, 65, 67, 76, 78).

[73] Marco Fiorentino and Raymond G. Beausoleil. «Compact sources of polarization-entangled photons». In: *Opt. Express* 16.24 (Nov. 2008), pp. 20149–20156 (cit. on p. 36).

[74] M. D. Eisaman et al. «Invited Review Article: Single-photon sources and detectors». In: *Review of Scientific Instruments* 82.7 (July 2011), p. 071101. ISSN: 0034-6748 (cit. on p. 36).

[75] C.-A. Bunge, M. Beckers, and B. Lustermann. «3 - Basic principles of optical fibres». In: *Polymer Optical Fibres*. Ed. by Christian-Alexander Bunge, Thomas Gries, and Markus Beckers. Woodhead Publishing, 2017, pp. 47–118. ISBN: 978-0-08-100039-7 (cit. on p. 36).

[76] Guoping Lin, Aurélien Coillet, and Yanne K. Chembo. «Nonlinear photonics with high-Q whispering-gallery-mode resonators». In: *Adv. Opt. Photon.* 9.4 (Dec. 2017), pp. 828–890 (cit. on p. 36).

[77] Marlan O. Scully and M. Suhail Zubairy. *Quantum Optics*. Cambridge University Press, 1997 (cit. on p. 38).

[78] R. Paschotta. *Optical Parametric Oscillators*. RP Photonics Encyclopedia. 2008 (cit. on p. 39).

[79] Mikael Siltanen, Tomi Leinonen, and Lauri Halonen. «Decreased oscillation threshold of a continuous-wave OPO using a semiconductor gain mirror». In: *Opt. Express* 19.20 (Sept. 2011), pp. 19675–19680 (cit. on p. 39).

[80] Luca Zatti, J. E. Sipe, and Marco Liscidini. «Generation of photon pairs by spontaneous four-wave mixing in linearly uncoupled resonators». In: *Phys. Rev. A* 107 (1 Jan. 2023), p. 013514 (cit. on p. 39).

[81] G. J. Rodríguez Becerra et al. «Integrated photon pairs source based on counter-propagating spontaneous four wave mixing in a silicon nitride microring resonator». In: *Appl. Opt.* 63.27 (Sept. 2024), pp. 7278–7285 (cit. on p. 40).

[82] M. Liscidini, L. G. Helt, and J. E. Sipe. «Asymptotic fields for a Hamiltonian treatment of nonlinear electromagnetic phenomena». In: *Phys. Rev. A* 85 (1 Jan. 2012), p. 013833 (cit. on p. 41).

[83] Stefano Azzini et al. «From classical four-wave mixing to parametric fluorescence in silicon microring resonators». In: *Opt. Lett.* 37.18 (Sept. 2012), pp. 3807–3809 (cit. on p. 41).

[84] Michael Kues et al. «On-chip generation of high-dimensional entangled quantum states and their coherent control». In: *Nature* 546 (2017), pp. 622–626 (cit. on p. 41).

[85] L. Mandelstam and Ig. Tamm. «The Uncertainty Relation Between Energy and Time in Non-relativistic Quantum Mechanics». In: *Selected Papers*. Ed. by Boris M. Bolotovskii, Victor Ya. Frenkel, and Rudolf Peierls. Berlin, Heidelberg: Springer Berlin Heidelberg, 1991, pp. 115–123. ISBN: 978-3-642-74626-0 (cit. on p. 42).

[86] R. Paschotta. *Frequency Combs*. RP Photonics Encyclopedia. 2007 (cit. on p. 42).

[87] Tara Fortier and Esther Baumann. «20 years of developments in optical frequency comb technology and applications». In: *Communications Physics* 2.1 (Dec. 2019). ISSN: 2399-3650 (cit. on p. 42).

[88] A.D. Ellis and A.M. Perego. *Optical Frequency Combs: Trends in Sources and Applications*. CRC Press, 2024. ISBN: 9781032548104 (cit. on p. 42).

[89] Scott A. Diddams, Kerry Vahala, and Thomas Udem. «Optical frequency combs: Coherently uniting the electromagnetic spectrum». In: *Science* 369.6501 (2020), eaay3676 (cit. on p. 42).

[90] D. E. Spence, P. N. Kean, and W. Sibbett. «60-fsec pulse generation from a self-mode-locked Ti:sapphire laser». In: *Opt. Lett.* 16.1 (Jan. 1991), pp. 42–44 (cit. on p. 42).

[91] T. Kobayashi et al. «High-repetition-rate optical pulse generator using a Fabry-Perot electro-optic modulator». In: *Applied Physics Letters* 21.8 (Oct. 1972), pp. 341–343. ISSN: 0003-6951 (cit. on p. 42).

[92] Tobias J. Kippenberg et al. «Dissipative Kerr solitons in optical microresonators». In: *Science* 361.6402 (2018), eaan8083 (cit. on pp. 42, 43, 46).

[93] Dmitry Kazakov et al. «Driven bright solitons on a mid-infrared laser chip». In: *Nature* 641 (Apr. 2025), pp. 83–89 (cit. on p. 42).

[94] L. A. Lugiato and R. Lefever. «Spatial Dissipative Structures in Passive Optical Systems». In: *Phys. Rev. Lett.* 58 (21 May 1987), pp. 2209–2211 (cit. on p. 42).

[95] Cyril Godey et al. «Stability analysis of the spatiotemporal Lugiato-Lefever model for Kerr optical frequency combs in the anomalous and normal dispersion regimes». In: *Phys. Rev. A* 89 (6 June 2014), p. 063814 (cit. on p. 43).

[96] Aurélien Coillet et al. «Azimuthal Turing Patterns, Bright and Dark Cavity Solitons in Kerr Combs Generated With Whispering-Gallery-Mode Resonators». In: *IEEE Photonics Journal* 5.4 (2013), pp. 6100409–6100409 (cit. on p. 43).

[97] Melissa A. Guidry et al. «Quantum optics of soliton microcombs». In: *Nature Photonics* 16.1 (Dec. 2021), pp. 52–58. ISSN: 1749-4893 (cit. on p. 44).

[98] H. Guo et al. «Universal dynamics and deterministic switching of dissipative Kerr solitons in optical microresonators». In: *Nature Physics* 13.1 (Sept. 2016), pp. 94–102. ISSN: 1745-2481 (cit. on p. 44).

[99] A. B. Matsko, A. A. Savchenkov, and L. Maleki. «On excitation of breather solitons in an optical microresonator». In: *Opt. Lett.* 37.23 (Dec. 2012), pp. 4856–4858 (cit. on p. 45).

[100] M. Haelterman, S. Trillo, and S. Wabnitz. «Dissipative modulation instability in a nonlinear dispersive ring cavity». In: *Optics Communications* 91.5 (1992), pp. 401–407. ISSN: 0030-4018 (cit. on p. 45).

[101] Yanne K. Chembo. «Kerr optical frequency combs: theory, applications and perspectives». In: *Nanophotonics* 5.2 (2016), pp. 214–230 (cit. on p. 45).

[102] Solomon Manukure and Timesha Booker. «A short overview of solitons and applications». In: *Partial Differential Equations in Applied Mathematics* 4 (2021), p. 100140. ISSN: 2666-8181 (cit. on p. 46).

[103] Elham Nazemosadat et al. «Switching Dynamics of Dark Solitons in Kerr Microresonators». In: *2019 Conference on Lasers and Electro-Optics Europe & European Quantum Electronics Conference (CLEO/Europe-EQEC)*. 2019, pp. 1–1 (cit. on p. 46).

[104] L. Columbo et al. «Unifying Frequency Combs in Active and Passive Cavities: Temporal Solitons in Externally Driven Ring Lasers». In: *Phys. Rev. Lett.* 126 (17 Apr. 2021), p. 173903 (cit. on p. 46).

[105] L. L. Columbo et al. «Dynamics of a broad-band quantum cascade laser: from chaos to coherent dynamics and mode-locking». In: *Opt. Express* 26.3 (Feb. 2018), pp. 2829–2847 (cit. on p. 46).

[106] Luigi Lugiato, Franco Prati, and Massimo Brambilla. *Nonlinear Optical Systems*. Cambridge University Press, 2015 (cit. on p. 46).

[107] Ruiyang Chen et al. «Ultralow-Loss Integrated Photonics Enables Bright, Narrowband, Photon-Pair Sources». In: *Phys. Rev. Lett.* 133 (8 Aug. 2024), p. 083803 (cit. on pp. 50, 54, 55, 70, 81, 87).

[108] Christian Reimer et al. «Integrated frequency comb source of heralded single photons». In: *Opt. Express* 22.6 (Mar. 2014), pp. 6535–6546 (cit. on pp. 50, 54, 73, 81).

[109] Erman Engin et al. «Photon pair generation in a silicon micro-ring resonator with reverse bias enhancement». In: *Opt. Express* 21.23 (Nov. 2013), pp. 27826–27834 (cit. on pp. 51, 54, 55, 58).

[110] Farid Samara et al. «High-rate photon pairs and sequential Time-Bin entanglement with Si3N4 microring resonators». In: *Optics Express* 27 (June 2019), pp. 19309–19318 (cit. on pp. 51, 54, 70, 87).

[111] Alexandre Chopin et al. «Ultra-efficient resonant generation of time-energy entangled photon pairs in a InGaP Photonic Crystal Cavity». In: *Conference on Lasers and Electro-Optics/Europe (CLEO/Europe 2023) and European Quantum Electronics Conference (EQEC 2023)*. Optica Publishing Group, 2023 (cit. on p. 51).

[112] K Inoue and K Shimizu. «Generation of quantum-correlated photon pairs in optical fiber: Influence of spontaneous Raman scattering». In: *Japanese journal of applied physics part 1 - Regular papers short notes & review papers* 43.12 (Dec. 2004), pp. 8048–8052. ISSN: 0021-4922 (cit. on p. 52).

[113] Chaoxuan Ma et al. «Silicon photonic entangled photon-pair and heralded single photon generation with CAR $>$ 12,000 and $g(2)(0) < 0.006$». In: *Opt. Express* 25.26 (Dec. 2017), pp. 32995–33006 (cit. on pp. 53, 54, 70, 81, 85, 87).

[114] Xiyuan Lu et al. «Biphoton Statistics of Quantum Light Generated on a Silicon Chip». In: *ACS Photonics* 3.9 (2016), pp. 1626–1636 (cit. on p. 54).

[115] Linghua Wang et al. «Nonlinear silicon nitride waveguides based on a PECVD deposition platform». In: *Optics Express* 26 (Apr. 2018), pp. 9645–9654 (cit. on p. 55).

[116] M.P. Hasselbeck. «NONLINEAR OPTICS, BASICS | Nomenclature and Units». In: *Encyclopedia of Modern Optics*. Ed. by Robert D. Guenther. Oxford: Elsevier, 2005, pp. 240–246. ISBN: 978-0-12-369395-2 (cit. on p. 55).

[117] LIGENTEC. *Technology - LIGENTEC* (cit. on p. 55).

[118] Jacob Levy et al. «CMOS-compatible multiple-wavelength oscillator for on-chip optical interconnects». In: *Nature Photonics* 4 (Dec. 2009), pp. 37–40 (cit. on p. 55).

[119] L. G. Helt et al. «Spontaneous four-wave mixing in microring resonators». In: *Opt. Lett.* 35.18 (Sept. 2010), pp. 3006–3008 (cit. on p. 58).

[120] D N Klyshko. «Use of two-photon light for absolute calibration of photoelectric detectors». In: *Soviet Journal of Quantum Electronics* 10.9 (Sept. 1980), p. 1112 (cit. on p. 59).

[121] Xiyuan Lu et al. «Heralding single photons from a high-Q silicon microdisk». In: *Optica* 3.12 (Dec. 2016), pp. 1331–1338 (cit. on p. 60).

[122] Z. Vernon, M. Liscidini, and J. E. Sipe. «No free lunch: the trade-off between heralding rate and efficiency in microresonator-based heralded single photon sources». In: *Opt. Lett.* 41.4 (Feb. 2016), pp. 788–791 (cit. on p. 60).

[123] Xiang Guo et al. «Parametric down-conversion photon pair source on a nanophotonic chip». In: *Light: Science & Applications* (May 2017) (cit. on p. 61).

[124] Chaoxuan Ma and Shayan Mookherjea. «Simultaneous dual-band entangled photon pair generation using a silicon photonic microring resonator». In: *Quantum Science and Technology* 3 (Apr. 2018) (cit. on p. 61).

[125] Kai Guo et al. «Nonclassical Optical Bistability and Resonance-Locked Regime of Photon-Pair Sources Using Silicon Microring Resonator». In: *Physical Review Applied* 11 (Mar. 2019) (cit. on p. 61).

[126] Andreas Christ et al. «Probing multimode squeezing with correlation functions». In: *New Journal of Physics* 13.3 (Mar. 2011), p. 033027. ISSN: 1367-2630 (cit. on pp. 62, 71).

[127] Leonard Mandel and Emil Wolf. «Coherent states of the electromagnetic field». In: *Optical Coherence and Quantum Optics*. Cambridge University Press, 1995, pp. 522–572 (cit. on p. 62).

[128] Geoffrey Brooker. *Modern classical optics*. Vol. 8. Oxford University Press, 2003 (cit. on p. 63).

[129] NKT Photonics. *Laser Spectral Linewidth*. Tech. rep. V1.0. NKT Photonics, Sept. 2013 (cit. on p. 63).

[130] Krzysztof Iniewski. *Wireless technologies: circuits, systems, and devices*. CRC press, 2017 (cit. on p. 64).

[131] Rodney Loudon. *The Quantum Theory of Light*. Oxford University Press, Sept. 2000. ISBN: 9780198501770 (cit. on pp. 65, 92).

[132] Gregg Jaeger. «Qubits». In: *Quantum Information: An Overview*. New York, NY: Springer New York, 2007, pp. 1–27. ISBN: 978-0-387-36944-0 (cit. on p. 65).

[133] Kevin Zielnicki et al. «Joint spectral characterization of photon-pair sources». In: *Journal of Modern Optics* 65.10 (2018), pp. 1141–1160 (cit. on pp. 65, 67).

[134] Shikhar Uttam. «Chapter 4 - Introduction to Quantum Information Processing». In: *Quantum Information Processing and Quantum Error Correction*. Ed. by Ivan Djordjevic. Oxford: Academic Press, 2012, pp. 119–144. ISBN: 978-0-12-385491-9 (cit. on p. 65).

[135] M. U. Karelin. «The schmidt number of pure continuous-variable bipartite entangled states and the method of its calculation». In: *Optics and Spectroscopy* 103.2 (Aug. 2007), pp. 193–195. ISSN: 1562-6911 (cit. on p. 65).

[136] Leonard Mandel. «Fluctuations of photon beams and their correlations». In: *Proceedings of the Physical Society* 72.6 (1958), p. 1037 (cit. on p. 67).

[137] Stefano Azzini et al. «Ultra-low power generation of twin photons in a compact silicon ring resonator». In: *Opt. Express* 20.21 (Oct. 2012), pp. 23100–23107 (cit. on p. 70).

[138] Adrien Bensemhoun et al. «Multipartite entanglement in bright frequency combs out of microresonators». In: *Physics Letters A* 493 (2024), p. 129272. ISSN: 0375-9601 (cit. on p. 70).

[139] Justin B. Spring et al. «On-chip low loss heralded source of pure single photons». In: *Opt. Express* 21.11 (June 2013), pp. 13522–13532 (cit. on p. 71).

[140] Leonard Mandel and Emil Wolf. «Quantum theory of photoelectric detection of light». In: *Optical Coherence and Quantum Optics*. Cambridge University Press, 1995, pp. 683–740 (cit. on p. 72).

[141] Roy J. Glauber. «The Quantum Theory of Optical Coherence». In: *Phys. Rev.* 130 (6 June 1963), pp. 2529–2539 (cit. on p. 72).

[142] Leonard Mandel and Emil Wolf. «Random (or stochastic) processes». In: *Optical Coherence and Quantum Optics*. Cambridge University Press, 1995, pp. 41–91 (cit. on p. 72).

[143] Rui-Bo Jin and Ryosuke Shimizu. «Extended Wiener–Khinchin theorem for quantum spectral analysis». In: *Optica* 5.2 (Feb. 2018), pp. 93–98 (cit. on p. 72).

[144] U. M. Titulaer and R. J. Glauber. «Correlation Functions for Coherent Fields». In: *Phys. Rev.* 140 (3B Nov. 1965), B676–B682 (cit. on p. 73).

[145] Z. Y. Ou and Y. J. Lu. «Cavity Enhanced Spontaneous Parametric Down-Conversion for the Prolongation of Correlation Time between Conjugate Photons». In: *Phys. Rev. Lett.* 83 (13 Sept. 1999), pp. 2556–2559 (cit. on p. 73).

[146] Ulrike Herzog, Matthias Scholz, and Oliver Benson. «Theory of biphoton generation in a single-resonant optical parametric oscillator far below threshold». In: *Phys. Rev. A* 77 (2 Feb. 2008), p. 023826 (cit. on p. 73).

[147] G. Brida et al. «An extremely low-noise heralded single-photon source: A breakthrough for quantum technologies». In: *Applied Physics Letters* 101.22 (Nov. 2012), p. 221112. ISSN: 0003-6951 (cit. on p. 76).

[148] Haoyang Wang et al. «Bright Heralded Single-Photon Source Saturating Theoretical Single-photon Purity». In: *Laser & Photonics Reviews* 19.9 (2025), p. 2401420 (cit. on p. 77).

[149] P Grangier, G Roger, and A Aspect. «Experimental evidence for a Photon Anticorrelation Effect on a Beam Splitter: a New Light on Single-Photon Sources». In: *Europhysics Letters* 1.4 (Feb. 1986), pp. 173–179. ISSN: 0295-5075 (cit. on p. 78).

[150] G. Brida et al. «A conclusive experiment to throw more light on "light"». In: *Physics Letters A* 328.4 (2004), pp. 313–318. ISSN: 0375-9601 (cit. on p. 78).

[151] G. Brida et al. «Experimental realization of a low-noise heralded single-photon source». In: *Opt. Express* 19.2 (Jan. 2011), pp. 1484–1492 (cit. on pp. 78, 79).

[152] Yun-Ru Fan et al. «Multi-Wavelength Quantum Light Sources on Silicon Nitride Micro-Ring Chip». In: *Laser & Photonics Reviews* 17.10 (2023), p. 2300172 (cit. on pp. 81, 82, 87).

[153] Imad I. Faruque et al. «Estimating the Indistinguishability of Heralded Single Photons Using Second-Order Correlation». In: *Phys. Rev. Appl.* 12 (5 Nov. 2019), p. 054029 (cit. on p. 81).

[154] J. Brendel, E. Mohler, and W. Martienssen. «Time-resolved dual-beam two-photon interferences with high visibility». In: *Phys. Rev. Lett.* 66 (9 Mar. 1991), pp. 1142–1145 (cit. on pp. 82, 85).

[155] J. D. Franson. «Bell inequality for position and time». In: *Phys. Rev. Lett.* 62 (19 May 1989), pp. 2205–2208 (cit. on pp. 82, 83, 87).

[156] Jing Suo et al. «Generation of hyper-entanglement on polarization and energy-time based on a silicon micro-ring cavity». In: *Opt. Express* 23.4 (Feb. 2015), pp. 3985–3995 (cit. on p. 83).

[157] J. Brendel et al. «Pulsed Energy-Time Entangled Twin-Photon Source for Quantum Communication». In: *Phys. Rev. Lett.* 82 (12 Mar. 1999), pp. 2594–2597 (cit. on p. 84).

[158] J. S. Bell and Alain Aspect. *Speakable and Unspeakable in Quantum Mechanics: Collected Papers on Quantum Philosophy*. 2nd ed. Cambridge University Press, 2004 (cit. on p. 84).

[159] John F. Clauser et al. «Proposed Experiment to Test Local Hidden-Variable Theories». In: *Phys. Rev. Lett.* 23 (15 Oct. 1969), pp. 880–884 (cit. on p. 84).

[160] P. G. Kwiat, A. M. Steinberg, and R. Y. Chiao. «High-visibility interference in a Bell-inequality experiment for energy and time». In: *Phys. Rev. A* 47 (4 Apr. 1993), R2472–R2475 (cit. on p. 85).

[161] P. G. Kwiat et al. «Correlated two-photon interference in a dual-beam Michelson interferometer». In: *Phys. Rev. A* 41 (5 Mar. 1990), pp. 2910–2913 (cit. on pp. 85, 87).

[162] Rakesh Ranjan Kumar et al. «Quantum states of higher-order whispering gallery modes in a silicon micro-disk resonator». In: *J. Opt. Soc. Am. B* 37.8 (Aug. 2020), pp. 2231–2237 (cit. on p. 85).

[163] P. G. Kwiat, A. M. Steinberg, and R. Y. Chiao. «High-visibility interference in a Bell-inequality experiment for energy and time». In: *Phys. Rev. A* 47 (4 Apr. 1993), R2472–R2475 (cit. on pp. 85, 87).

[164] Sven Aerts et al. «Two-Photon Franson-Type Experiments and Local Realism». In: *Phys. Rev. Lett.* 83 (15 Oct. 1999), pp. 2872–2875 (cit. on p. 87).

[165] Francesco Vedovato et al. «Postselection-Loophole-Free Bell Violation with Genuine Time-Bin Entanglement». In: *Phys. Rev. Lett.* 121 (19 Nov. 2018), p. 190401 (cit. on p. 88).

[166] Irene Goti et al. «Absolute frequency measurement of a Yb optical clock at the limit of the Cs fountain». In: *Metrologia* 60.3 (May 2023), p. 035002 (cit. on p. 90).

[167] C. Simon et al. «Quantum memories: A review based on the European integrated project "Qubit Applications (QAP)"». In: *The European Physical Journal D* 58.1 (Apr. 2010), pp. 1–22. ISSN: 1434-6079 (cit. on p. 107).

[168] Khabat Heshami et al. «Quantum memories: emerging applications and recent advances». In: *Journal of Modern Optics* 63.20 (2016), pp. 2005–2028 (cit. on p. 107).

[169] Jinxian Guo et al. «High-performance Raman quantum memory with optimal control in room temperature atoms». In: *Nature Communications* 10.1 (Jan. 2019). ISSN: 2041-1723 (cit. on p. 107).

[170] Noemi Tagliavacche et al. «Frequency-bin entanglement-based Quantum Key Distribution». In: *npj Quantum Information* 11.1 (Apr. 2025). ISSN: 2056-6387 (cit. on pp. 107, 108).

[171] Bin Fang et al. «Fast and highly resolved capture of the joint spectral density of photon pairs». In: *Optica* 1.5 (Nov. 2014), pp. 281–284 (cit. on p. 108).

[172] M. Liscidini and J. E. Sipe. «Stimulated Emission Tomography». In: *Phys. Rev. Lett.* 111 (19 Nov. 2013), p. 193602 (cit. on p. 108).

[173] Dongning Liu et al. «Photonic-reconfigurable entanglement distribution network based on silicon quantum photonics». In: *Photon. Res.* 11.7 (July 2023), pp. 1314–1325 (cit. on p. 108).

[174] Hao Yu et al. «Quantum key distribution implemented with d-level time-bin entangled photons». In: *Nature Communications* 16 (Jan. 2025) (cit. on p. 108).